
[All ETDs from UAB](#)

[UAB Theses & Dissertations](#)

1999

A silicon /silver multilayer Fabry -Perot bandpass transmission filter for use near 28.4 nm.

David B. Gore
University of Alabama at Birmingham

Follow this and additional works at: <https://digitalcommons.library.uab.edu/etd-collection>

Recommended Citation

Gore, David B., "A silicon /silver multilayer Fabry -Perot bandpass transmission filter for use near 28.4 nm." (1999). *All ETDs from UAB*. 6363.
<https://digitalcommons.library.uab.edu/etd-collection/6363>

This content has been accepted for inclusion by an authorized administrator of the UAB Digital Commons, and is provided as a free open access item. All inquiries regarding this item or the UAB Digital Commons should be directed to the [UAB Libraries Office of Scholarly Communication](#).

INFORMATION TO USERS

This manuscript has been reproduced from the microfilm master. UMI films the text directly from the original or copy submitted. Thus, some thesis and dissertation copies are in typewriter face, while others may be from any type of computer printer.

The quality of this reproduction is dependent upon the quality of the copy submitted. Broken or indistinct print, colored or poor quality illustrations and photographs, print bleedthrough, substandard margins, and improper alignment can adversely affect reproduction.

In the unlikely event that the author did not send UMI a complete manuscript and there are missing pages, these will be noted. Also, if unauthorized copyright material had to be removed, a note will indicate the deletion.

Oversize materials (e.g., maps, drawings, charts) are reproduced by sectioning the original, beginning at the upper left-hand corner and continuing from left to right in equal sections with small overlaps. Each original is also photographed in one exposure and is included in reduced form at the back of the book.

Photographs included in the original manuscript have been reproduced xerographically in this copy. Higher quality 6" x 9" black and white photographic prints are available for any photographs or illustrations appearing in this copy for an additional charge. Contact UMI directly to order.

UMI[®]

Bell & Howell Information and Learning
300 North Zeeb Road, Ann Arbor, MI 48106-1346 USA
800-521-0600

**A SILICON/SILVER MULTILAYER
FABRY-PEROT BANDPASS TRANSMISSION FILTER
FOR USE NEAR 28.4 NM**

by

DAVID B. GORE

A DISSERTATION

**Submitted to the graduate faculty of The University of Alabama at Birmingham,
in partial fulfillment of the requirements for the degree of
Doctor of Philosophy**

BIRMINGHAM, ALABAMA

1999

UMI Number: 9946709

UMI Microform 9946709
Copyright 1999, by UMI Company. All rights reserved.

**This microform edition is protected against unauthorized
copying under Title 17, United States Code.**

UMI
300 North Zeeb Road
Ann Arbor, MI 48103

ABSTRACT OF DISSERTATION
GRADUATE SCHOOL, UNIVERSITY OF ALABAMA AT BIRMINGHAM

Degree Ph.D. Program Physics
Name of Candidate David B. Gore
Committee Chair David L. Shealy
Title A Silicon/Silver Multilayer Fabry-Perot Bandpass Transmission Filter for
Use Near 28.4 nm

A transmissive Fabry-Perot filter was designed, fabricated, and tested in an attempt to reduce the bandpass near the Fe XV spectral line in the extreme ultraviolet. The design of the filter involved analysis of the optical constants of the available materials, examination of binary alloy tables for candidate material pairs, and computer modeling of possible configurations. Of the materials available, silicon and silver were determined to best fit the requirements of high throughput, low off-peak transmissivity, and minimal rate of interdiffusion. The optical component was fabricated using radio frequency triode sputter deposition onto silicon wafer substrates. An effort was also made to produce a transmissive substrate consisting of a thin silicon nitride window on a silicon wafer support structure using standard photolithographic and wet-etch techniques. Testing of the fabricated multilayer device included x-ray diffractometry, Auger spectroscopy, transmission electron microscopy, and reflectometry in the extreme ultraviolet.

The designed Fabry-Perot multilayer filter had a theoretical peak transmission of 1.55% at 28.0 nm and a full width at half maximum of 2.0 nm. The fabricated filter suffered from oxidation of its exposed silicon layer, addition of an adsorbed water layer, an interfacial roughness of between 0.5 and 1.2 nm, and a thickness error of

approximately 0.5 nm. If this filter were tested as a free-standing filter, its theoretical peak transmissivity would be between 1.05% and 0.75% at 27.0 nm with a full width at half maximum between 2.8 nm and 3.7 nm.

DEDICATION

To my parents

ACKNOWLEDGMENTS

Due to the experimental nature of this research, many people were involved. Without their help, much of the work done would not have been possible. First and foremost, I would like to thank Dr. Palmer N. Peters and Mr. Curtis Banks of NASA/Marshall Space Flight Center for their time and advice and the use of Dr. Peter's triode sputtering system to create the multilayer structures I tested. I would also like to thank Dr. Paul Ashley and Mr. Chris Maurer in the Army's Weapons Research Directorate for the use of their Silicon Wafer Processing Laboratory and the help they have provided.

Testing the fabricated multilayers rested in the hands of many people. I thank Dr. Marcus Vlasse of NASA/MSFC's Space Science Lab, Dr. Robin Griffin of UAB's Materials Science and Engineering Department, and Dr. Yogesh Vohra of UAB's Physics Department for their help and the use of their x-ray diffractometry equipment. Dr. Cheri Moss in the UAB Materials Science and Engineering Department gave me much of her time in performing Auger electron spectroscopy on some of my samples. In the same department, Mr. John Ji gave me much help in preparing samples for transmission electron microscopy. Finally, I would like to thank Dr. Arthur B. C. Walker and Dr. Dennis Martínez-Galarce of Stanford University's Center for Space Science and Astrophysics for allowing me access to the Stanford Synchrotron Radiation Laboratory (SSRL) and for their help in testing multilayers at extreme

ultraviolet wavelengths. SSRL is operated by the Department of Energy, office of Basic Energy Sciences.

In the area of support, I would like to thank Dr. William F. Kaukler of the University of Alabama in Huntsville, Dr. Vladimir Peskov and Dr. David Hathaway of NASA/MSFC, and many others who have guided me along the way. I would like to thank my advisor, Dr. David Shealy, for the opportunity to pursue a wide spectrum of research at NASA/MSFC and Mr. Richard B. Hoover for allowing me access to the Space Science Laboratory and its employees. I would also like to thank Dr. Arthur B. C. Walker, Mr. Richard B. Hoover, and the entire 1994 Multi-Spectral Solar Telescope Array crew at the Stanford Center for Space Science and Astrophysics for the chance to work on their rocket payload and help get it off the ground in November of that year.

I would also like to thank my parents and friends for their advice and patience as I complained about the numerous things graduate students complain about.

During the time I have been taking courses, passing exams, and ferreting out a research project, I have been funded under NASA Training Grant NGT-50880. The final four years of funding were provided by the University of Alabama at Birmingham Department of Physics.

TABLE OF CONTENTS

	<u>Page</u>
ABSTRACT	iii
DEDICATION	v
ACKNOWLEDGMENTS	vii
LIST OF TABLES	x
LIST OF FIGURES	xi
INTRODUCTION.....	1
OVERVIEW OF THE MULTI-SPECTRAL SOLAR TELESCOPE ARRAY	6
Pre-Flight Focussing	8
In-Field Focussing	13
Summary of Visible Light Testing	15
Filters	17
DESIGN.....	26
Multilayers	27
Optical Constants	31
Interfacial Roughness	35
Computational Modeling	40
Materials Search	40
FABRICATION AND TESTING.....	62
Radio Frequency Triode Sputtering.....	62
Substrate Preparation	67
Structure Testing	69
Auger Spectroscopy	70
X-ray Diffractometry	80
Transmission Electron Microscopy	85
Extreme Ultraviolet Reflectivity Testing.....	91

TABLE OF CONTENTS (Continued)

	<u>Page</u>
DISCUSSION AND CONCLUSIONS.....	101
LIST OF REFERENCES	110

LIST OF TABLES

<u>Table</u>	<u>Page</u>
1 MSSTA two-mirror telescope design specifications.....	7
2 MSSTA Herschelian specifications.....	8
3 Visible-light resolutions of the two mirrored telescopes.....	10
4 Visible light resolution test results.....	16
5 Thin film filters for MSSTA II.....	18
6 Silicon/Silver Fabry-Perot design specifications.....	60
7 Sputter deposition rates determined by stylus profilometry.....	63
8 Silicon/Silver Fabry-Perot as deposited.....	65
9 Energy windows for Figure 36.....	77
10 Energy windows for Figure 35.....	77
11 Comparison of results.....	101

LIST OF FIGURES

<u>Figure</u>	<u>Page</u>
1 Determination of back focus position.....	9
2 Modulation transfer function of the 17.3 nm Cassegrain.....	11
3 Modulation transfer function of the 21.1 nm Cassegrain.....	12
4 Locating back focus position with a Gaertner travelling microscope.....	14
5 Filter 94-1.....	19
6 Filter 94-2.....	20
7 Filter 94-3.....	21
8 Filter 94-4.....	22
9 Filter 94-5.....	23
10 Schematic of three layers inside a multilayer optical stack.....	28
11 Coefficients of absorption: Group I.....	42
12 Coefficients of absorption: Group IIa.....	43
13 Coefficients of absorption: Group IIb.....	44
14 Coefficients of absorption: Group III.....	45
15 Coefficients of absorption: Group IV.....	46
16 Coefficients of absorption: Group Va.....	47
17 Coefficients of absorption: Group Vb.....	48
18 Coefficients of absorption: Group VI.....	49

LIST OF FIGURES (Continued)

<u>Figure</u>	<u>Page</u>
19 Molybdenum-silicon Fabry-Perot filter.....	51
20 First candidates for Fabry-Perot filter.....	52
21 Binary alloy phase diagram for carbon and tungsten.....	54
22 X-ray diffraction profile of carbon/tungsten multilayer.....	55
23 X-ray diffraction profile of carbon/tungsten multilayer after two years.....	56
24 Binary alloy phase diagram for aluminum and zinc.....	57
25 Binary alloy phase diagram for silicon and zinc.....	58
26 Binary alloy phase diagram for silver and silicon.....	59
27 Fabry-Perot filter transmissivity as designed.....	61
28 MSFC RF triode set-up.....	64
29 Fabry-Perot filter transmissivity as designed for deposition.....	66
30 Auger surface scan of Sample 25.....	72
31 Auger scan of Sample 25 (120 s sputter).....	73
32 Auger scan of Sample 25 (300 s sputter).....	74
33 Scan of Sample 25.....	76
34 Depth scan of Sample 25 using high energy Si line.....	78
35 Depth scan of Sample 25 using low energy Si line.....	79
36 X-ray diffractometry profile of Sample 20: 23.88 nm/pair.....	82
37 X-ray diffractometry profile of Sample 28: 16.1 nm/pair.....	83
38 X-ray diffractometry profile of Fabry-Perot filter.....	84

LIST OF FIGURES (Continued)

<u>Figure</u>	<u>Page</u>
39 X-ray diffractometry profile of Fabry-Perot filter including thickness errors and interfacial roughness.....	86
40 Transmission electron micrograph of Sample 26.....	88
41 Transmission electron micrograph of Fabry-Perot filter.....	89
42 Pixel values for Fabry-Perot filter.....	90
43 Schematic of SSRL beam-line VIII-1.....	93
44 Raw data: photocathode signal for Optic 38.....	97
45 Extreme ultraviolet reflectivity of Fabry-Perot filter.....	98
46 Extreme ultraviolet reflectivity of Fabry-Perot filter including oxidation, interfacial roughness, and thickness errors.....	100
47 Comparison of perfect Fabry-Perot filter with experiment.....	102
48 Transmissivity of silicon nitride and silicon carbide windows 30 nm thick.....	106

INTRODUCTION

Standard glass lenses and metallic mirrors function poorly at wavelengths below 100 nm. As the wavelength of incident light decreases, the optical constants of materials approach unity. The reduced difference of index of refraction across an interface minimizes the effects of both refraction and reflection, lowering throughputs and efficiencies of these devices.

A common method employed to increase reflectivity of an interface at these short wavelengths is to line up many such interfaces on the optical axis. If the phase thickness of each layer is made such that reflected radiation adds in-phase at each interface, many small reflected amplitudes may be summed into a larger one. The optic obtained is called a “multilayer” mirror. The total reflectivity of such a mirror can become fairly large, reaching 60% near wavelengths of 13.5 nm.¹

By depositing such multilayer reflective coatings onto curved optics, imaging systems can be made. Such systems have been designed and employed with varying success for microscopes² and telescopes.³ Recently, metallic multilayer stacks have been fabricated to transmit 13-nm radiation. These devices have been employed as elements in polarization detectors⁴ (useful in synchrotron beam lines) and beam splitters.⁵

Reflective-optic, soft x-ray imaging systems only display their narrow band-passes in the soft x-ray regime. Being made of metallic coatings, these multilayers reflect ultraviolet, visible, and infrared radiation quite well. As interference devices,

they also reflect higher order radiation. If a spectrally broad source is being imaged, these wavelengths will make it to the image plane and will be recorded if not otherwise rejected. Currently, transmissive filters made of thin films (≈ 400 nm) of various metals deposited onto a nickel mesh support structure are placed in the optical path. By reflecting radiation with frequencies lower than the conduction frequency of the metal and absorbing radiation above the energy required to ionize inner shell electrons, they have been used both as high-pass filters for blocking visible wavelengths and low-pass filters for blocking higher order radiation.

The Multi-Spectral Solar Telescope Array (MSSTA)⁶ is a sounding rocket payload consisting of 19 telescopes designed to produce images of the sun at thirteen different spectral lines. This payload was successfully launched from White Sands Missile Range on 3 November, 1994. Seventeen of these telescopes employed reflecting soft x-ray multilayer optics imaging radiation between 4.4 and 30.4 nm.⁷ Visible and higher-order light rejection was accomplished via thin film filters placed approximately 8 cm from the focus of the telescopes. The proximity of these filters to the focal plane exposed them to focussed solar radiation. A few filters failed because of excessive heating. In addition, such close proximity to the focal plane would allow any breach to transmit a large amount of undesired solar flux to the image plane.

The design of these thin film filters makes tailoring their bandpasses difficult. The short wavelength cut-off is due to inelastic scattering, and the long wavelength cut-off is a function of the conduction frequency of the material. Shifting the wavelength of peak transmission or narrowing the bandpass is a matter of searching for

materials with the correct properties.⁸ Tailoring the optical characteristics of such a filter is non-trivial.

Currently, multilayer stacks are being used to make narrow band filters at infrared, visible, and near-ultraviolet wavelengths. Indeed, many of these are Fabry-Perot etalons and are commercially available with peak transmissivities from 180 nm through 1000 nm ($\frac{\Delta\lambda}{\lambda} \approx 0.017$ in the visible, 0.04 with $420 \text{ nm} \geq \lambda \geq 250 \text{ nm}$, and 0.18 with $248 \text{ nm} \geq \lambda \geq 180 \text{ nm}$). Fully metallic Fabry-Perot etalons can be analogously constructed to selectively filter radiation at shorter wavelengths. Barbee and Underwood have designed, constructed, and tested a tungsten/carbon multilayer Fabry-Perot filter to be used in reflection for the Cu K_α line (0.154 nm),⁹ and Fernandez *et al.* have designed, constructed, and tested a molybdenum/silicon multilayer Fabry-Perot filter to be used in reflection at 12.5-nm wavelengths.¹⁰

These filters are necessarily thin in order to minimize absorption effects in the system. Recently, multilayers have been deposited onto windows constructed of silicon nitride, boron nitride, or silicon carbide to divide the tasks of mechanical strength from those of optical quality in the production of soft x-ray beam-splitters.⁵ This may also prove to be useful in making larger filters, suitable for placement at the entrance of a telescopic system, where lower thermal loads would be placed on the filter and breaches in the filter would have a lessened impact on the imaging system.

The creation of a multilayer Fabry-Perot etalon filter for operation in the extreme ultraviolet (EUV) requires investigation into the MSSTA payload, optical and materials design considerations, fabrication technologies, and methods of testing the final filter. The MSSTA payload optics are designed to image solar radiation at

many wavelengths. Two of these wavelengths, Fe XV at 28.4 nm and He II at 30.4 nm, are very close to each other. It would be worthwhile to create the filter such that the center of the bandpass encompassed one of these two spectral lines and blocked the other. It was chosen to create the filter with a bandpass centered near 28.4 nm.

Both optical design and materials choices will determine the final performance of the filter. Determining the major contribution to the optical constants is important in choosing the correct indices of refraction to use during modeling. Those indices of refraction will be complex and indicate the presence of absorption. Absorption not only attenuates radiation traversing the system, but also induces an arbitrary phase change upon reflection from an interface. These two effects must be considered in the design of the filter. In addition, the interface between materials may no longer be abrupt at the dimensions of a tenth of a wavelength of the radiation of interest. These “rough” interfaces must be included in the model filter to better understand their role in the degradation of the filters performance. The materials themselves must be chosen with care. Even if the proper interface is created between a pair of materials, those materials must not change rapidly over time. If they should incorporate ambient materials (by oxidation, for example), the optical constants will change. If the two materials mix at their common boundary, they will induce rough interfaces.

Given the short wavelength of interest and the knowledge that a large amount of absorption will be present in the system, the layers set down to create the filter must necessarily be thin. These layers will be on the order of one-quarter the wavelength of light in thickness. To set down layers 10 nm thick, a system capable of extremely

slow rates of deposition must be found. The method of fabrication chosen was radio frequency triode sputtering. In addition, if the filter is to be transmissive, it must be set on a substrate that will pass 28.4-nm wavelengths. Silicon wet-etch techniques are suitable for creation of a thin support structure of silicon nitride spanning a window in a silicon wafer.

Testing the fabricated multilayer will need to elucidate both final materials content and structure. Auger spectroscopy is well suited to the task of determining the presence of impurities in the fabricated filter. The filter structure may be determined via three tests: x-ray diffractometry, transmission electron microscopy, and reflectometry at the wavelength of interest at a synchrotron beam-line source. X-ray diffractometry yields a rapid determination of gross structure and interfacial roughness. Transmission electron microscopy will reveal structures as small as 0.3 nm, which is necessary to determine the presence of defects in the filter. Finally, synchrotron beam-line testing yields information at the wavelength of interest and will reveal the presence of interfacial roughness, adsorbed atmospheric element layers, and oxidized materials.

OVERVIEW OF THE MULTI-SPECTRAL SOLAR TELESCOPE ARRAY

The MSSTA⁶ is a rocket-borne observatory designed to image the sun in selected soft x-ray (4.41-9.39 nm), extreme ultraviolet (EUV) [15.0-33.5 nm], and far ultraviolet (FUV) [121.56 and 155.0 nm] wavelengths. The MSSTA is a joint project of Stanford University, NASA/MSFC, and the Lawrence Livermore National Laboratory. Its first flight, on May 13, 1991, brought back many solar images, some with sub-arc second resolution.¹¹ Telescopes on the MSSTA use multilayer-coated normal incidence optics in order to obtain greater collecting area and diffraction-limited resolution not offered by grazing incidence systems. These telescopes were tested with standard interferometric and resolution target tests to determine optical performance. For the longer wavelengths, the MSSTA employs doubly reflecting Ritchey-Chrétien and Cassegrain telescopes. Detailed specifications are listed in Table 1. At soft x-ray wavelengths, the MSSTA utilizes single reflection Herschelien optics. Data for these telescopes⁶ are listed in Table 2. The second flight of the MSSTA, on November 3, 1994, carried six Ritchey-Chrétien, two Cassegrain, and eleven Herschelien telescopes.

The Ritchey-Chrétien telescopes are two-mirrored telescopes with hyperboloid optical elements. These mirrors are held in place in their cells with a vacuum compatible Dow Corning Silastic RTV which also allows for slight motion during vibrational loading. To minimize changes in mirror separation, the optical benches were constructed of graphite fiber in an epoxy resin matrix.³ Earlier theoretical studies revealed that the Ritchey-Chrétien telescopes could obtain spatial resolutions of better

than 0.3 arc s over a 48 arc min field of view at 121.6 nm (with the best possible resolution of 0.03 arc s occurring near the optical axis at a wavelength of 17.3 nm).¹² This second flight carried five Ritchey-Chrétien telescopes with mirrors coated to image wavelengths of 15.0, 19.3, 28.4, 30.4, and 155.0 nm. A Short Ritchey-Chrétien telescope was constructed, capable of obtaining resolutions of 0.22 arc s at its operating wavelength of 121.6 nm.¹³

The two Cassegrain telescopes are not true Cassegrains—the optical elements were fabricated as spheres. Conical elements of the smoothness required for the multilayer coatings were unavailable at the time the Cassegrain optics were made. The telescopes were found to be diffraction limited in visible wavelengths. The maximum resolution, however, is limited to 0.5 arc s due to aberration.¹⁴

Table 1. MSSTA two-mirror telescope design specifications.

	Ritchey-Chrétien	Short Ritchey-Chrétien	Cassegrain
Focal length (cm)	350	230	200
Mirror separation (cm)	80	55	42.3
Primary diameter (cm)	12.7	12.7	6.4
Secondary diameter (cm)	4.9	5.7	2.5
Total field of view (arc min)	48	73	48

The eleven Herschelian telescopes flown were of five different types and designed to operate at 4.42, 5.47 (2), 9.39, 14.3, 15.0 (2), 18.0, 19.3, 21.1, and 28.4 nm. All were off-axis paraboloids except for the 18.0-nm telescope which was a General Optics 1.5-inch concave sphere with a 2-meter radius of curvature. The multilayer

coating for this optic was deposited at MSFC by Palmer Peters a few weeks before launch.¹⁵

Table 2. MSSTA Herschelian specifications.

Wavelength	Diameter	Focal Length
4.4, 14.3 nm	4.0 cm	1.4 m
5.47, 15.0, 28.4 nm	4.0 cm	1.0 m
9.39 nm	5.0 in	1.0 m
18.0 nm	1.5 in	1.0 m
19.3, 21.1 nm	4.0 in	1.4 m

Pre-Flight Focussing

The two Cassegrain telescopes and three of the six Ritchey-Chrétien telescopes were tested interferometrically for position of best focus at MSFC. (The 28.4- and 121.6-nm telescopes were unavailable for testing, and the 155.0-nm telescope required special handling, described later in this section.) A Zygo PTI Fizeau interferometer, using a Helium-Neon laser (632.8 nm) as its coherent light source, produced interferograms which were captured with a frame grabber (installed in an IBM-AT equipped with an Intel Inboard 386 processor and an EGA monitor and video card). These interferograms were then analyzed using MicroFringe 3.1 code. Because of the existence of the central obscuration, spider mount and multilayer sector boundaries on these telescopes, the interferogram contained many artifacts that the code was unable to recognize. The interference patterns were digitized by hand. The entire set-up was laid out on a 5' x 9' Microflat granite table as shown in Figure 1.

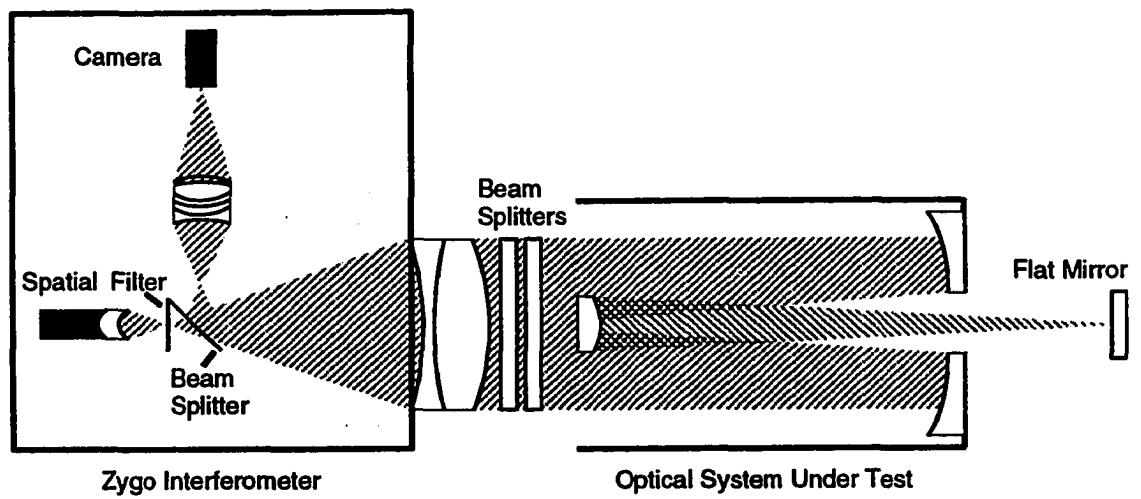


Figure 1. Determination of back focus position.

With a precision (1/20 wave) flat reference mirror reflecting the beam back through the optical system under test, each fringe in the interferogram represents 1/2 wave of wavefront deformation. After the flat mirror was moved to the point where MicroFringe 3.1 reported the flattest wave front, that position was then used as the position of best focus and, therefore, the camera film plane. The position of best focus for any telescope was found repeatedly to within 0.001 inch. The modulation transfer function of the two Cassegrain telescopes, as calculated from the interferograms, is shown in Figures 2 and 3, where a normalized spatial frequency of unity represents a diffraction-limited resolution of 2.5 arc s (at 632.8 nm). Based on these results, the telescopes are expected to have achieved the sub-arc second resolution desired at their respective operational wavelengths.

Table 3. Visible-light resolutions of the two mirrored telescopes.

Telescope	Resolution
15.0 nm	7.1 arc s
19.3 nm	7.1 arc s
30.4 nm	7.1 arc s
17.3 nm	8.3 arc s
21.1 nm	6.7 arc s

The approximate visible-light resolutions of the telescopes are listed in Table 3. These calculations serve as a base-line for the photographic tests performed at the launch site and described later in this chapter. The resolutions are calculated for a

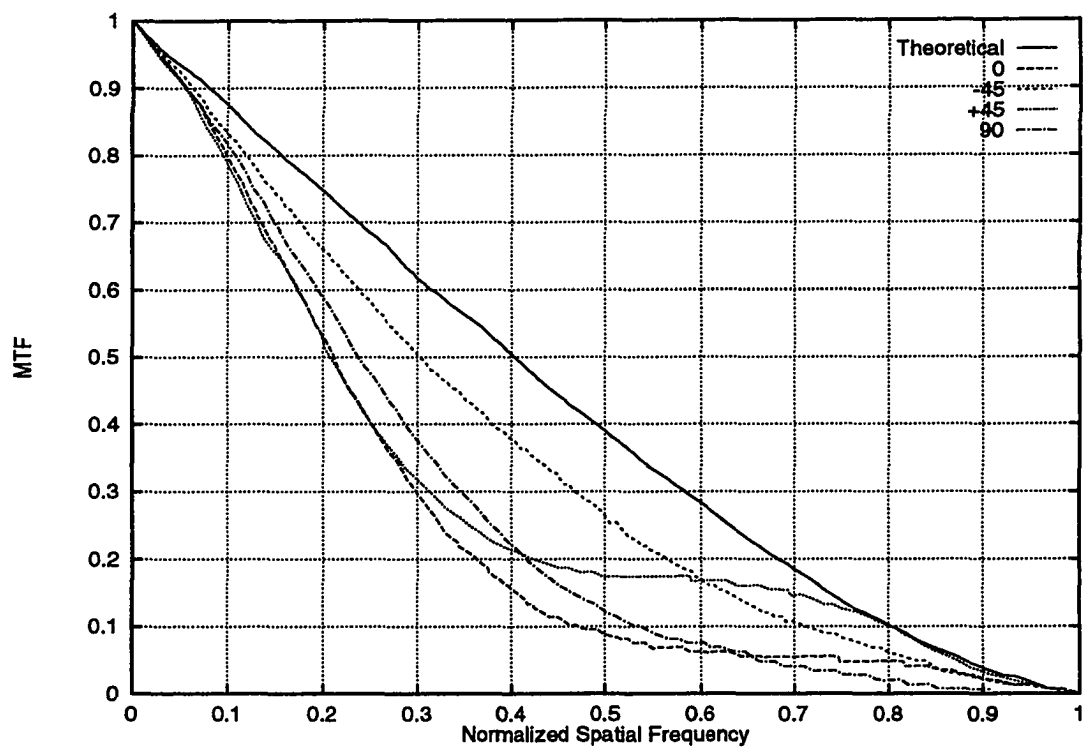


Figure 2. Modulation transfer function of the 17.3 nm Cassegrain.

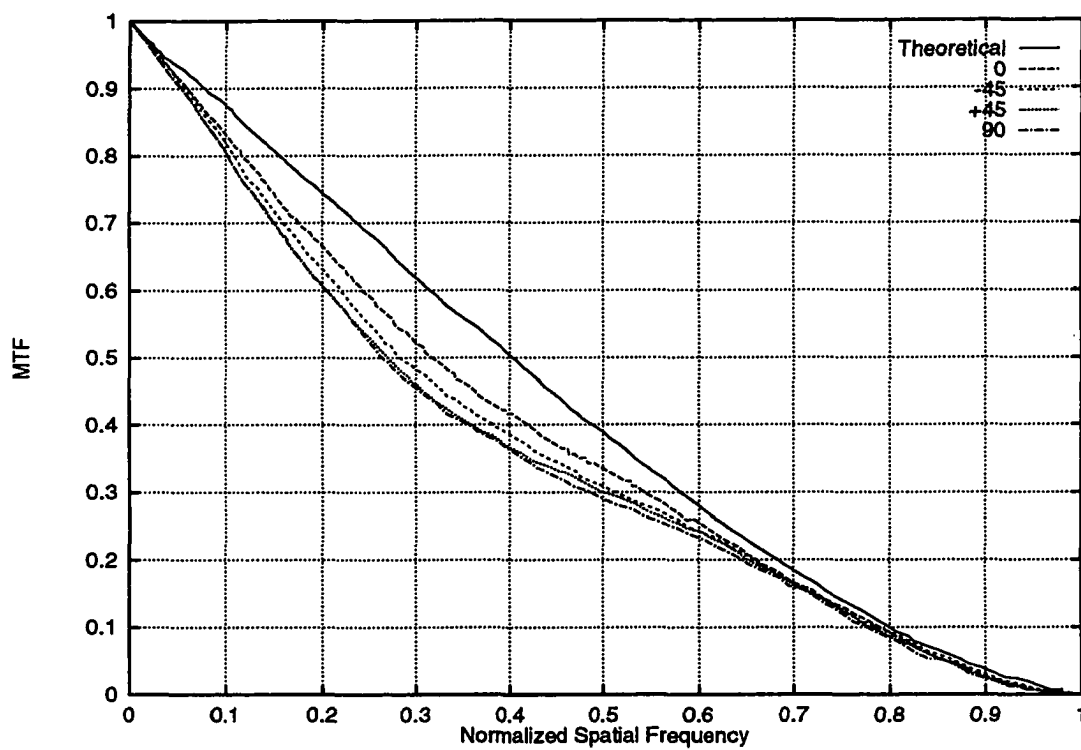


Figure 3. Modulation transfer function of the 21.1 nm Cassegrain.

modulation transfer function of 0.4 as the detector (photographic film) requires this level of contrast to faithfully record an image.

The 155.0-nm Ritchey-Chrétien telescope was coated by Acton Research Corporation with a dielectric layer stack that has such a low reflectivity at the red He-Ne laser line that the multi-pass interferometer was unable to record an interference pattern. The conventional knife-edge test was performed instead. This test has a somewhat lower accuracy in determining the position of best focus; however, the 155.0-nm Ritchey-Chrétien telescope operates at such a long wavelength that the depth of focus of the system is significantly greater than for the EUV instruments.³

In-Field Focussing

The telescopes were transported to White Sands Missile Range, placed into the MSSTA II payload, and mated with their cameras. To aid in focusing, a 16-inch Schmidt-Cassegrain collimator with a 180-inch focal length was used to illuminate the payload. This collimator was aligned and focussed using a 6-inch cube's corner retro-reflector while a 10 arc s pinhole was placed in its object plane.

To perform "in-the-field" focusing, a Standard 1951 Air Force High Resolution test target was placed in the object plane of the collimator. As shown in Figure 4, a Gaertner traveling microscope, fitted with a razor blade in its object plane obscuring part of its field of view, was then used to view the image of the resolution test target produced by each telescope.

The position of best focus was chosen to be the location of the razor blade where the microscope showed the sharpest image. This position was reproducible to

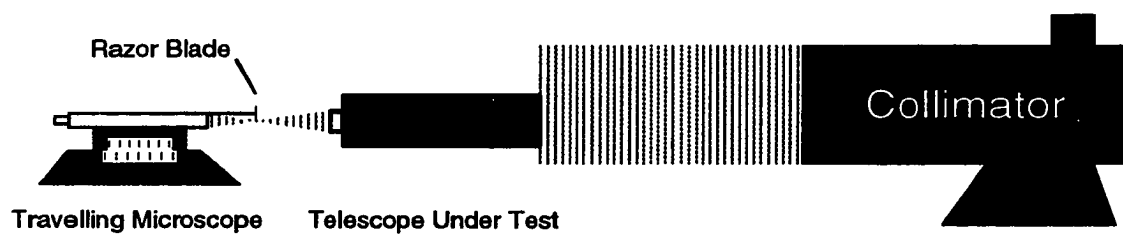


Figure 4. Locating back focus position with a Gaertner travelling microscope.

within 0.04 inches. After the cameras were mounted with their film planes in the correct position, photographs were taken of the resolution test target. A summary of the data is presented in Table 4.

Originally, due to the lower accuracy of this test, this method of focusing was only to be performed on the 13 telescopes that were not or could not be interferometrically tested at MSFC. After the payload had been vibration tested, it was found that three of the secondary mirrors of the Ritchey-Chrétiens had moved (those of the 19.3, 28.4, and 30.4 nm telescopes). The mirrors were repositioned within their cells and held in place with vacuum-compatible Dow Corning Silastic RTV. The back focus position was then re-determined with the traveling microscope.

In the case of the Ritchey-Chrétiens, all telescopes performed within approximately a factor of two of the diffraction limit. The Herschelien telescopes' resolutions varied widely due to some being used further off axis than originally designed. This can be seen in Table 4 where one value of resolution is quite different than the value in the orthogonal direction. The 18.0-nm Herschelien, being a spherical optic, performs worse for off-axis input field angles than the paraboloids.

Summary of Visible Light Testing

The MSSTA II payload with its complement of 19 telescopes was assembled and optically tested at White Sands Missile Range in the visible wavelengths before flight. Five of the two-mirrored systems were focussed interferometrically. The modulation transfer functions elucidated by the analysis of the telescopes' interferograms at the position of best focus indicated the ability of those telescopes to attain

Table 4. Visible light resolution test results.

Telescope	Horizontal (arc s)	Vertical (arc s)
Ritchey-Chrétien (D.L. = 1.2 arc s)		
15.0 nm	1.2	1.4
19.3 nm	2.8	1.4
28.4 nm	1.3	3.2
121.6 nm	4.5	2.0
155.0 nm	1.3	3.6
Cassegrain (D.L. = 2.4 arc s)		
17.3 nm	8.0	6.3
4.0 cm Herschelians (D.L. = 3.8 arc s)		
4.4 nm	4.0	5.6
5.47 nm (β)	41.0	35.8
5.47 nm (η)	3.2	4.0
14.3 nm	4.5	8.0
15.0 nm (δ)	5.6	4.0
15.0 nm (ϵ)	18.0	6.3
28.4 nm	4.5	8.0
4.0 in Herschelians (D.L. = 1.5 arc s)		
19.3 nm	2.0	5.0
21.1 nm	2.0	3.6
5.0 in Herschelian (D.L. = 1.2 arc s)		
9.39 nm	12.7	3.6
1.5 in Herschelian (D.L. = 4.0 arc s)		
18.0 nm	25.3	25.3

(D.L. = Diffraction limit at 632.8 nm. Horizontal and vertical resolutions are arbitrary, orthogonal directions in the image plane. Greek letters denote different telescopes coated for the same wavelength.)

roughly half of their diffraction-limited resolutions. The 155.0-nm Ritchey-Chrétien was focussed using a conventional knife edge test because of the low reflectivity of the coating at 632.8 nm.

All telescopes were then aligned and checked for focus in situ using a Diffraction Limited 16-inch collimator which projected either a pinhole for alignment or a Standard 1951 Air Force High Resolution test target. All of the Ritchey-Chrétien telescopes performed admirably, as did a number of the Herschelien telescopes. The difference in calculated resolution versus observed resolution at visible wavelengths may stem from the fact that the film used for the tests (SO-253) was able to record images at lower contrasts levels than expected. With these performances, it is not unreasonable to expect that many of the telescopes attained the sub arc-second resolution for which they were designed.

Images taken on this flight are still being analyzed, but it appears that the 155.0-nm Ritchey-Chrétien did yield sub-arc second resolution of structures in the chromosphere.¹⁶ The resolution test target images were recently digitized by Dr. Dennis Martínez-Galarce, and the revised resolution results are to be published shortly.¹⁷

Filters

The filters currently used in the MSSTA payload are thin films of various elements deposited on a support structure of 83% transmissive nickel mesh.¹⁸ These filters function by attenuating and reflecting radiation below the conduction frequency. At the short-wavelength cut-off, the process of inelastic scattering with an inner shell electron is used to absorb unwanted radiation.

The materials used for filters on the last flight of the MSSTA were chosen to meet the requirements of rejecting radiation outside of the desired passband. Where possible, the passband of the filters were made narrower by taking advantage of

a material's absorption edge. The filters were tested at the Stanford Synchrotron Radiation Laboratory (SSRL), and the data¹⁹ for the five filters flown are given in Table 5 and Figures 5-9.

Table 5. Thin film filters for MSSTA II.

Filter	Peak λ	Max T.	FWHM	Composition	Telescopes
94-1	17.2	11.4%	2.6	170 Al, 110 Y, 45 C	17.3, 19.3, 21.1
94-2	16.8	9.6%	2.3	160 Al, 150 Y, 45 C	21.1
94-3	16.9	32.9%	5.0	200 Al, 40 C	18.0, 28.4, 30.4
94-4	8.1	4.4%	2.6	300 Y, 150 Nb, 20 C	9.39, 12.8, 14.3, 15.0
94-5	5.3	13.2%	0.19	100 Al, 250 C, 250 Phth	5.47

Wavelengths and thicknesses are in (nm). Phth is phthalocyanine.

The method by which these thin film filters operate makes it difficult to optimize them for a specific wavelength and to reduce their full width at half maximum. Fabry-Perot interferometers are much better adapted to tuning both peak wavelength and full width at half maximum.

A Fabry-Perot filter utilizes a resonant cavity that reinforces radiation at integer multiples of a fundamental frequency and uses destructive interference to suppress other frequencies. If the resonance cavity is constructed of a single slab of material, it is called an "etalon." The primary characteristic of a Fabry-Perot filter is its etalon thickness.

A Fabry-Perot's band-pass can be significantly reduced by using the properties of interference. An etalon of thickness, d , combines wavefronts from multiple

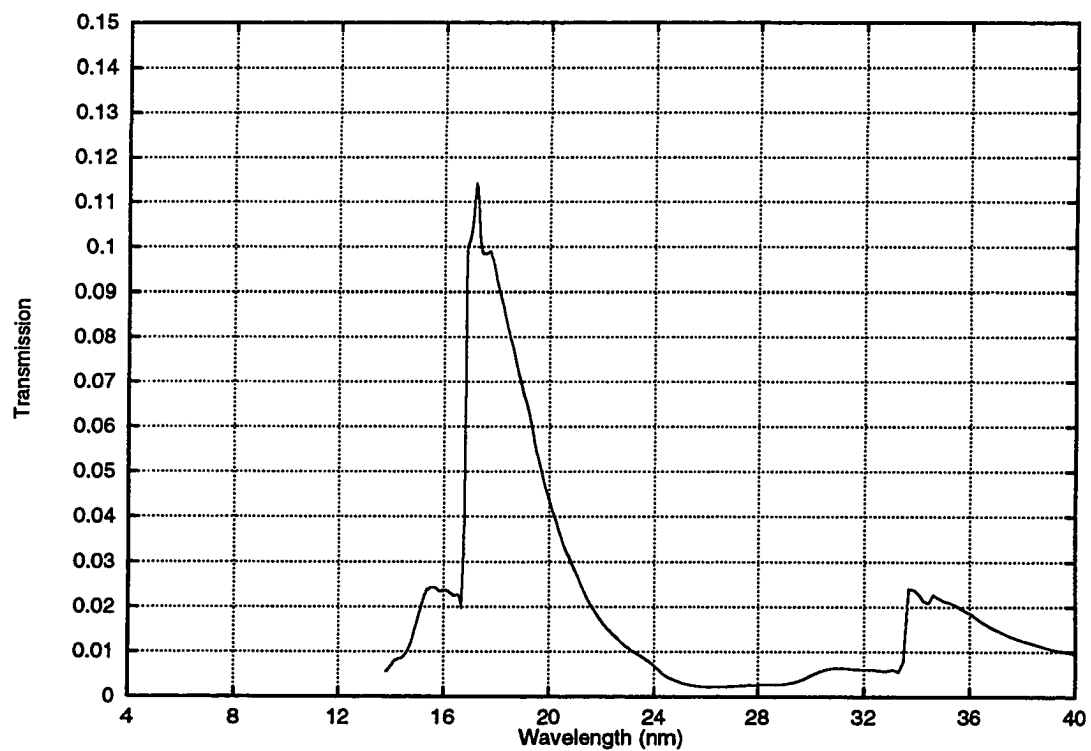


Figure 5. Filter 94-1.

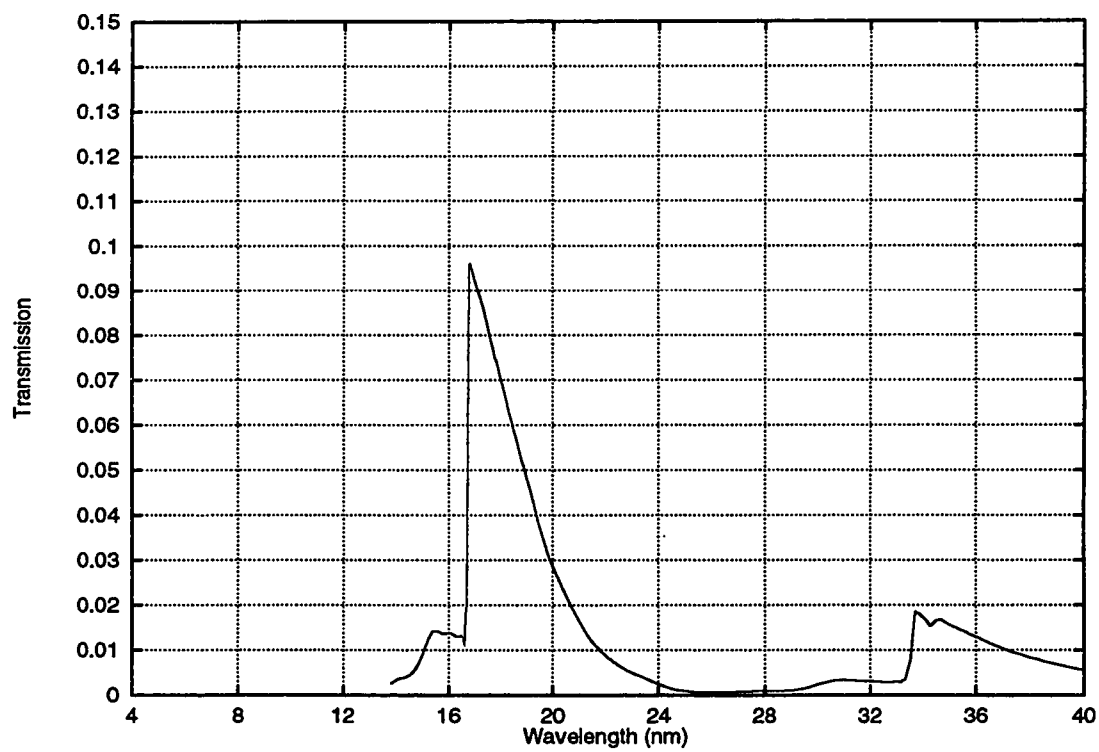


Figure 6. Filter 94-2.

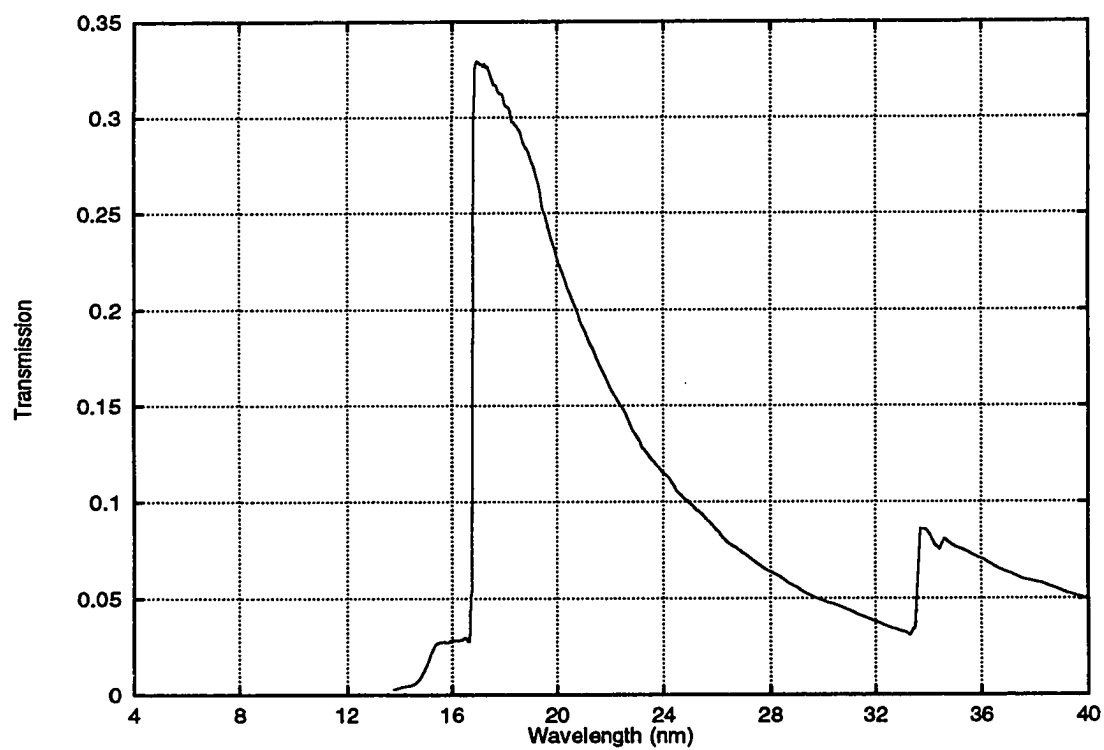


Figure 7. Filter 94-3.

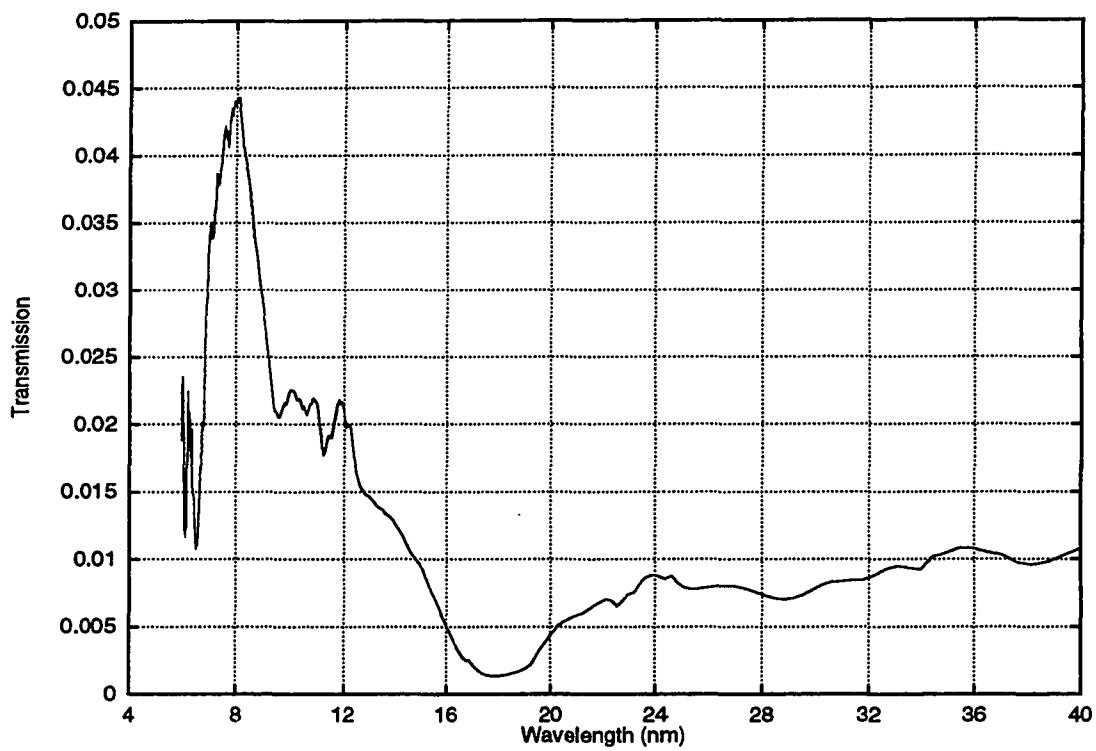


Figure 8. Filter 94-4.

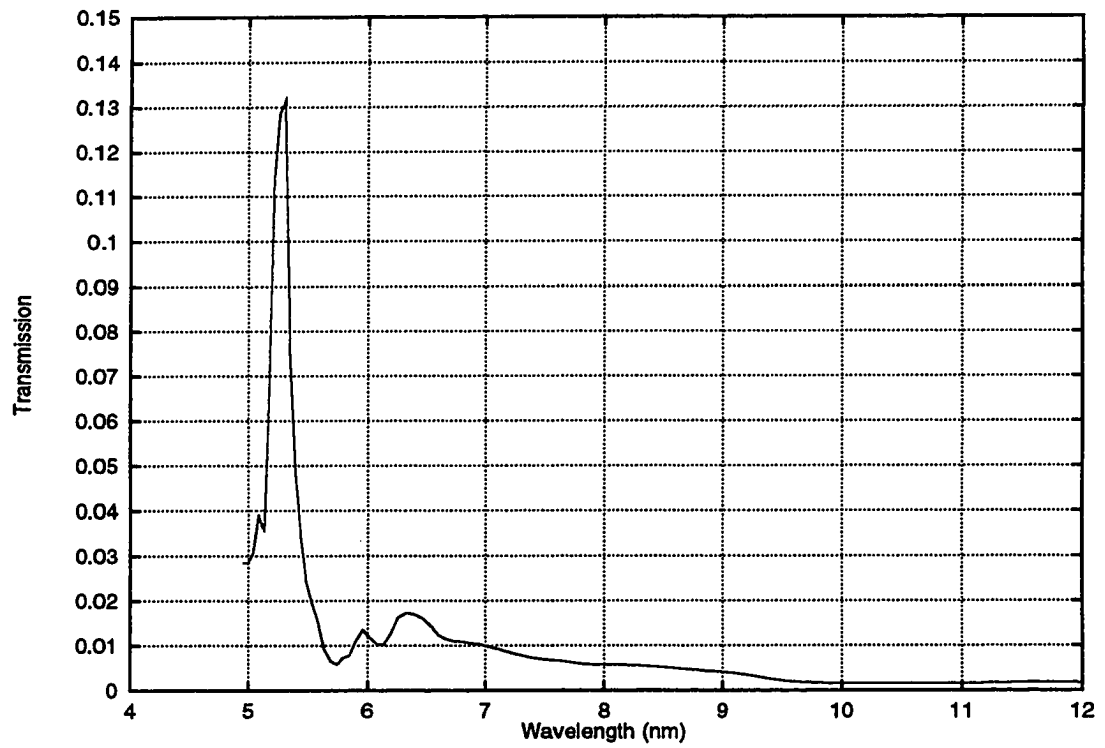


Figure 9. Filter 94-5.

reflections at its surfaces. Using the matrix formalism outlined in the next chapter, the transmission of a Fabry-Perot filter is

$$T = \frac{T_i^2}{(1 - R_i)^2 + 4R_i \sin^2\left(\frac{y}{2}\right)} \quad (1)$$

where T_i and R_i are the transmissivity and reflectivity at the surfaces of the spacer layer, n is the index of refraction of the spacer layer, and y is twice the phase thickness of the spacer ($y = \frac{4\pi dn}{\lambda}$). The maximum and minimum transmission through the filter are

$$T_{max} = \frac{T_i^2}{(1 - R_i)^2} \quad \text{when} \quad \lambda = \frac{2nd}{m} \quad (2)$$

$$T_{min} = \frac{T_i^2}{(1 + R_i)^2} \quad \text{when} \quad \lambda = \frac{4nd}{m} \quad (3)$$

where m is a positive integer greater than zero.

The transmission can be re-written as

$$T = \frac{T_{max}}{1 + F \sin^2\left(\frac{y}{2}\right)}. \quad (4)$$

This is known as the Airy Formula where

$$F = \frac{4R_i}{(1 - R_i)^2}. \quad (5)$$

As long as λ is within ± 0.1 of its value at T_{max} , $\frac{y}{2}$ can be considered a small angle. The full width at half maximum in y is then $\frac{4}{\sqrt{F}}$. Converting the domain from y to λ , the full width at half maximum is

$$\text{FWHM} \approx \frac{4\pi dn \sqrt{F}}{m^2 \pi^2 F - 1}. \quad (6)$$

From equations (2) and (6) it can be seen that the full width at half maximum is, roughly, inversely proportional to m , and can be reduced by adding thickness to the

spacer. However, in an absorptive medium, this needs to be balanced against the exponential loss of flux with increasing thickness.

In addition to the issue of absorption, many other optical design criteria must be considered. The most important of these include increasing the reflectivity of the optic, determining the optical constants of materials, understanding the effect optical interfaces have on the efficiency of the optic, and choosing the materials to be used in the construction of the filter.

DESIGN

As wavelengths decrease, optical constants approach unity. Because reflectivity at an interface depends on the ratio of optical constants on either side, reflectivity decreases with wavelength. One popular method of overcoming this deficiency is to increase the number of interfaces and space them such that reflected radiation from one interface adds in phase with radiation reflected from interfaces deeper in the stack. Optics utilizing this method to increase reflectivity are called "multilayers."

The optical constants of the materials composing the layers are a function of wavelength and, as wavelength decreases, the index of refraction is affected more by the number density of particular elements than by the presence of particular compounds. The dominant optical property of the elements stems from treating the associated electrons as a collisionless plasma. The correct optical constants are then derived by determining a complex number representing the number of "free" electrons per atom. This approximation becomes better as frequencies increase (wavelengths decrease).

Even though the optical constants may be known, the morphology of the interface becomes important if the change in optical constants occurs over a distance greater than an appreciable fraction of the wavelength of radiation. Interfaces which do not occur within a negligible fraction of the wavelength of radiation are considered "rough" and decrease the reflectivity of the interface. Interdiffusion between layers can easily form rough interfaces, and such roughness must be taken into account.

Also important is the choice of materials. A Fabry-Perot's pass-band becomes narrower with increasing etalon thickness; however, absorption of radiation also increases with thickness. The material chosen for the etalon must be low in absorption, and the complement material must not only form an interface with a relatively high reflectivity, but must also aid in rejection of wavelengths outside of the desired pass-band. In addition, the two materials should not readily intermix, nor should they be susceptible to oxidation.

Multilayers

A simple dielectric multilayer stack consists of two media of differing indices of refraction, n , alternating with layer number, l . Figure 10 is a schematic of three layers inside such a stack.

At each interface there is reflection and transmission of radiation. The materials are chosen such that, at each interface, the Fresnel coefficients predict high reflectivities. Reflection may be weak at the interface between a single layer pair, but many such interfaces raise the total reflection of the stack appreciably if the reflected wavefronts interfere constructively. Layer thicknesses, d_l , are therefore chosen such that reflected light adds in phase at each interface. This requires, for radiation of vacuum wavelength λ in non-absorptive media, that

$$d_l = (2m + 1) \frac{\lambda}{4n_l} \left[1 - \left(\frac{n_{l-1}}{n_l} \sin \theta \right)^2 \right]^{-\frac{1}{2}} \quad (7)$$

where m is an integer representing the order of reflection and θ is the incident angle of the incoming light. This equation was derived by requiring that the phase of two

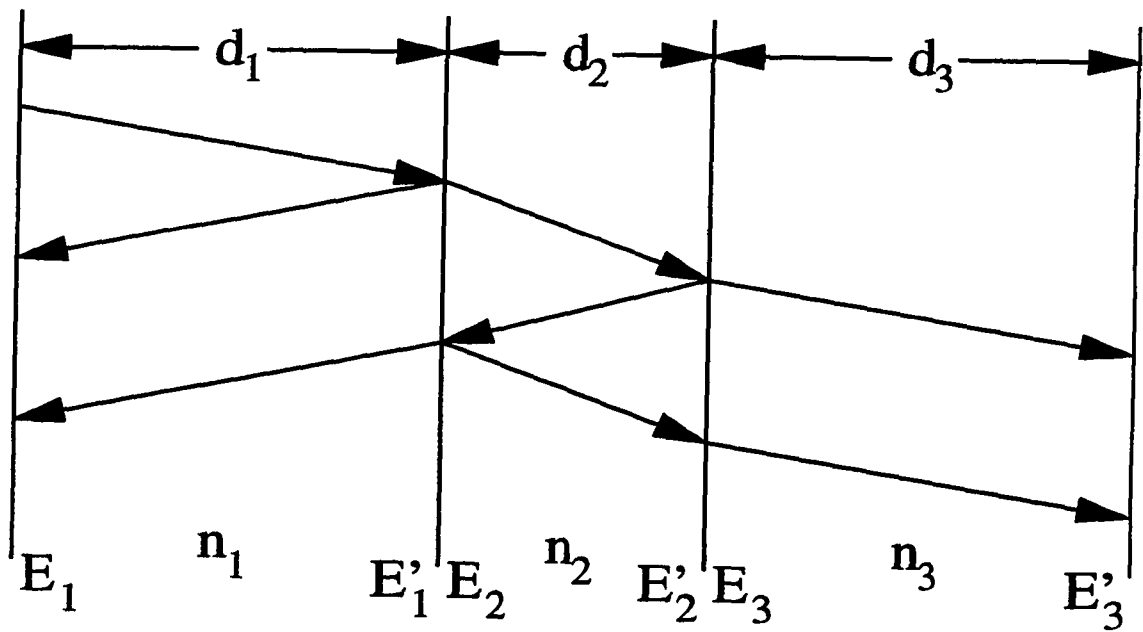


Figure 10. Schematic of three layers inside a multilayer optical stack.

rays differ by a factor of $2m\pi$. The first ray is reflected from the forward interface of one layer. The second ray traverses that layer, reflects off of the following interface, re-traverses the layer, and exits the original interface.

If the approximation is made such that the indices of refraction are that of vacuum (unity) and the normal incidence angle, θ , is replaced with the grazing incidence angle, $\Theta = 90 - \theta$, equation (7) reduces to Bragg's law for x-ray crystals:

$$2D \sin \Theta = N\lambda \quad (8)$$

where D is the layer period and N is an integer called the "Bragg Order." This is useful in x-ray diffractometry of periodic structures where the indices of refraction are close enough to unity to utilize this law for determination of layer pair thickness from plots of reflectivity versus grazing incidence angle.

The properties of a stack consisting of l layers can be quickly calculated numerically via a matrix formalism²⁰ where the (possibly complex) index of refraction of the medium, thickness of the medium, and incident angle of radiation are the only independent variables.

For a simple, three-layer stack (as depicted in Figure 10), calculating the transmission through layer 2 can be done via matrix mechanics:

$$\vec{E}'_1 = \tilde{S} \vec{E}_3 \quad (9)$$

where $\vec{E}'_1 = \begin{pmatrix} E'_{l1} \\ E'_{r1} \end{pmatrix}$ represents the leftward and rightward propagating electric field at the *right*-hand side of layer 1 and $\vec{E}_3 = \begin{pmatrix} E_{l3} \\ E_{r3} \end{pmatrix}$ represents the leftward and rightward propagating electric fields at the *left*-hand side of layer 3. \tilde{S} is the 2×2 stack matrix

which yields the transformation. Because $\frac{E_{t3}}{E_{r1}}$ represents the transmitted electric field and $\frac{E'_{r1}}{E_{r1}}$ the reflected field,

$$\tau_{stack} = S_{22}^{-1} \quad \text{and} \quad \rho_{stack} = S_{12} S_{22}^{-1} \quad (10)$$

where τ_{stack} and ρ_{stack} are the Fresnel transmission and reflection coefficients, respectively, for the stack. The stack matrix itself represents the combined effect of all the optics as radiation impinges on the multilayer stack. In the case of this simple, three layer stack, it can be factored into

$$\tilde{S} = \tilde{I}_{12} \tilde{P}_2 \tilde{I}_{23} \quad (11)$$

where

$$\tilde{I}_{ij} = \frac{1}{\tau_{ij}} \begin{pmatrix} 1 & \rho_{ij} \\ \rho_{ij} & 1 \end{pmatrix} \quad (12)$$

and describes the physics at the interface of layers i and j where τ_{ij} and ρ_{ij} are the Fresnel coefficients of transmission and reflection at the interface.

Propagation of a ray through a layer, j , is described by the matrix

$$\tilde{P}_j = \begin{pmatrix} e^{-i\phi_j} & 0 \\ 0 & e^{i\phi_j} \end{pmatrix}, \quad \phi_j = \frac{2\pi}{\lambda} n_j d_j \cos \theta_j \quad (13)$$

where θ_j is the angle the ray makes with the surface normal. Carrying out the multiplication,

$$\begin{aligned} \tilde{S} &= \frac{1}{\tau_{12}\tau_{21}} \begin{pmatrix} 1 & \rho_{12} \\ \rho_{12} & 1 \end{pmatrix} \begin{pmatrix} e^{-i\phi_2} & 0 \\ 0 & e^{i\phi_2} \end{pmatrix} \begin{pmatrix} 1 & \rho_{21} \\ \rho_{21} & 1 \end{pmatrix} \\ &= \frac{1}{\tau_{12}\tau_{21}} \begin{pmatrix} e^{-i\phi_2} + \rho_{12}\rho_{21}e^{i\phi_2} & \rho_{21}e^{-i\phi_2} + \rho_{12}e^{i\phi_2} \\ \rho_{12}e^{-i\phi_2} + \rho_{21}e^{i\phi_2} & \rho_{12}\rho_{21}e^{-i\phi_2} + e^{i\phi_2} \end{pmatrix}; \end{aligned}$$

thus,

$$\begin{aligned}\tau_{stack} &= \frac{\tau_{12}\tau_{21}}{\rho_{12}\rho_{21}e^{-i\phi_2} + e^{i\phi_2}} \\ \rho_{stack} &= \frac{\rho_{21}e^{-i\phi_2} + \rho_{12}e^{i\phi_2}}{\rho_{12}\rho_{21}e^{-i\phi_2} + e^{i\phi_2}}.\end{aligned}\tag{14}$$

Such methods are easily formatted into computer executable code and can be used to optimize multilayer stacks with tailored pass-bands. Recently, work has been done to create multilayer filters with pass-bands showing Chebychev features (as has been done with electronics filters) in the infrared with non-absorbing materials.²¹

Optical Constants

When absorption is present in materials, they must be described by complex indices of refraction, \tilde{n} . Calculating these indices properly is important if an accurate model is to be made. According to Henke *et al*,²² the complex index of refraction of a material may be represented by

$$\tilde{n} = n - ik = 1 - \delta - i\beta\tag{15}$$

where

$$\begin{aligned}\delta &= \frac{r_e}{8\pi^2\epsilon_0}\lambda^2 \sum_a \rho_a f_{1,a} \\ \beta &= \frac{r_e}{8\pi^2\epsilon_0}\lambda^2 \sum_a \rho_a f_{2,a}.\end{aligned}\tag{16}$$

The material, composed of atoms with number density ρ_a , is considered a collisionless plasma with $\tilde{f} = f_1 + if_2$ “free” electrons (of radius r_e) per atom. λ is the wavelength of incident radiation.

Theoretically determining \tilde{n} for a metal is done by calculating its “dielectric constant,” ϵ . The equation of motion of a free electron in a metal is governed by the driving force created by the oscillating electric field and local damping effects:

$$m \frac{d^2 \vec{r}}{dt^2} + m\gamma \frac{d\vec{r}}{dt} = q\vec{E}_0 e^{i\omega t} \quad (17)$$

where m is the mass of the electron, q its charge, \vec{r} is its displacement, γ is a damping constant, and $\vec{E}_0 e^{i\omega t}$ is the electric field of the incoming electro-magnetic wave.

Choosing a harmonic solution for \vec{r} ,

$$\vec{r}(t) = \vec{r}_0 e^{i\omega t} = \frac{q/m}{i\gamma\omega - \omega^2} \vec{E}_0 e^{i\omega t} \quad (18)$$

which has a dipole moment of

$$q\vec{r}_0 = \frac{q^2/m}{i\gamma\omega - \omega^2} \vec{E}_0 \quad (19)$$

yields a polarization in the material of

$$\vec{P} = \frac{\rho q^2/m}{i\gamma\omega - \omega^2} \vec{E}_0 \quad (20)$$

where ρ is the density of free electrons.

From the wave equation,

$$n = \sqrt{\frac{\mu\epsilon}{\mu_0\epsilon_0}}. \quad (21)$$

Assuming non-magnetic, linear media, this may be re-written

$$\begin{aligned} \tilde{n}^2 &= 1 + \frac{|\vec{P}|}{\epsilon_0 |\vec{E}|} \\ &= 1 - \frac{\omega_p^2}{\omega^2 + \gamma^2} - i \left(\frac{\gamma}{\omega} \right) \frac{\omega_p^2}{\omega^2 + \gamma^2} \end{aligned} \quad (22)$$

where ω_p is the plasma frequency, $\frac{\rho q^2}{m\epsilon_0}$.

Given that $\tilde{n}^2 = (n - ik)^2$,

$$\begin{aligned} n^2 - k^2 &= 1 - \frac{\omega_p^2}{\omega^2 + \gamma^2} \\ 2nk &= \left(\frac{\gamma}{\omega}\right) \frac{\omega_p^2}{\omega^2 + \gamma^2}. \end{aligned} \quad (23)$$

Approximation to a collisionless plasma is equivalent to setting $\gamma = 0$. This yields

$$n^2 = 1 - \frac{\omega_p^2}{\omega^2}. \quad (24)$$

At extreme ultraviolet wavelengths, $\omega^2 \gg \omega_p^2$. Setting $n = 1 - \delta$, an approximation may be made:

$$n^2 \approx 1 - 2\delta, \quad \delta = \frac{\omega_p^2}{2\omega^2}. \quad (25)$$

And δ can be expressed as

$$\delta = \frac{r_e}{8\pi^2\epsilon_0} \lambda^2 \rho \quad (26)$$

where r_e is the classical electron radius ($\frac{q_e^2}{m_e c^2}$).

Henke *et al.*²² state that any element can be treated in this fashion by choosing ρ correctly. Henke defines a constant \tilde{f} to be the fraction of “free” electrons per atom. To account for absorption, \tilde{f} is complex ($\tilde{f} = f_1 + if_2$). Therefore, for any particular species of atom in a compound,

$$\delta_a = \frac{r_e}{8\pi^2\epsilon_0} \lambda^2 \rho_a \tilde{f}_a \quad (27)$$

where ρ_a is the density of the given atom, a , in the compound.

Furthermore, Henke states that the δ_a are superimposable:

$$\delta = \frac{r_e}{8\pi^2\epsilon_0}\lambda^2 \sum_a \rho_a \tilde{f}_a. \quad (28)$$

Much of the modeling that follows utilizes index of refraction information extrapolated from Henke's experimental values of \tilde{f} .

Materials where $\beta \neq 0$ induce two effects on the reflection of radiation. First, power is lost in traversing the system. Power loss in absorptive materials defines a maximum number of periods viable for a reflector. As one goes deeper into the optical stack, less radiation is available because of dissipation in earlier layers; thus, deeper layers contribute less reflected energy. In a mirror, additional layers may not contribute, but they are not detrimental to the performance of the optic. For a transmission filter, however, additional layers reduce throughput. The number of layers to be included in the filter was settled based on computational modeling. In addition, reflection at interfaces no longer results in phase changes of 0 or π . This requires a different optimization for multilayer structures than the $\frac{\lambda}{4}$ layers described for non-absorbing media. Vinogradov and Zeldovich²³ derived the following equation for the optimum ratio, γ_{opt} , of the thickness of high-absorption material to the total thickness of a high-absorption/low-absorption pair:

$$\tan(\pi\gamma_{\text{opt}}) - \pi \left(\gamma_{\text{opt}} + \frac{n_l k_l}{n_h k_h - n_l k_l} \right) = 0 \quad (29)$$

where n_h , k_h , n_l , and k_l are the real index of refraction and absorption for the high-absorption and low-absorption materials, respectively.

Interfacial Roughness

Because multilayer optics depend on reflection and transmission at interfaces between materials, it is important to consider the geometry of those interfaces. In particular, we are interested in the optical effects of a particular dielectric function, $\epsilon(\vec{x})$.

If the dielectric constant of the material changes from its initial value, ϵ_0 , to its final value, ϵ' , within a distance smaller than the wavelength of radiation considered, the interface may be approximated as a step function, and reflection and transmission at an interface may be calculated from the boundary conditions at the interface. This approximation is certainly viable for optics to be used at visible and longer wavelengths. However, as wavelengths decrease, tolerances on “perfect” interfaces also decrease to the point where even minor interdiffusion between materials forces one to inquire about the optical effects of an arbitrarily wide interface. The formalism to follow is adapted from Stearns²⁴.

An electric field

$$\vec{E}^0(\vec{x}, t) = \vec{E}_0 e^{i\vec{k}_0 \cdot \vec{x}} e^{i\omega t} \quad (30)$$

impinging on an arbitrary interface satisfies the homogeneous wave equation

$$(\vec{\nabla}^2 + \vec{k}^2)\vec{E}^0(\vec{x}) = 0. \quad (31)$$

The displacement field in a linear, non-magnetic medium obeys the relation

$$(\vec{\nabla}^2 + \vec{k}^2)\vec{D}(\vec{x}) = -\vec{\nabla} \times \vec{\nabla} \times (\vec{D}(\vec{x}) - \epsilon_0 \vec{E}(\vec{x})). \quad (32)$$

The displacement field may be considered a superposition of the field scattered by the change in ϵ and the field not scattered

$$\vec{D} = \vec{D}^{sc} + \vec{D}^0. \quad (33)$$

The non-scattered case implies $\vec{D}^0 = \epsilon' \vec{E}$; hence, $(\vec{\nabla}^2 + \vec{k}^2) \vec{D}^0 = 0$ and

$$\begin{aligned} (\vec{\nabla}^2 + \vec{k}^2) \vec{D}^{sc}(\vec{x}) &= -\vec{\nabla} \times \vec{\nabla} \times (\vec{D}(\vec{x}) - \epsilon_0 \vec{E}(\vec{x})) \\ &= -\vec{\nabla} \times \vec{\nabla} \times (\epsilon(\vec{x}) \vec{E}(\vec{x}) - \epsilon_0 \vec{E}(\vec{x})) \\ &= -\vec{\nabla} \times \vec{\nabla} \times \alpha(\vec{x}) (\vec{E}^0(\vec{x}) + \vec{E}^{sc}(\vec{x})) \end{aligned} \quad (34)$$

where

$$\alpha(\vec{x}) = \epsilon(\vec{x}) - \epsilon_0 \quad (35)$$

and the electric field has been divided into scattered and non-scattered terms. This can be further simplified by noting that

$$\vec{\nabla}^2 \vec{E} - \frac{\epsilon \mu_0}{c^2} \frac{\partial^2}{\partial t^2} \vec{E} = \frac{1}{\epsilon} \vec{\nabla} (\vec{\nabla} \cdot \vec{P}) + \frac{\mu_0}{c^2} \frac{\partial^2}{\partial t^2} \vec{P}. \quad (36)$$

In linear media, $\vec{P} = \vec{D} - \epsilon_0 \vec{E}$. Thus, the non-scattered electric field satisfies the homogeneous version of equation (36). The polarization is non-vanishing only for \vec{E}^{sc} where $\vec{P} = \alpha(\vec{x}) \vec{E}$.

Because $\alpha(\vec{x}) \ll 1$ in the extreme ultraviolet, the right-hand side of equation (36) may be taken as small. In the Born approximation, this is taken to be small enough, in fact, to make the approximation $\vec{E}^{sc} \approx 0$. Thus

$$(\vec{\nabla}^2 + \vec{k}^2) \vec{D}^{sc}(\vec{x}) \approx -\vec{\nabla} \times \vec{\nabla} \times \alpha(\vec{x}) \vec{E}^0(\vec{x}). \quad (37)$$

Stearns prefers to solve equation (37) in Fourier space, with the result

$$\vec{D}^{sc}(\vec{x}) = \frac{1}{(2\pi)^3} \int \int \int [(\hat{s} \times \vec{E}_0) \times \hat{s}] \tilde{\alpha}(\vec{s} - \vec{k}_0) \frac{s^2}{s^2 - k^2} e^{i\vec{s} \cdot \vec{x}} d^3 s. \quad (38)$$

Defining $\Delta = \epsilon' - \epsilon_0$,

$$\alpha(\vec{x}) = \begin{cases} 0 & z \rightarrow \infty \\ \Delta & z \rightarrow -\infty \end{cases}. \quad (39)$$

The normalized derivative of $\alpha(\vec{x})$ in the \hat{z} direction can also be used as a description of the interface:

$$g(\vec{x}) = \frac{1}{\Delta} \frac{\partial \alpha(\vec{x})}{\partial z} = \frac{1}{\Delta} \frac{\partial \epsilon(\vec{x})}{\partial z}. \quad (40)$$

The $z = 0$ plane is defined by requiring

$$\int z g(\vec{x}) d^3 x = 0. \quad (41)$$

Notice, for some region $-\frac{X}{2} < x < \frac{X}{2}$, $-\frac{Y}{2} < y < \frac{Y}{2}$,

$$\int_{-\frac{Y}{2}}^{\frac{Y}{2}} \int_{-\frac{X}{2}}^{\frac{X}{2}} \int_{-\infty}^{\infty} g(\vec{x}) dz dy dx = XY = A. \quad (42)$$

Over a small enough region ($\Delta x, \Delta y < \lambda$), the specular field only depends on the average variation of the dielectric function. Thus, we may introduce an average profile function

$$\begin{aligned} p(z) &= \frac{1}{\Delta} \frac{\int \int [\epsilon(\vec{x}) - \epsilon'] dx dy}{\int \int dx dy} \\ &= \frac{1}{A\Delta} \int \int [\epsilon(\vec{x}) - \epsilon'] dx dy. \end{aligned} \quad (43)$$

The derivative of the average profile function is simply defined as

$$w(z) = \frac{dp(z)}{dz}. \quad (44)$$

By separating \vec{k} into a magnitude, k , and unit vector, \hat{n} , Stearns solves equation (32) for both reflection and transmission of a given polarization, \hat{E} . For reflection,

$$\hat{E}^* \cdot \vec{E}^r(\vec{x}) = \frac{\Delta k^2}{8\pi^2 \epsilon_0} (\hat{E}^* \cdot \vec{E}_0) \int \int \frac{\tilde{g}(\vec{k} - \vec{k}_0)}{n_z(n_z - n_z^0)} e^{i\vec{k} \cdot \vec{x}} dn_x dn_y. \quad (45)$$

For transmission,

$$\hat{E}^* \cdot \vec{E}^t(\vec{x}) = -\frac{\Delta k'^3}{8\pi^2 \epsilon'} (\hat{E}^* \cdot \vec{E}_0) \int \int \frac{\tilde{g}(\vec{k}' - \vec{k}_0)}{n_z(k'_z - k_z^0)} e^{i\vec{k} \cdot \vec{x}} dn_x dn_y. \quad (46)$$

It is important that these results reduce to known reflectivities and transmissivities at perfect interfaces, i.e. where $g(\vec{x}) = \delta(z)$. Indeed, substituting the Fourier transform of $\delta(z)$ for the reflection integral yields

$$\hat{E}^* \cdot \vec{E}^r(\vec{x}) = \frac{\Delta}{4\epsilon_0 n_z^0{}^2} (\hat{E}^* \cdot \vec{E}_0) e^{i\vec{k}^r \cdot \vec{x}} \quad (47)$$

where

$$k_x^r = k_x^0, \quad k_y^r = k_y^0, \quad \text{and} \quad k_z^r = -k_z^0.$$

By defining $\vec{q} = \vec{k} - \vec{k}_0$ to be the momentum transfer vector for reflection ($\vec{q} = \vec{k}' - \vec{k}_0$ for transmission), we find that the specular field requires $q_x = q_y = 0$. The Fourier transform of $g(\vec{x})$ then has the form

$$\tilde{g}(\vec{q}) = \delta(q_x) \delta(q_y) g(q_z) \quad (48)$$

and

$$\tilde{g}(q_z) = A \tilde{w}(q_z) \quad (49)$$

which reduces the integrals (39) and (40) to analytic functions:

$$\hat{E}^* \cdot \vec{E}^r(\vec{x}) = r_0 \tilde{w}(q_z) e^{i\vec{k}^r \cdot \vec{x}} \quad (50)$$

and

$$\hat{E}^* \cdot \vec{E}^t(\vec{x}) = t_0 \tilde{w}(q_z) e^{i\vec{k}^t \cdot \vec{x}} \quad (51)$$

where r_0 and t_0 are the Fresnel reflection and transmission coefficients, respectively.

Both reflection and transmission are reduced by the factor $\tilde{w}(q_z)$. For transmission,

$$\tilde{w}(q_z) = \tilde{w}(k'_z - k_z^0) \approx \tilde{w}\left(-\frac{\Delta}{2\epsilon_0 n_z^0}\right) \approx 1$$

to first order in Δ . Thus, transmission is unaffected by interfacial roughness to first order in Δ . Knowing that $q_z = -2kn_z^0$, the reduction in reflection at an interface with a particular interface profile, $p(z)$, may be estimated. The standard model for classical interdiffusion of two materials yields an error function for the interface profile

$$p(z) = \frac{1}{\sqrt{\pi}} \int_{-\infty}^z e^{-\frac{t^2}{2\sigma^2}} dt. \quad (52)$$

This results in a derivative of

$$w(z) = \frac{1}{\sqrt{2\pi\sigma^2}} e^{-\frac{z^2}{2\sigma^2}} \quad (53)$$

which has the Fourier transform

$$\tilde{w}(s) = e^{-\frac{\sigma^2 s^2}{2}}. \quad (54)$$

Substituting $s = q_z = -2kn_z^0$,

$$\tilde{w}(q_z) = e^{-2\sigma^2 k^2 n_z^{02}}. \quad (55)$$

This is the famous Debye-Waller factor²⁵

$$R = R_0 e^{-2\left(\frac{2\pi\sigma \cos \alpha}{\lambda}\right)^2} \quad (56)$$

which can be incorporated into stack reflectivity calculations to model the reduction in reflectivity that results from interfacial roughness.

Computational Modeling

The code used for the initial computational modeling was written in FORTRAN 77 on a UNIX platform (Silicon Graphics IRIX 5.3 IP7). It uses the matrix formalism developed earlier²⁰ and outputs plots of either transmission or reflection versus wavelength (for bandwidth plots) or angle of incidence (for rocking-curve plots). The wavelength-dependent, complex indices of refraction are given by equation (16) where the f values are the atomic complex scattering factors published by Henke *et al.*²² The front end is written in TCL/TK to allow a simple, graphical user interface, and results are automatically plotted with Gnuplot. This code reproduces results obtained by XMC commercial code which runs in the MS DOS environment and, as a test case, reproduces the theoretical results calculated for Barbee's FPE.²⁶

Toward the end of the modeling process, the personally developed code was relinquished in favor of IMD,²⁷ software developed by Windt at Bell Laboratories. IMD is written in and runs under RSI's interactive data language (IDL) environment and is preferable due to its ability to model rough and diffuse boundaries between layers by using the formalism presented earlier and attempt to fit model parameters (such as interfacial roughness, layer thicknesses errors, γ values, etc.) to measured data.

Materials Search

The materials for the prospective filter need to satisfy five requirements. First, they must be available as sputtering targets. Second, the material used for the etalon must have as low a coefficient of absorption as possible at the wavelength of interest.

Third, the materials chosen must not combine with atmospheric elements, thereby inducing a change of index of refraction. Fourth, the complement material of the pair must create an optical interface with the first material in such a manner to suppress wavelengths significantly outside of the band of interest. Fifth, the various materials chosen must not mix at the boundary, which can introduce scattering losses caused by the rough interface.

There exist algorithmic searches for layer materials.²⁸ However, these searches base their merit function almost entirely on maximizing reflectivity at the wavelength of interest. Suppression of wavelengths outside this region and interdiffusion issues are not discussed. Genetic algorithms have recently been proposed,²⁹ however, which use departures from the desired spectra as their merit function.

The materials available as sputtering targets were as follows: Ag, Al, Au, Bi, C, Co, Cr, Cu, Fe, Ge, Li, Mg, Mo, Nb, Ni, Ru, Si, Sn, Ta, Ti, U, V, W, Al₂O₃, BaTiO₃, BN, B₄C, LaB₆, LiO₂, Si₃N₄, SiO₂, and TiO₂. Figures 11 through 18 plot the coefficient of absorption with respect to wavelength for all these materials. They are grouped by similar characteristic shapes.

Group I materials (Figure 11) represent the lowest coefficient of absorption in the wavelength range 25-35 nm. Satisfying condition two, these are the etalon materials of choice. Of these, rapid oxidation of lithium and magnesium leaves only silicon and aluminum as viable options.

The choice of the complement material must be made carefully. Even though molybdenum (second highest peak in group Vb, Figure 17) is a standard multilayer material, its optical constants are not suited for use in a Fabry-Perot filter,¹ as the

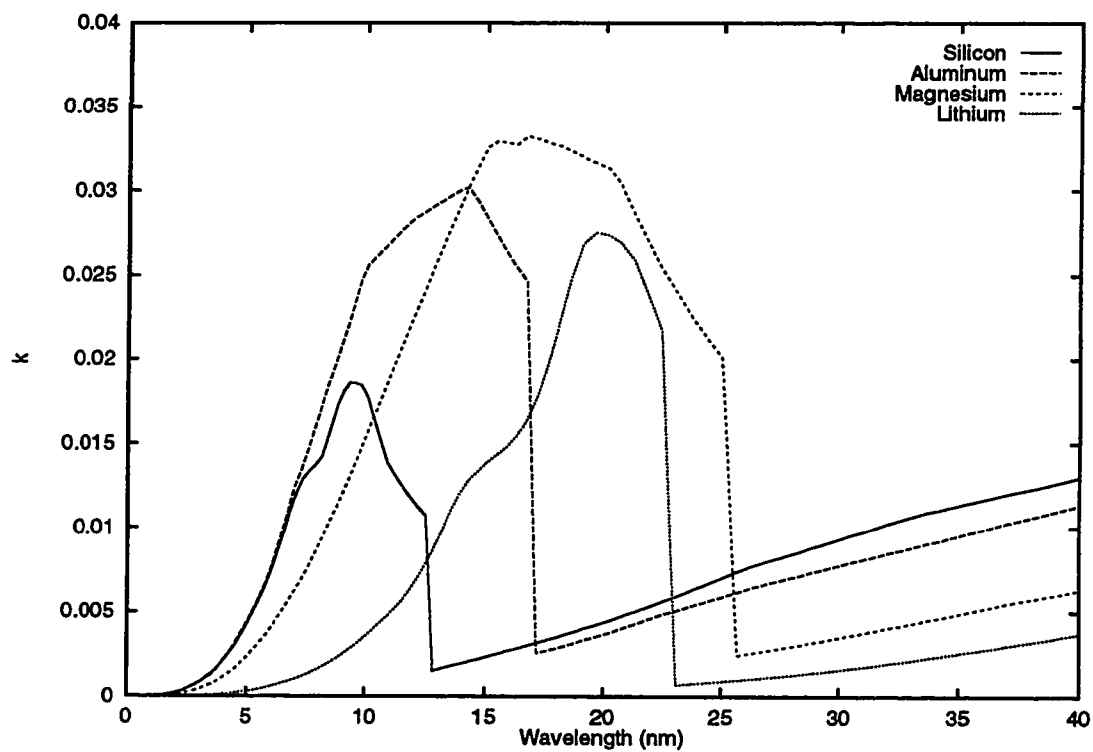


Figure 11. Coefficients of absorption: Group I.

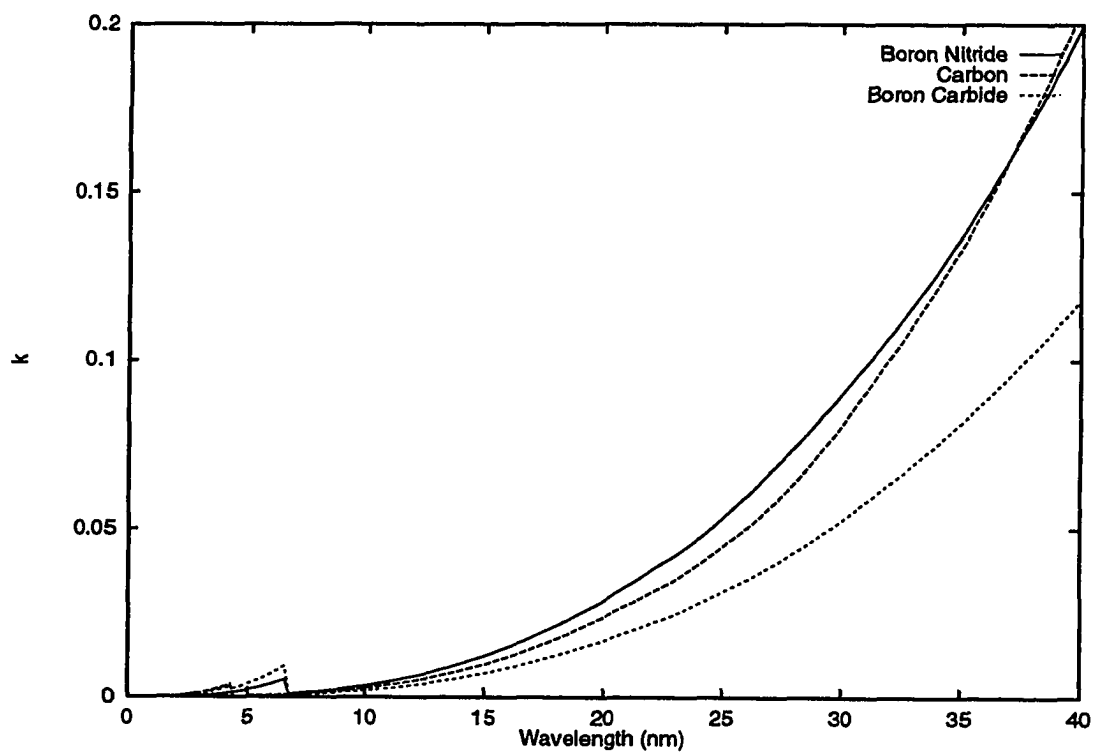


Figure 12. Coefficients of absorption: Group IIa.

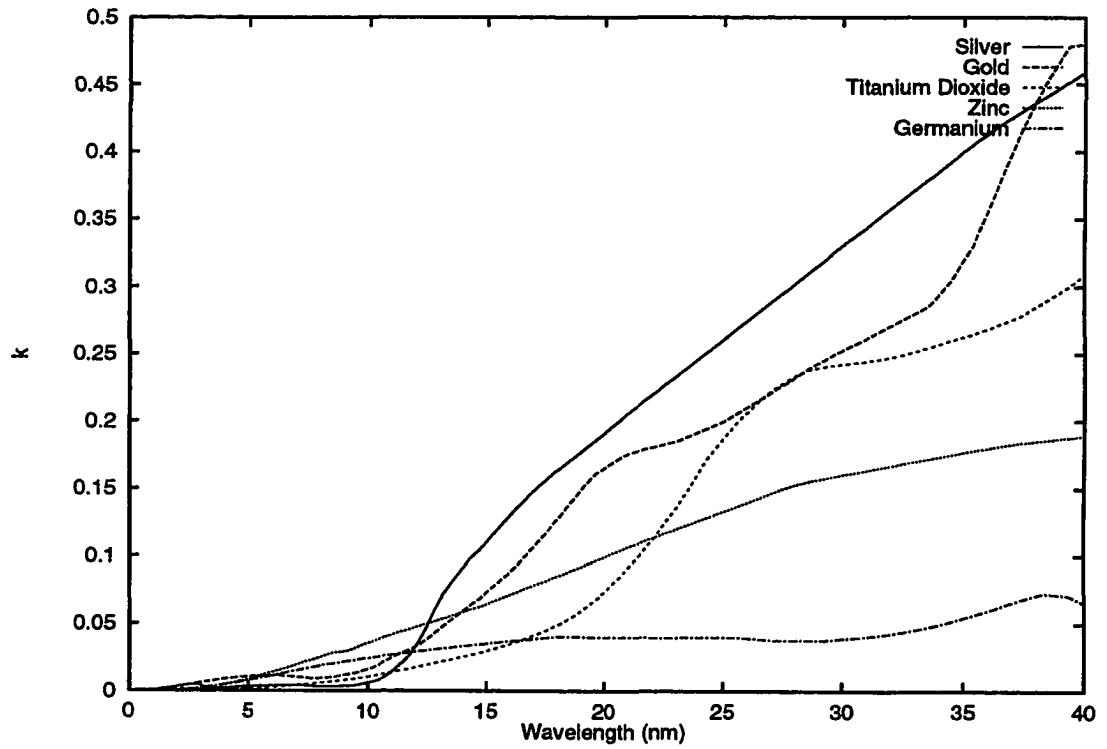


Figure 13. Coefficients of absorption: Group IIb.

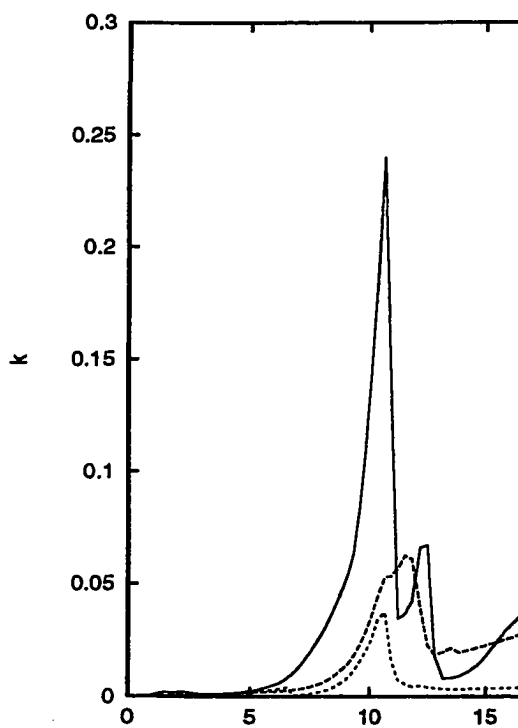


Figure 14. Coefficient

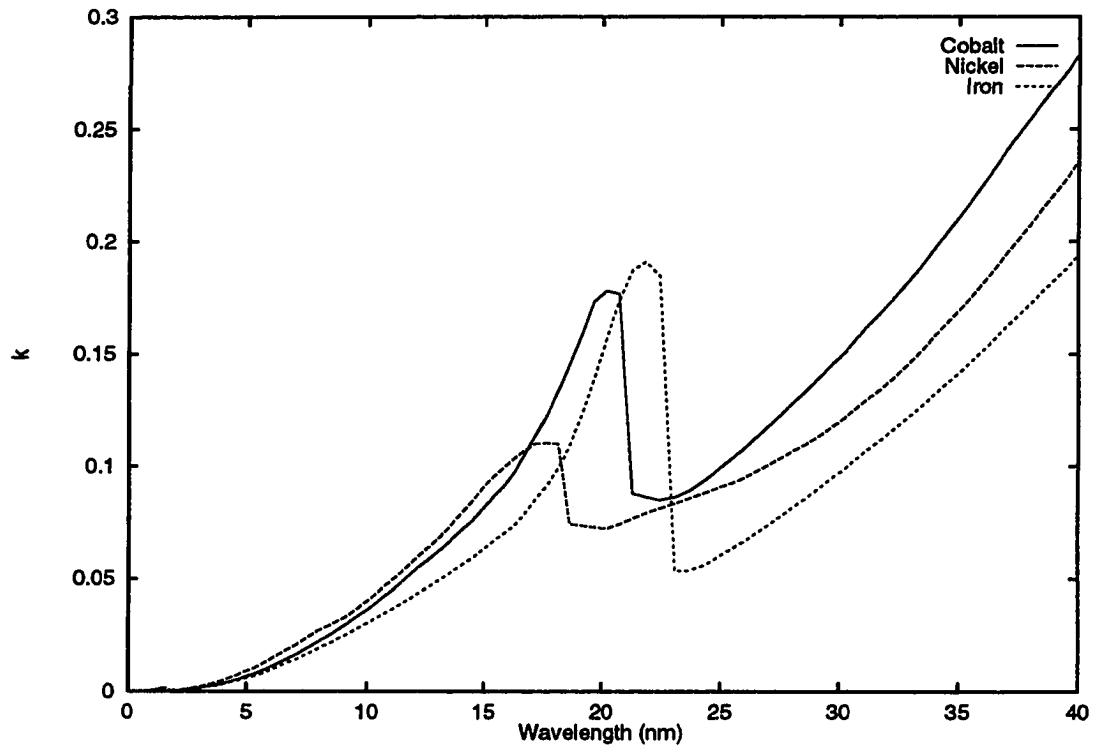


Figure 15. Coefficients of absorption: Group IV.

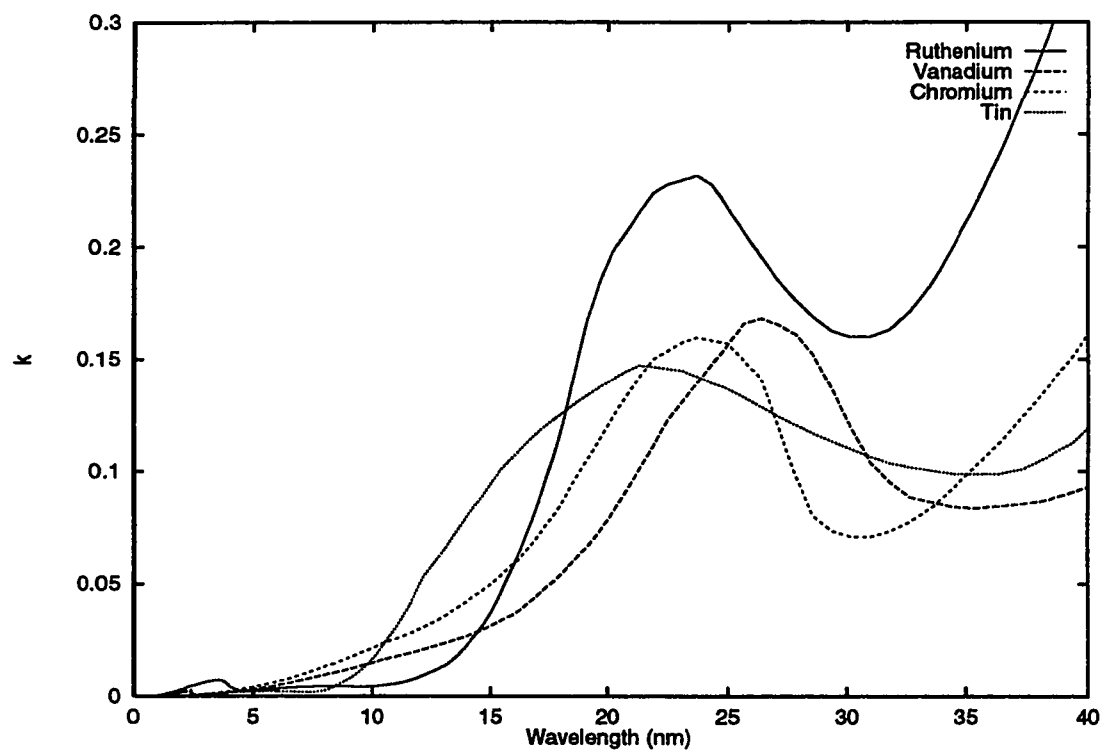


Figure 16. Coefficients of absorption: Group Va.

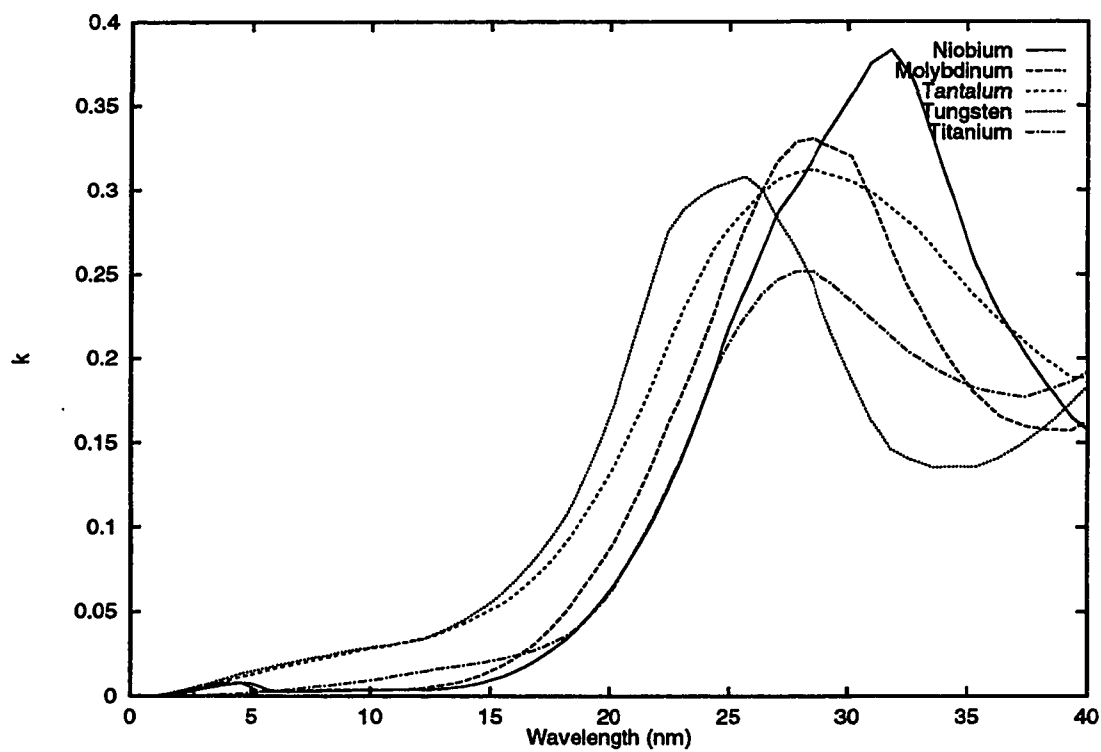


Figure 17. Coefficients of absorption: Group Vb.

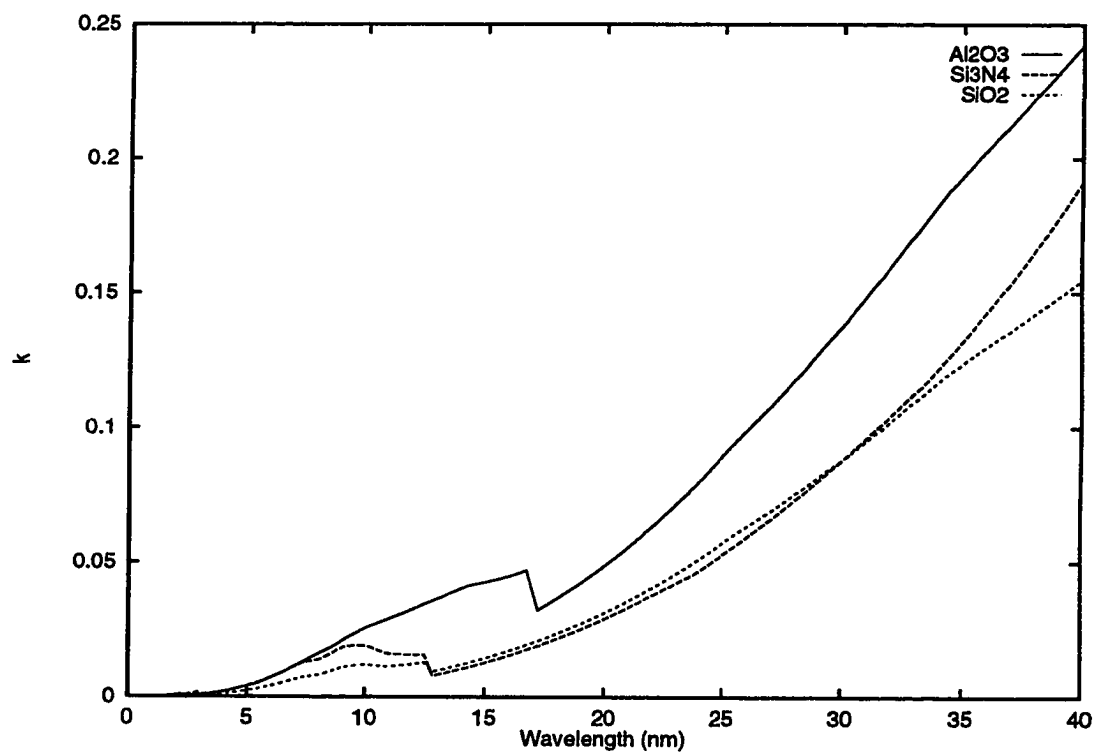


Figure 18. Coefficients of absorption: Group VI.

theoretical transmissivity plotted in Figure 19 depicts. This filter is a 27.5-nm thick silicon etalon between multilayer mirrors, each constructed of seven pairs of silicon and molybdenum layers. Each silicon/molybdenum layer pair has a thickness of 15.0 nm and a gamma of 0.2. The quick drop-off in index of absorption on both the high and low wavelength sides of molybdenum allows off-peak radiation to pass through the filter, causing the high "wings." Hence, materials from groups IV, Va, and Vb (Figures 15, 16, and 17) do not satisfy the fourth condition and are not useful. Materials from group IIa and VI (Figures 12 and 18) have coefficients of absorption that drop off too steeply on the short wavelength side.

Materials from group IIb (Figure 13) appeared to have the best chance of creating a filter with a narrow peak surrounded by areas of low transmission. Paired with possible materials from Group I, the first candidates were Zn/Al, Zn/Si, and Ag/Si. These candidates are plotted in Figure 20. Of these three candidates, the interdiffusion condition remains to be addressed. One means of doing so is to examine the phase diagram of the two materials such as are listed in Hansens' binary alloys tables³⁰ or Massalski's binary alloy phase diagrams.³¹

Carbon and tungsten are well known and often used multilayer materials. However, the diagram in Figure 21 shows a very complicated system indicating that, below 1250 C, the two materials may possess solid solubility with two phases present: a solid consisting of pure tungsten, and a solid containing tungsten carbide. Indeed, x-ray diffractometry revealed that a multilayer constructed of carbon and tungsten had characteristics that were far from ideal immediately following sputter deposition. The multilayer was designed to be a reproduction of the mirror created by Barbee

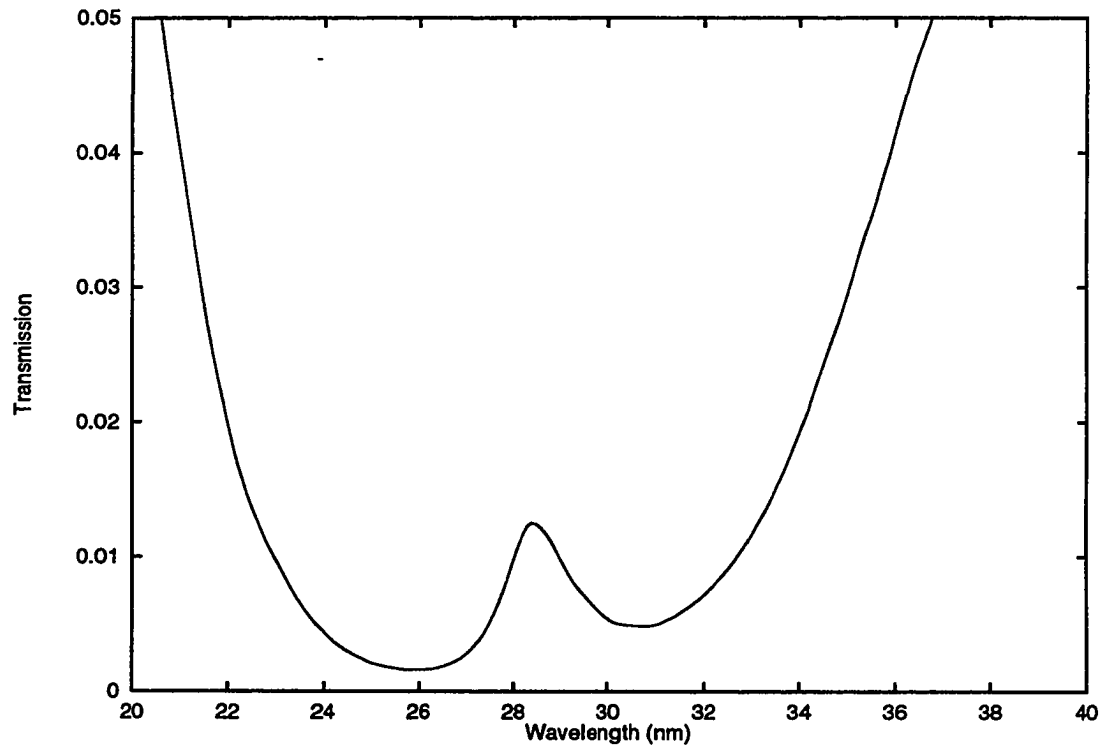


Figure 19. Molybdenum-silicon Fabry-Perot filter.

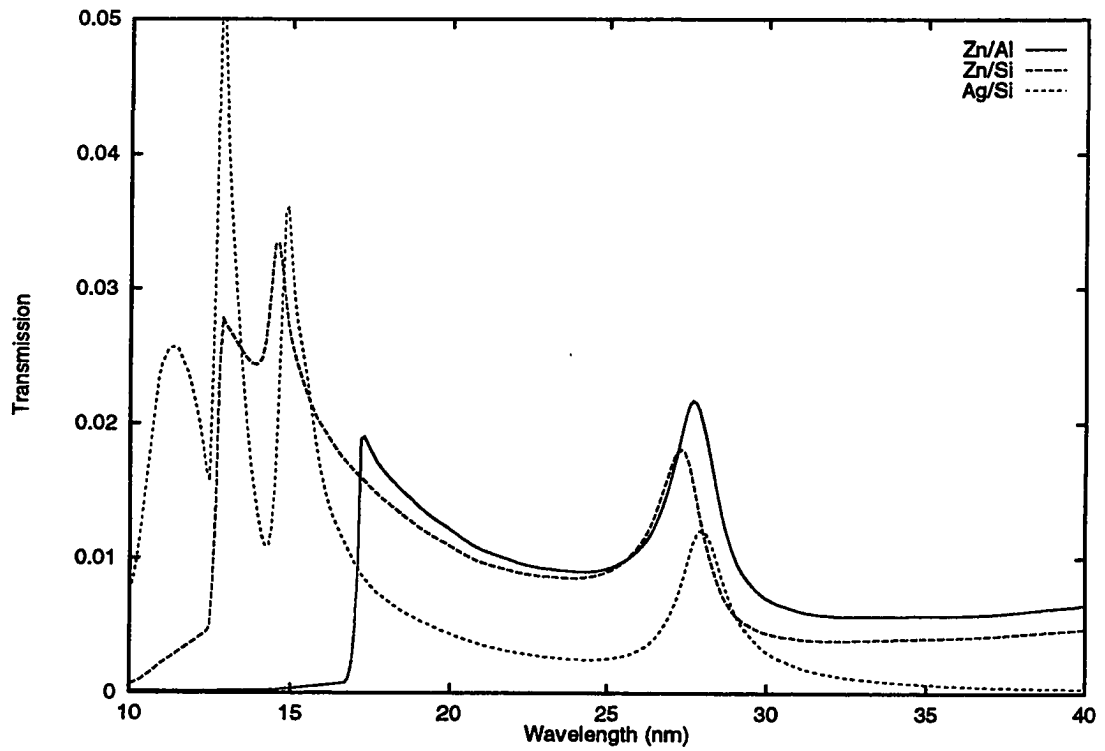


Figure 20. First candidates for Fabry-Perot filter.

*et al.*⁹ for their Fabry-Perot etalon: fifteen pairs of tungsten and carbon with a pair thickness of 2.76 nm and a gamma of 0.308. Figure 22 is the reflectivity of the sample two days after fabrication. Figure 23 is the reflectivity of the same multilayer after two years plotted against theory (solid line). The theoretical carbon-tungsten multilayer in the plot replaces the first tungsten layer with tungsten oxide (WO_2), and the interfacial roughness between layers is approximately 1.3 nm. Thus, both oxidation of the top layer and interfacial roughness induced serious degradation in the reflectivity of this multilayer.

Figure 24 is the binary alloy phase diagram for aluminum and zinc. Although solid solubility does not appear very great at temperatures below 50°C, the pairs silicon and zinc, and silicon and silver (plotted in Figures 25 and 26) appear to have a much lower solid solubility. Based on information from these diagrams, the decision was made to create the Fabry-Perot filter using silicon as the etalon and silver as the high-index complement.

The final parameters for this multilayer, listed in Table 6, were determined mostly via computational modeling. A pair thickness of 15.0 nm was used for initial modeling of the system and yields a peak reflectivity at 28.0 nm. Vinogradov's parameter (equation (29)) was plotted and a root found at $\gamma_{\text{opt}} \approx 0.190$. This requires the silver layer thickness to be 2.85 nm in each pair. This Fabry-Perot interferometer has a peak transmission of 1.55% at 20.04 nm with a full width at half maximum of 2.0 nm. Its transmissivity is plotted in Figure 27.

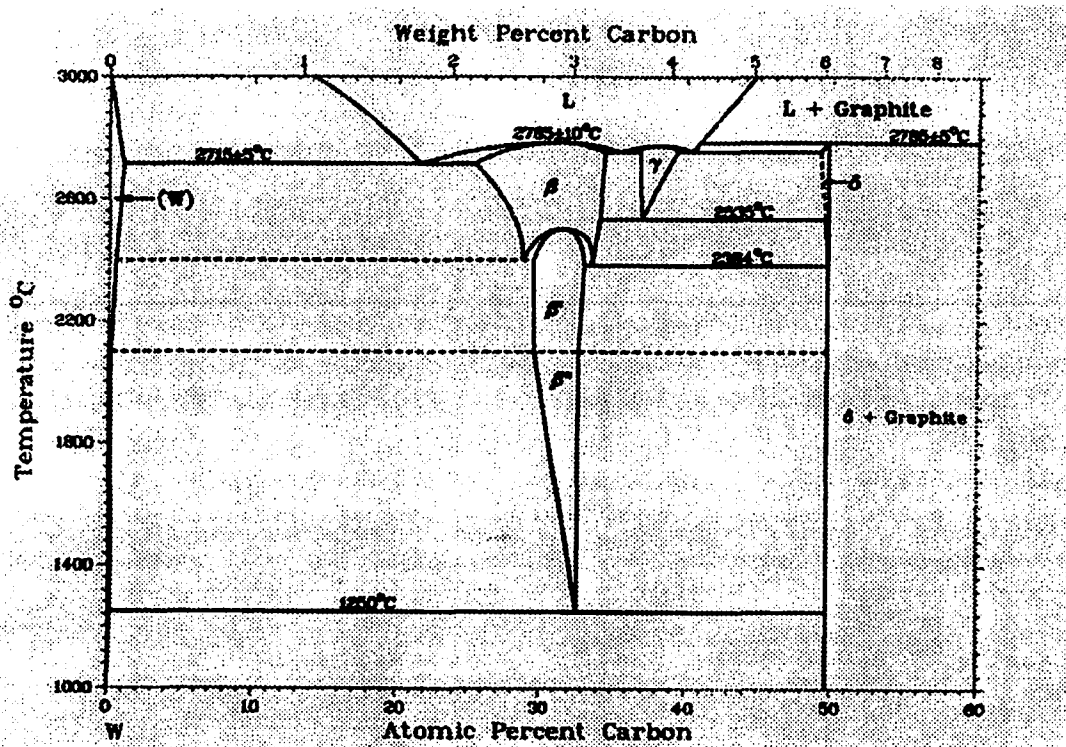


Figure 21. Binary alloy phase diagram for carbon and tungsten.

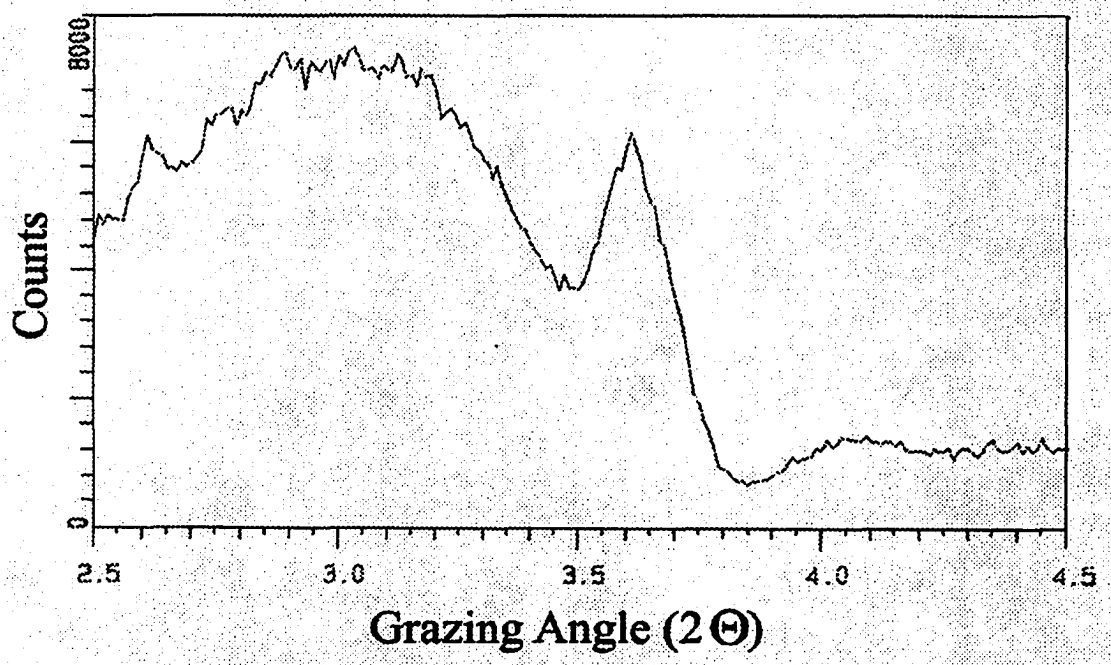


Figure 22. X-ray diffraction profile of carbon/tungsten multilayer.

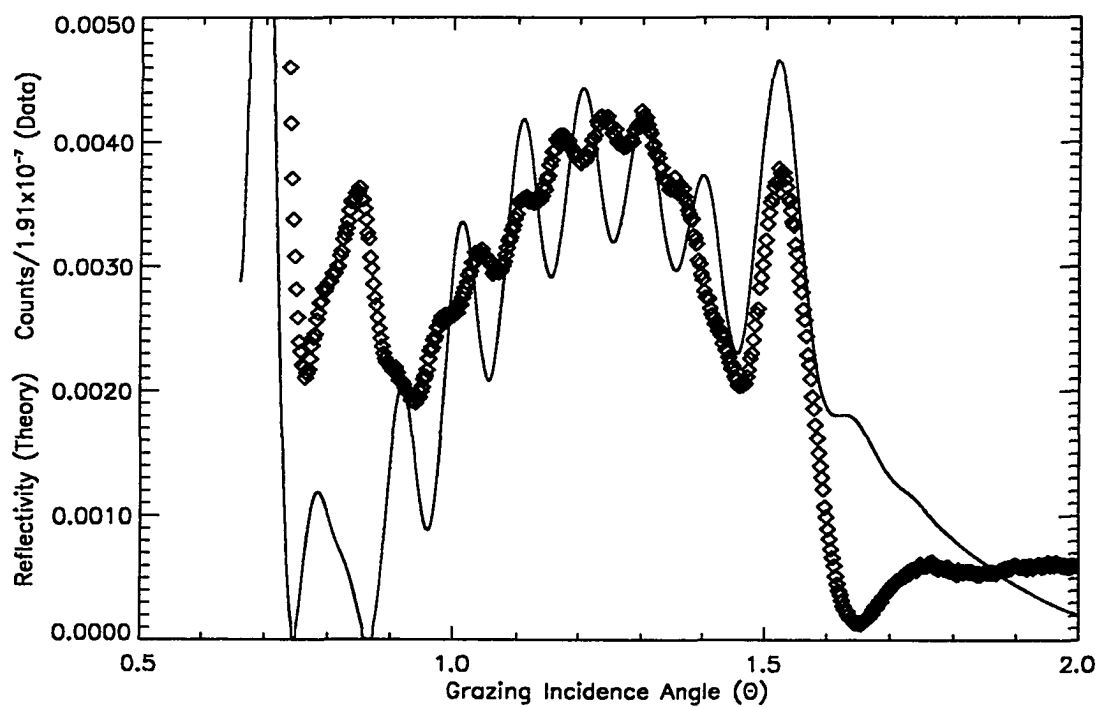


Figure 23. X-ray diffraction profile of carbon/tungsten multilayer after two years.

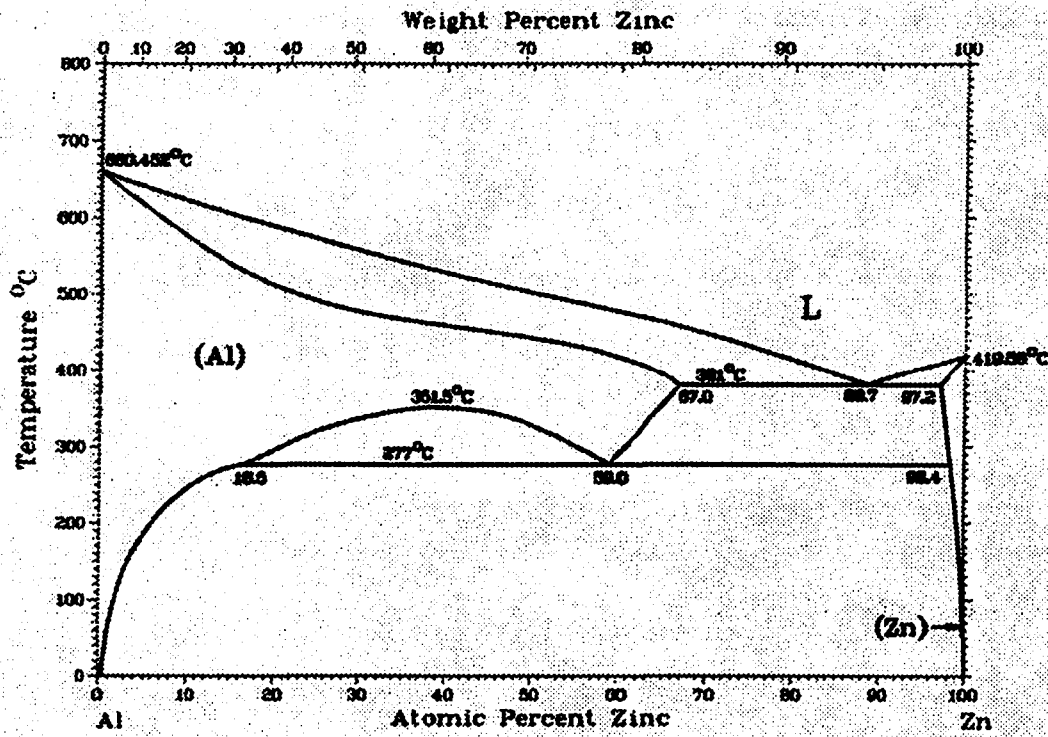


Figure 24. Binary alloy phase diagram for aluminum and zinc.

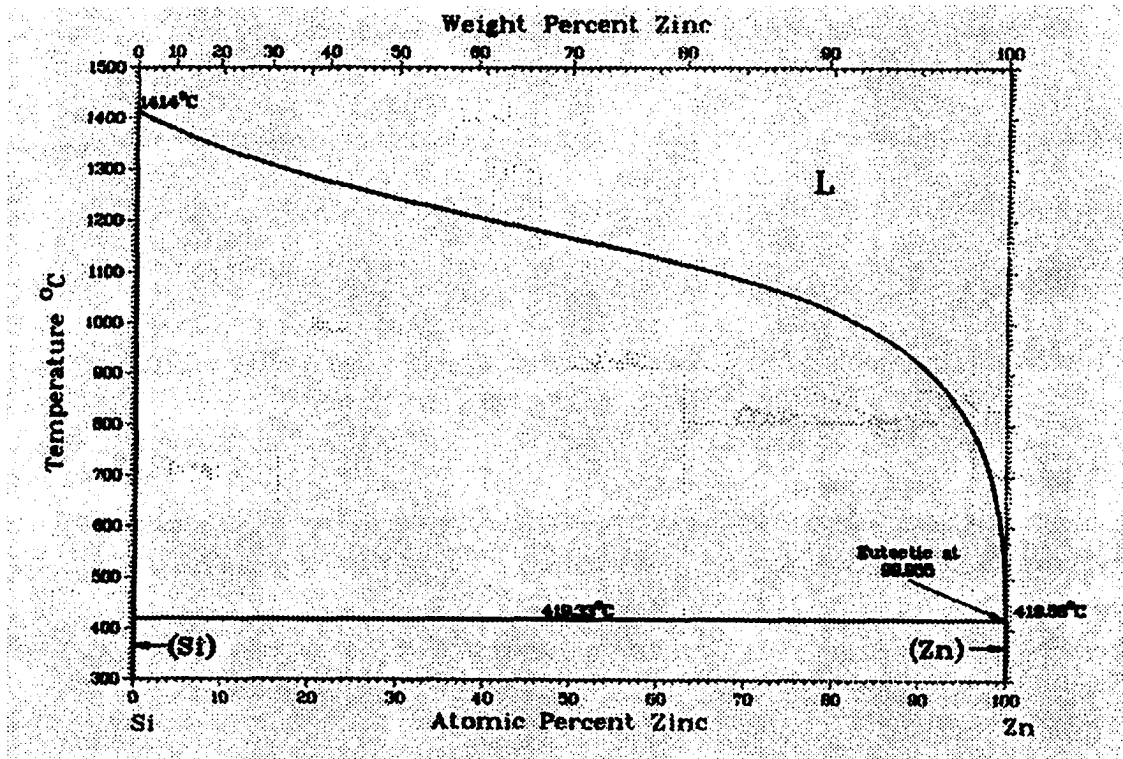


Figure 25. Binary alloy phase diagram for silicon and zinc.

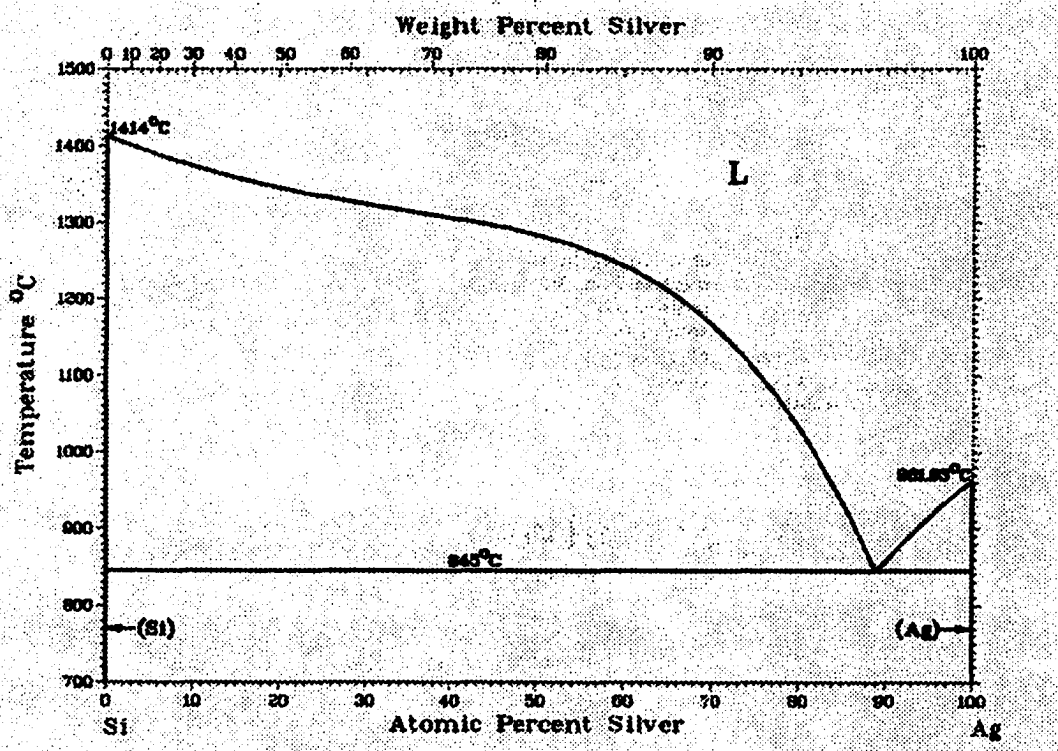


Figure 26. Binary alloy phase diagram for silver and silicon.

Table 6. Silicon/Silver Fabry-Perot design specifications.

	Layer	Thickness
7x	Silicon/Silver multilayer	12.15 nm/2.85 nm
1	Silicon etalon	26.0 nm
7x	Silver/Silicon multilayer	2.85 nm/12.15 nm
1	Silicon substrate	N/A

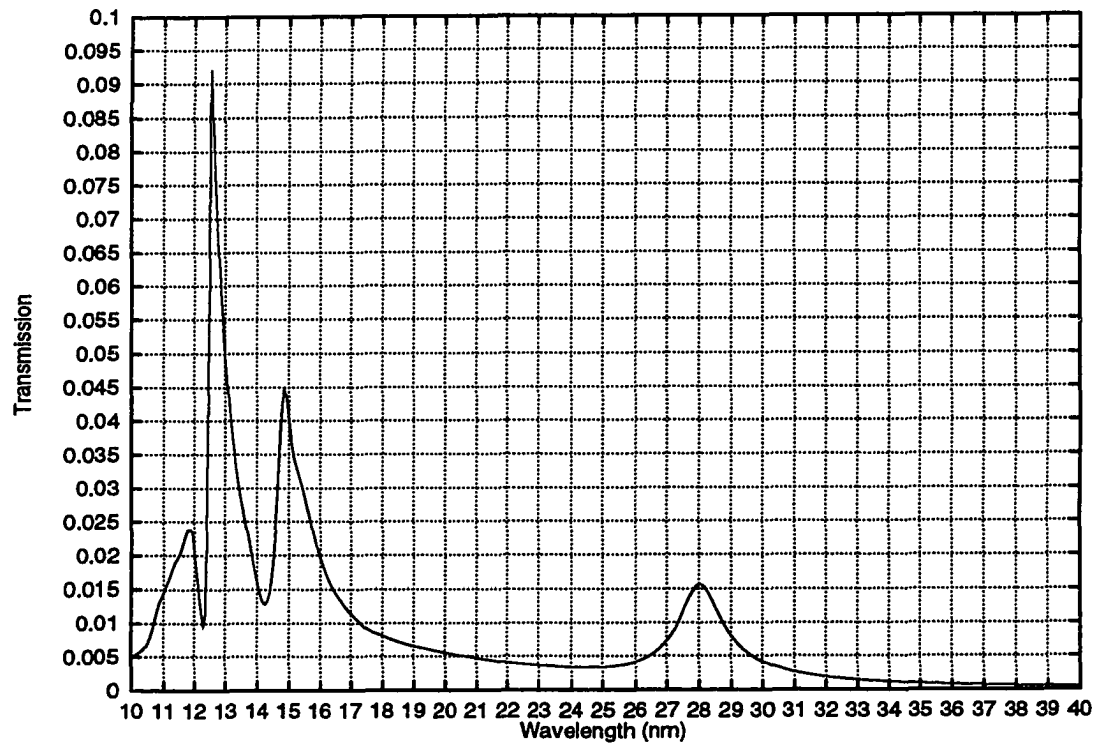


Figure 27. Fabry-Perot filter transmissivity as designed.

FABRICATION AND TESTING

Once the parameters for the desired Fabry-Perot interferometer have been determined, it is necessary to consider the methods by which it will be fabricated and tested. There are many different methods for depositing thin films. Sputter deposition, having deposition rates from 1–50 nm/min, is slow enough to be relatively well controlled. Because the filter is designed to be used in transmission, the substrate upon which the multilayer is deposited should ideally be transmissive.

After the filter has been constructed, it is necessary to determine the actual parameters of the fabricated optic. Contamination during deposition will affect the materials composition. Inaccuracies in determining sputter deposition rates will affect layer thicknesses. Finally, material properties may affect composition and sharpness of optical interfaces. To elucidate the final structure of the multilayer, Auger spectroscopy, x-ray diffractometry, transmission electron microscopy, and extreme ultraviolet reflectivity measurements were made.

Radio Frequency Triode Sputtering

Sputtering is the process by which atoms from a target are knocked off via collision by another species—typically ionized noble gases such as argon. Those atoms then drift toward and adhere to the substrate material. There are many configurations of sputtering devices, including D.C. diode, magnetron, and ion beam sputtering. The

system available at MSFC for fabricating multilayer structures involved R.F. triode sputtering. Figure 28 depicts the set-up at MSFC's Space Science Laboratory.¹⁵

A vacuum chamber is pumped down to $\approx 1 \times 10^{-6}$ torr. High purity argon is then introduced into the evacuated sputtering chamber to a pressure of 1×10^{-3} torr. A forward power of 200 watts at 13.56 MHz is applied while a small filament ejects free electrons into the chamber. These electrons, having high mobility, oscillate within the RF field and collide with the argon gas to produce argon anions with much lower mobility. During the production of the argon plasma, the water-cooled anode—upon which the substrate to be coated is placed—floats to a DC potential ≈ 1 KV higher than the cathode containing the target. These argon anions drift toward the cathode, dislodging atoms from the target upon collision.

Deposition rates can be determined by depositing a material onto a substrate (silicon wafer sections, in this case) and using a stylus profilometer to determine the thickness of a film deposited for a known time. It has been found that only the central 5 cm of the 15.2-cm target produces a fairly uniform deposition rate. The rates determined by this process are listed in Table 7.

Table 7. Sputter deposition rates determined by stylus profilometry.

Target	Sputter rate (nm/s)
Carbon	0.015 ± 0.002
Silicon	0.052 ± 0.006
Tungsten	0.155 ± 0.005
Silver	0.525 ± 0.041

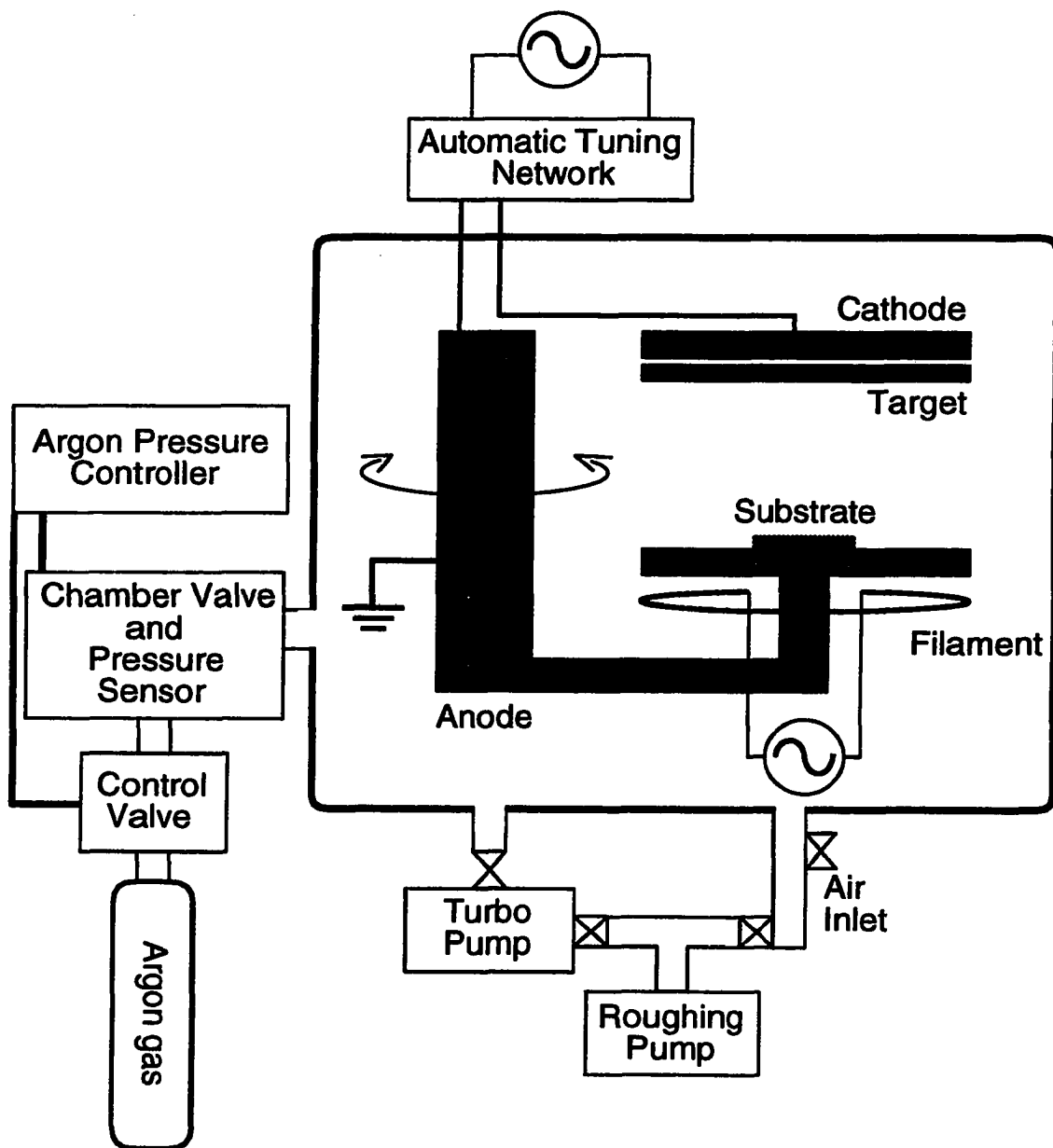


Figure 28. MSFC RF triode set-up.

One difficulty encountered with the system is that any sputter deposition performed must be of a duration that is an integer multiple of 1 s. Thus, deposited layer thickness must necessarily be slightly different from design thicknesses because of the inability to sputter for fractions of a second. The final sputter deposition rates given in the transmission electron microscopy section are 0.759 nm/s for silver and 0.126 nm/s for silicon. For the design specifications listed in Table 6, this requires a 3.75-s sputter for silver and a 96.43-s sputter for silicon. Because this is not possible, the deposition times were rounded to the nearest second. This yields the specifications given in Table 8 and $\gamma = 0.20$. Because the filter has a slightly larger period thickness, its peak transmission will be pushed forward slightly, to 28.2 nm. The filter is also not as thoroughly optimized, so the peak transmissivity will be slightly degraded: 1.23%. This degradation in performance is plotted in Figure 29.

Table 8. Silicon/Silver Fabry-Perot as deposited.

	Layer	Thickness
7x	Silicon/Silver multilayer	12.10 nm/3.04 nm
1	Silicon etalon	25.96 nm
7x	Silver/Silicon multilayer	3.04 nm/12.10 nm
1	Silicon substrate	N/A

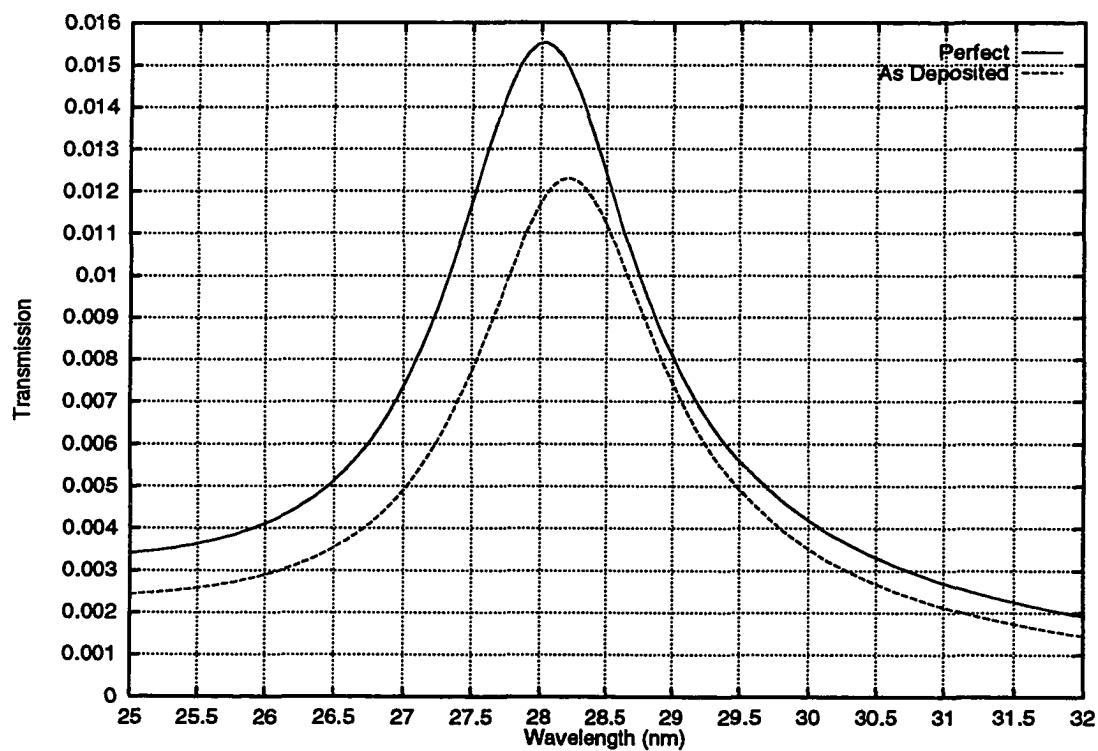


Figure 29. Fabry-Perot filter transmissivity as designed for deposition.

Substrate Preparation

Given the success of creating thin, silicon nitride windows as support structures for thin, multilayer optics,³² an attempt was made to produce 30-nm thick windows on a standard silicon wafer (diameter 76.2 mm; thickness 381 μm ; crystallographic orientation, $\langle 100 \rangle$; phosphorus doped; single-side polish). Because silicon nitride was available as a sputtering target, these layers were formed via sputter deposition.

If the windows are to be flat (indeed, if they are to exist at all), the silicon must be removed from beneath an existing silicon nitride layer. This is done by chemically etching the silicon in the desired locations from the reverse side. Crystalline silicon may be etched either isotropically or anisotropically. An isotropic etchant (such as hydrofluoric acid) removes silicon at equal rates in all directions. This chemical will continue to etch until it is either exhausted or chemically arrested. An anisotropic etchant (such as potassium hydroxide) removes silicon only from preferred crystallographic planes. When the required symmetry no longer exists, the etching process halts.

Given the autonomous nature of these anisotropic etchants, and the ability to form square windows, it was decided to use potassium hydroxide as the etchant. No special handling is required because silicon nitride is not attacked by potassium hydroxide. To limit the activity of the etchant to only the spots where the windows were to be placed, a coating of silicon nitride needed to be placed over the back side of the silicon wafer with the proper holes. This was done via photolithography techniques performed at the U.S. Army Weapons Directorate.

Because potassium hydroxide creates a pyramidal pit with an apex angle of 54.7° , the final window size will be 0.54 mm smaller than the window created on the reverse side after etching through the 381- μm thick wafer. A mask with properly sized windows was designed in a computer CAD program. The mask chosen had approximately 315 rectangular holes with dimensions of one side ranging from 0.6 mm to 4.4 mm. This design was then imaged onto a photographic plate. The plate was developed, washed, and used as the photolithographic mask.

After the silicon nitride layer was sputter deposited on the polished surface of the wafer, the reverse was coated with Shipley STR1045 photoresist and the wafer was spun at 3500 rpm for 60 s to thin the photoresist to an even coating of 5 μm . The coating was hardened by heating the wafer to 110°C for 2 min. The photoresist, being relatively insensitive to visible light, was then vacuum sealed to the emulsion side of the mask and exposed to ultraviolet light. The mask was then removed from the wafer and the photoresist was developed in sodium metasilicate and washed, leaving photoresist squares in the places where windows were desired. The reverse surface was then coated with 100 nm of silicon nitride.

Because parts of the silicon nitride are supported by the photoresist, it was removed when the photoresist is removed with acetone. This is called a "lift-off" procedure. Following the removal of silicon nitride from the etch regions, the wafer was immersed in potassium hydroxide to begin the etching process. Unfortunately, during the 6-h etch, the potassium hydroxide was able to undercut the silicon nitride mask and begin etching in unwanted areas. It is highly possible that the rough surface of the reverse side of a singly polished silicon wafer kept the silicon nitride mask from

bonding well to the silicon. A doubly polished wafer may very well have provided a substrate capable of surviving the etching procedure. As a result of not being able to constrain the etching procedure before the assigned SSRL beam-line time, it was decided to abandon this process and test the optic only in reflectivity.

Structure Testing

Once the filter is fabricated, there are a number of ways to determine the resulting structure. The quantities of the greatest importance are layer periodicity and thickness, interface quality, and composition. The four methods used to elucidate these quantities were Auger spectroscopy, x-ray diffractometry, transmission electron microscopy, and reflectometry at extreme ultraviolet wavelengths.

The composition of the multilayer certainly will have an effect on its performance. Because the optical constants are more affected by elemental content than anything else at these wavelengths, it is important to determine the presence of impurities. Auger spectroscopy was utilized to determine materials composition because it is relatively straight forward and capable of detecting small amounts of elements heavier than lithium.

Of the four methods utilized in testing the fabricated multilayer structures, x-ray diffractometry was the least time consuming. Because optical constants rapidly approach unity as wavelengths decrease, the reflectivity of $\text{Cu-}K_{\alpha}$ radiation at 0.154 nm off a sample may be modeled by the approximation given in equation (8). This simplifies analysis of pair thicknesses greatly and was used frequently to determine sputter deposition rates. Because the wavelength is so short, it is also greatly affected

by interfacial roughness and can be used to monitor this quantity as well. This method is also non-destructive; thus, it is possible to re-test a sample at a later time to observe time dependent effects such as interdiffusion.

X-ray diffractometry alone is not enough to determine the ratio, γ , because it can determine only the pair thickness. To actually measure layers nanometers thick, a cross section of the multilayers was made and subjected to transmission electron microscopy. High energy electrons (20-200 keV) possess a DeBroglie wavelength of 8.6-2.5 pm—smaller than visible light photon wavelengths by roughly a factor of 100,000. This allows one to visually inspect structures many orders of magnitude smaller than is possible via visible light microscopy. To study layers nanometers thick, this becomes a necessity.

Finally, a test of reflectivity at the wavelength of interest must be performed. Whereas x-ray diffractometry is not sensitive to oxidized layers or adsorbed moisture, extreme ultraviolet reflectivity is. This information can be checked with data retrieved from Auger spectroscopy. The reduction in reflectivity resulting from interfacial roughness can be double checked against that inferred from x-ray diffractometry.

Auger Spectroscopy

It is desirable to determine the species of atom present in the fabricated multilayer. Even though the sputtering process will create a multilayer with a given materials content, such things as the purity of the sputtering targets, presence of a leak in the vacuum system, and pressure of sputtering ion species may affect the actual material content. Auger spectroscopy was utilized to detect impurities.

Auger spectroscopy involves the collection of emitted electrons from the sample and the measurement of their respective kinetic energies. This requires a fairly high vacuum and was performed at 3.6×10^{-8} Pa at the University of Alabama at Birmingham's Materials and Mechanical Engineering department. To eject these electrons, electrons of an energy high enough to ionize inner shell electrons (10 keV at 300 nA in this case) is sent toward the sample. An incident electron creates a hole in the K shell of an unknown atom in the sample. An electron in the L shell of that atom drops into the K shell and fills the hole. The surplus energy either is emitted as a photon or ejects an electron in a higher shell. The process which ejects the electron is the one of interest. The energy with which the electron leaves is characteristic of the species of atom from which it came. This is the Auger electron. What remains is an atom doubly ionized in the L shell.

Figure 30 is a surface scan of Sample 25—fifteen pairs of silver on silicon. The horizontal axis represents the energy of electrons collected. The vertical axis is the derivative of the number of electrons collected at a given energy. Plotting the derivative shows sharper features and is easier to interpret.

The Auger process is non-destructive. However, to determine impurities incorporated into the multilayer, a destructive mode is available. First, a surface scan is taken, then the sample is bombarded with argon ions in a low grade vacuum (7×10^{-3} Pa) to remove some sample. Another scan is taken in the pit created by the argon ion beam.

Figures 31 and 32 show scans taken after 120 and 300 s of bombardment have taken place. Although one would expect to see only silver or only silicon, this

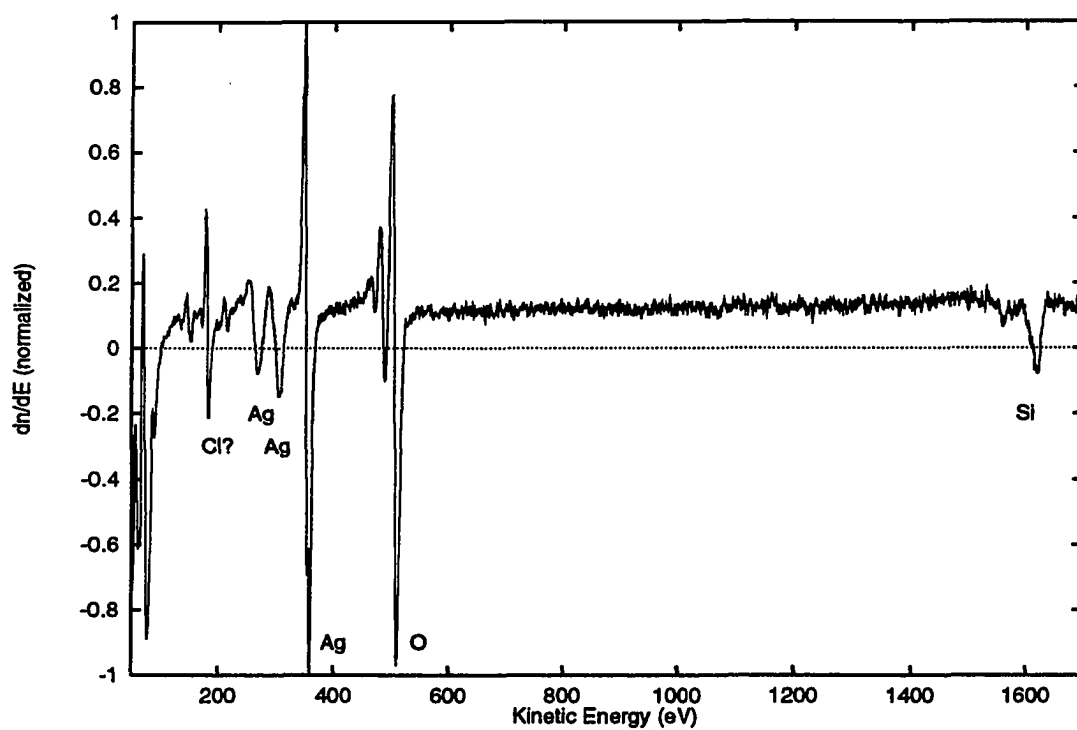


Figure 30. Auger surface scan of Sample 25.

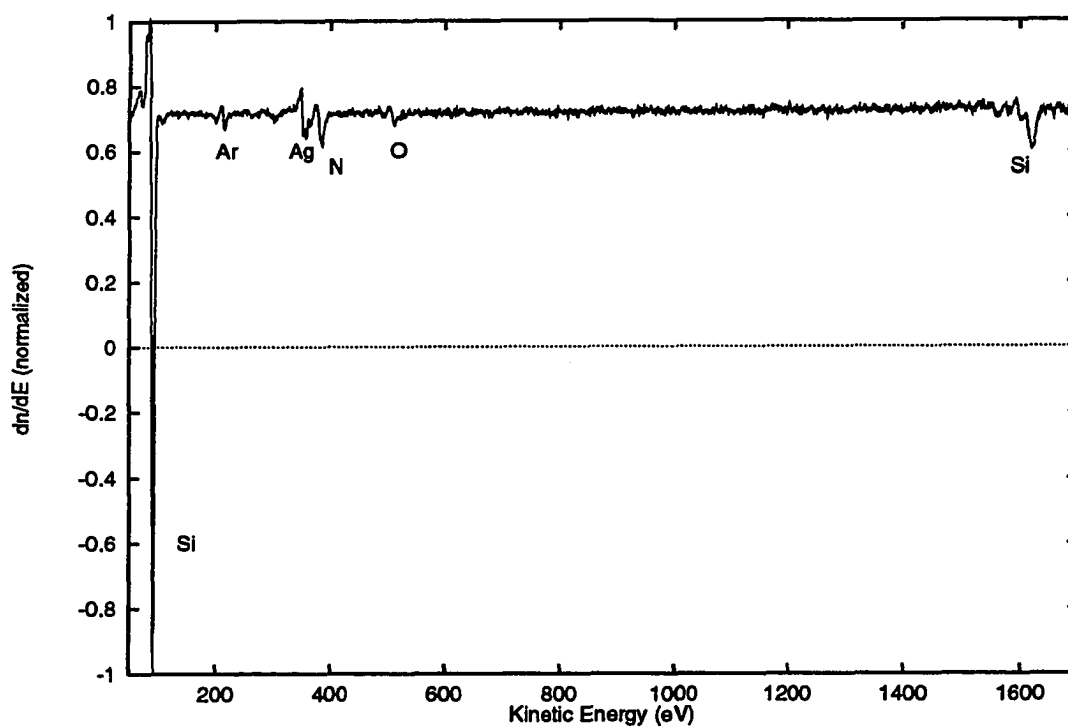


Figure 31. Auger scan of Sample 25 (120 s sputter).

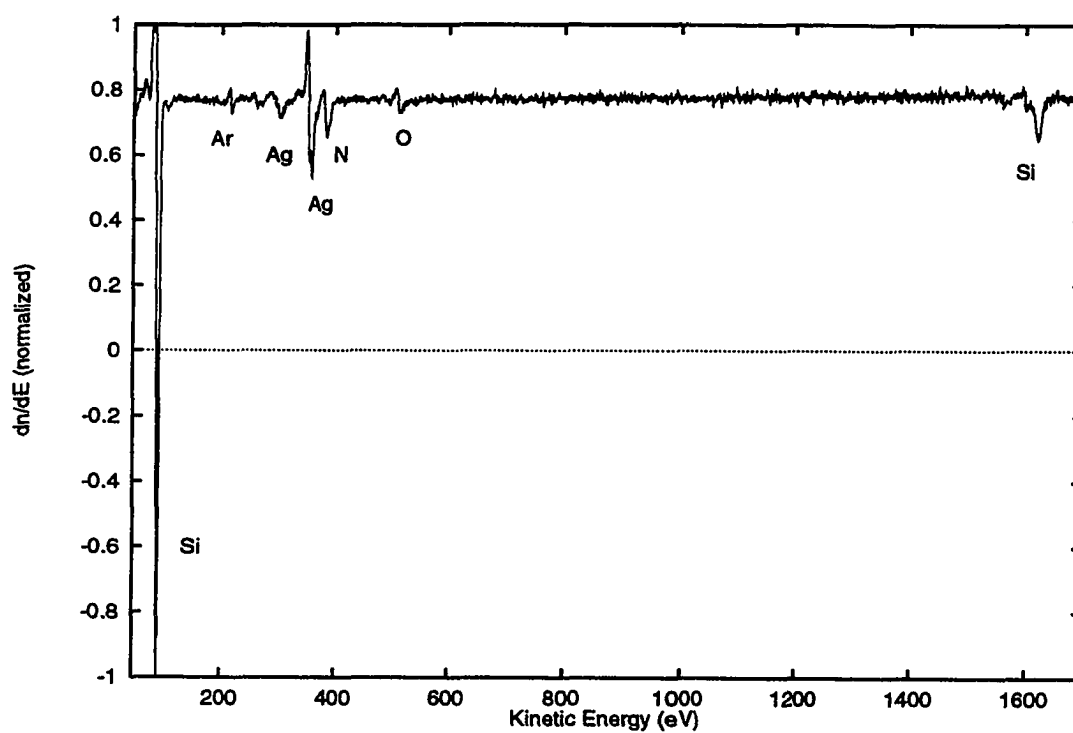


Figure 32. Auger scan of Sample 25 (300 s sputter).

particular data set was collected while the region of interest was set larger than the argon ion beam width. Hence, more than one layer was scanned. This was corrected during the depth scans.

These scans show no serious impurities incorporated in the multilayer structure. Silicon and silver are certainly expected. Argon is a residual signal from sputter ablation of the sample because it is absent from the surface scan. Except for the surface scan, the oxygen and nitrogen signals occur due to a leak in the vacuum system. At the surface, the very prominent oxygen signal is due to oxidation of the silver surface. This is better determined from the depth scans to follow.

Figure 33 is a micrograph of the region tested. Note the alternating bands of light and dark surrounding the pit. These are cross sections of the silver (light) and silicon (dark) layers as the pit was created.

During an automated depth scan, the spectrometer records relative numbers of electrons in a number of energy "windows," performs a timed sputter removal of sample, and then records electrons captured at the new depth. Figures 34 and 35 show the relative numbers of electrons collected in four energy windows, shown in Tables 9 and 10, as a function of sputter time. Each sputter cycle lasted 3 s. X-ray diffractometry measurements place pair thicknesses in this sample near 21 nm. This yields an ion removal rate of approximately 0.4 nm/s.

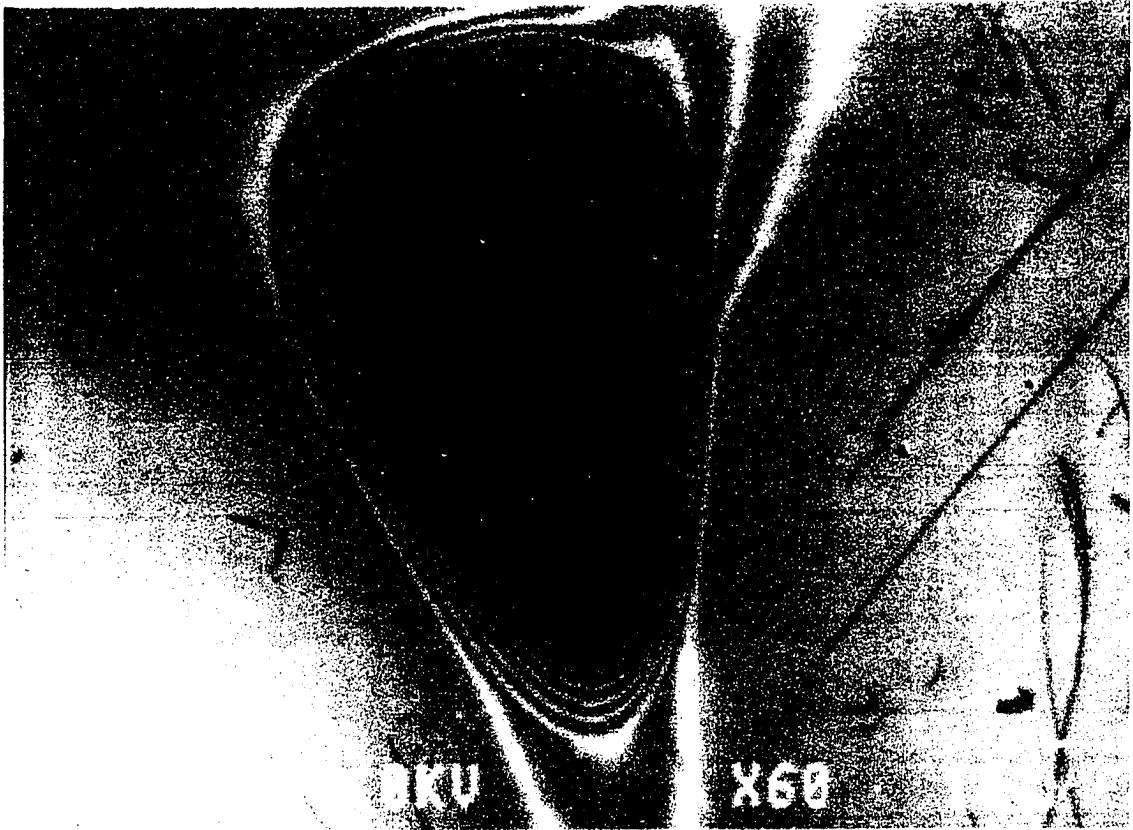


Figure 33. Scan of Sample 25.

Table 9. Energy windows for Figure 34.

Element	Energy range (eV)
Silver	341-366
Nitrogen	371-396
Oxygen	500-525
Silicon	1602-1634

Table 10. Energy windows for Figure 35.

Element	Energy range (eV)
Silicon	82-100
Silver	341-366
Nitrogen	371-396
Oxygen	495-520

Given a periodic structure of silver and silicon, one would expect to see the silver and silicon signals oscillate 180° out of phase. This is not seen in Figure 34 because the sensitivity of the spectrometer at 1620 eV seems to be too low. When the lower energy silicon line was chosen, the desired periodicity emerges as shown in Figure 35. The wild features in the silicon signal in peaks 10 and 11 are noise related and not data.

Structures of note in the depth scan include a constant nitrogen and oxygen signal. It would appear that a small leak had developed in the system. Note the correlation between the two signals, especially just after sputter cycle 160 and just before cycle 180. However, two oxygen structures make themselves apparent: at the surface of the multilayer, where oxidation has taken place; and at the substrate, where oxidation took place before the multilayer was deposited.

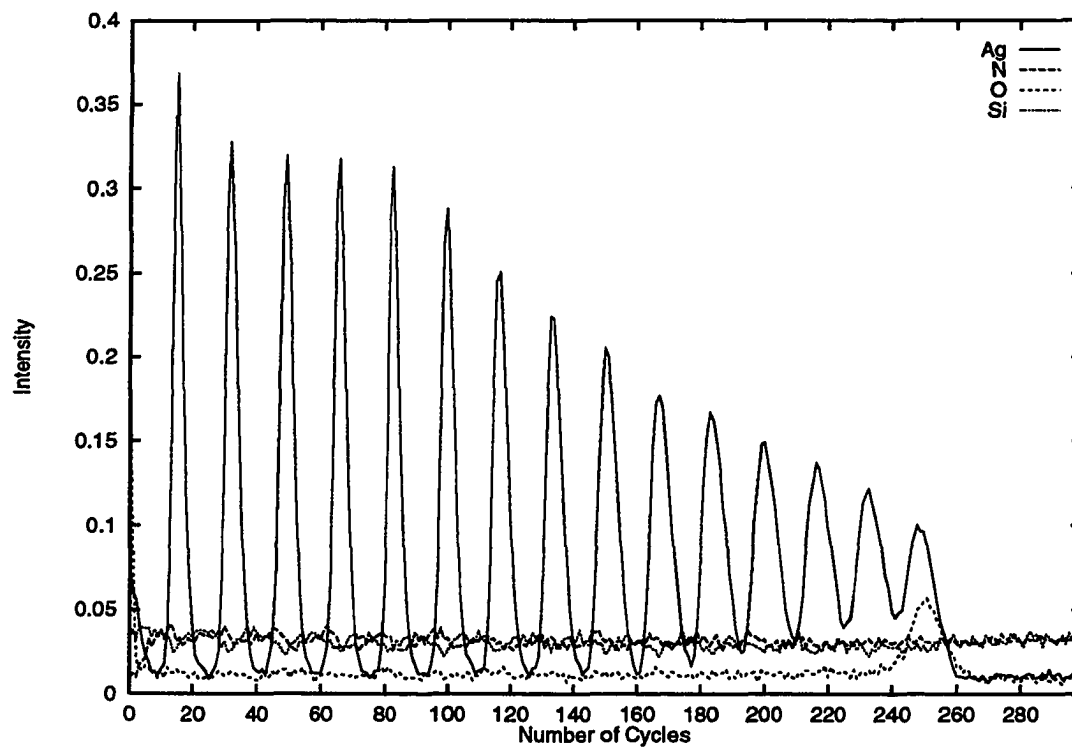


Figure 34. Depth scan of Sample 25 using high energy Si line.

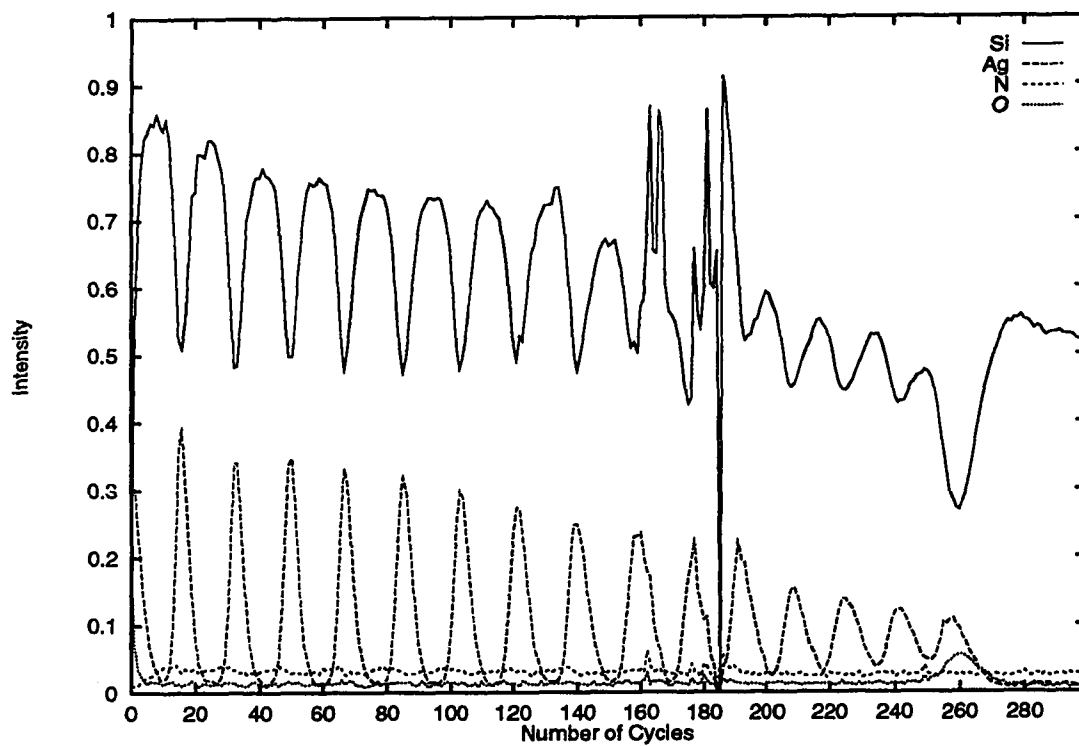


Figure 35. Depth scan of Sample 25 using low energy Si line.

Although the Auger spectroscopy depth scans imply a proper, alternating structure of relatively pure silicon and silver, it does not do so with much accuracy. Because sputter removal rates differ between silicon and silver, the actual thickness of the layers is unknown. The question of interfacial roughness is also left unaddressed. X-ray diffractometry, transmission electron microscopy, and extreme ultraviolet reflectivity are better suited for such inquiries.

X-ray Diffractometry

X-ray diffractometry consists of shining a narrow beam of x-rays from a Cu- K_α source onto the sample to be tested. The specularly reflected beam impinges on a cesium iodide crystal, and the intensity is measured in counts. Because the wavelength is so short, one can model the multilayer as a crystal and use Bragg relation

$$N\lambda = 2D \sin \Theta \quad (57)$$

where N is the order of the reflection, λ the vacuum wavelength of the incident radiation, D the pair thickness and Θ the grazing angle of incidence ($\Theta = 90$ is normal incidence). A plot of reflectivity versus grazing incidence angle shows peaks at integer N values and may be used to determine D .

During fabrication of the Fabry-Perot filter, many samples were created and tested via x-ray diffractometry to determine multilayer pair thicknesses. Two such plots are shown in Figures 36 and 37. The sample in each case is fifteen pairs of silicon and silver. In conjunction with transmission electron microscopy, sputter de-

position rates may be determined much more accurately than measurement via stylus profilometry of a single coating deposited upon a substrate.

According to Spiller,³³ interfacial roughness and thickness errors will strongly affect the x-ray reflectivity of an imperfect multilayer. This can be seen in Figure 37 as a result of the reduction of layer thicknesses by 67%. It is better seen, however, in the rocking curve of the fabricated Fabry-Perot filter in Figure 38. Three parameters must be changed to better fit the model to the data: pair thickness, thickness error, and interfacial roughness.

Easiest of the three parameters is the pair thickness, D . The model is based on a perfect reproduction of the desired optic—a pair thickness of 15 nm. The spacing between peaks in the data, however, is best modeled by a pair thickness of 14.25 nm.

Thickness errors produce two effects: they reduce reflectivity in the main peaks and increase reflectivity between peaks. Both of these effects are easily seen in the figure. Computational modeling suggests a thickness error of approximately 0.5 nm.

Interfacial roughness also reduces the reflectivity in the peaks but also causes the reflectivity to drop more steeply at larger grazing angles. The data imply an interfacial roughness of approximately 0.5 nm. Fernandez *et al.*¹⁰ measured the interfacial roughness of their molybdenum/silicon optic via x-ray diffractometry and reported a value of 0.6 nm. Figure 39 shows the data plotted against a model incorporating these three effects. This model also includes an adsorbed water layer 7.0 nm thick, a fully oxidized top silicon layer (SiO_2), and an eighth silver layer added between the substrate and the multilayer. X-ray reflectivity is relatively insensitive to the first two effects; however, motivation for their inclusion is presented with the EUV reflectivity

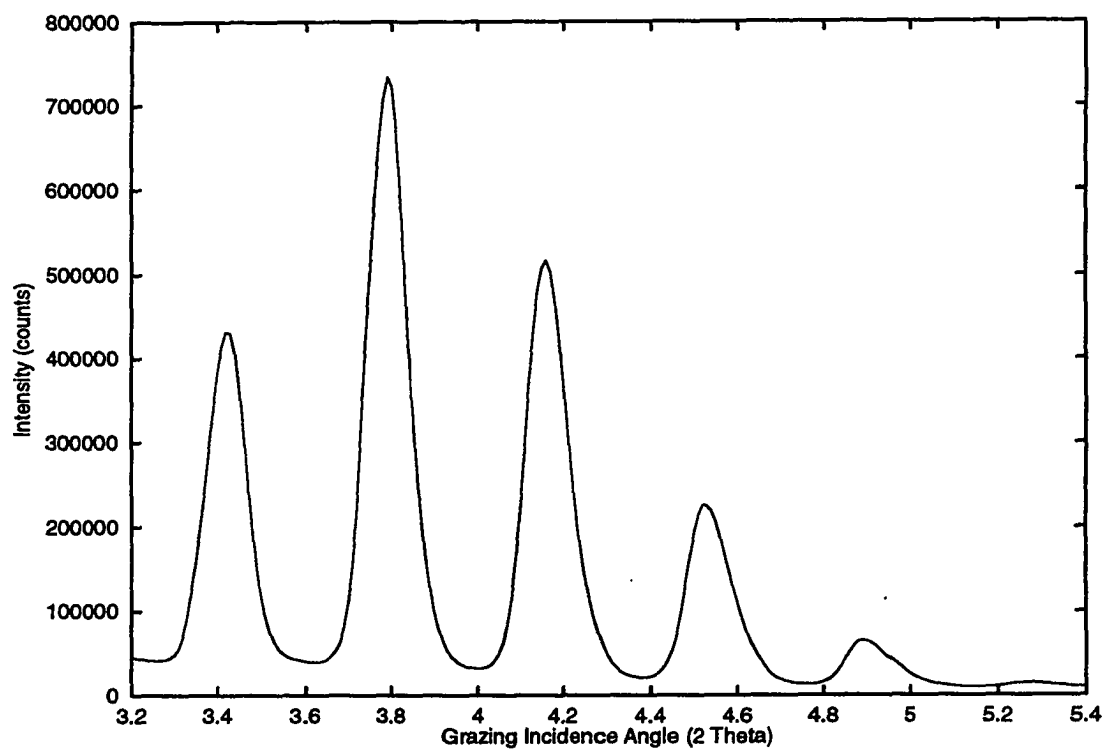


Figure 36. X-ray diffractometry profile of Sample 20: 23.88 nm/pair.

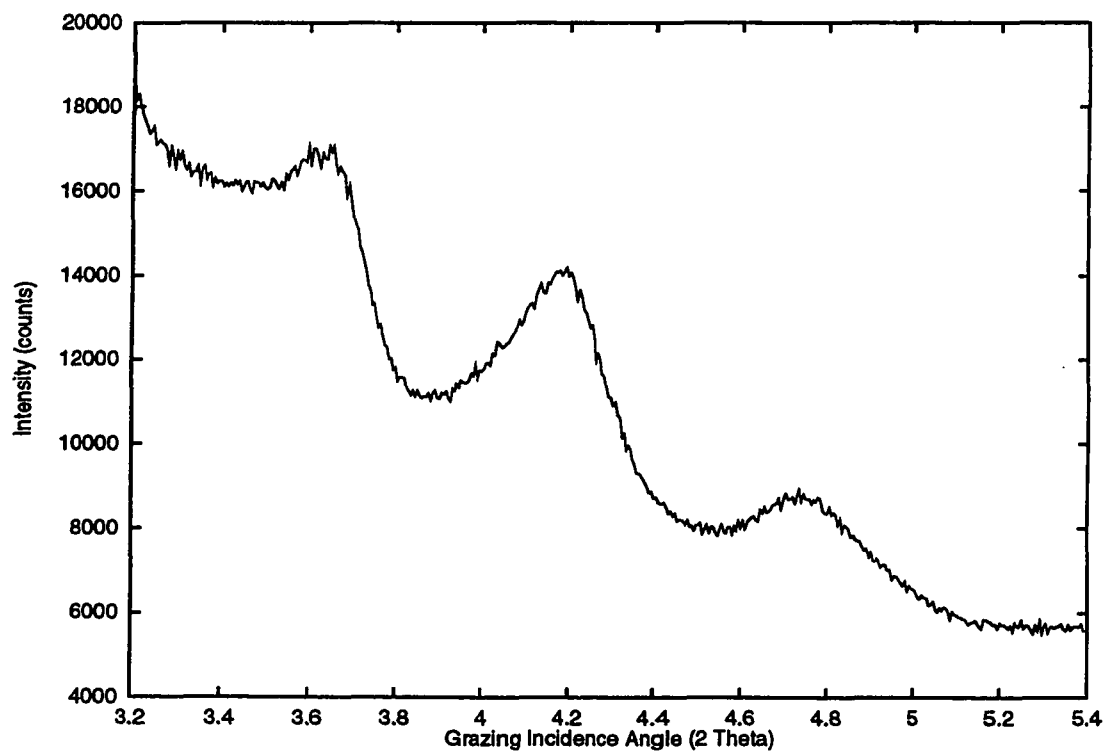


Figure 37. X-ray diffractometry profile of Sample 28: 16.1 nm/pair.

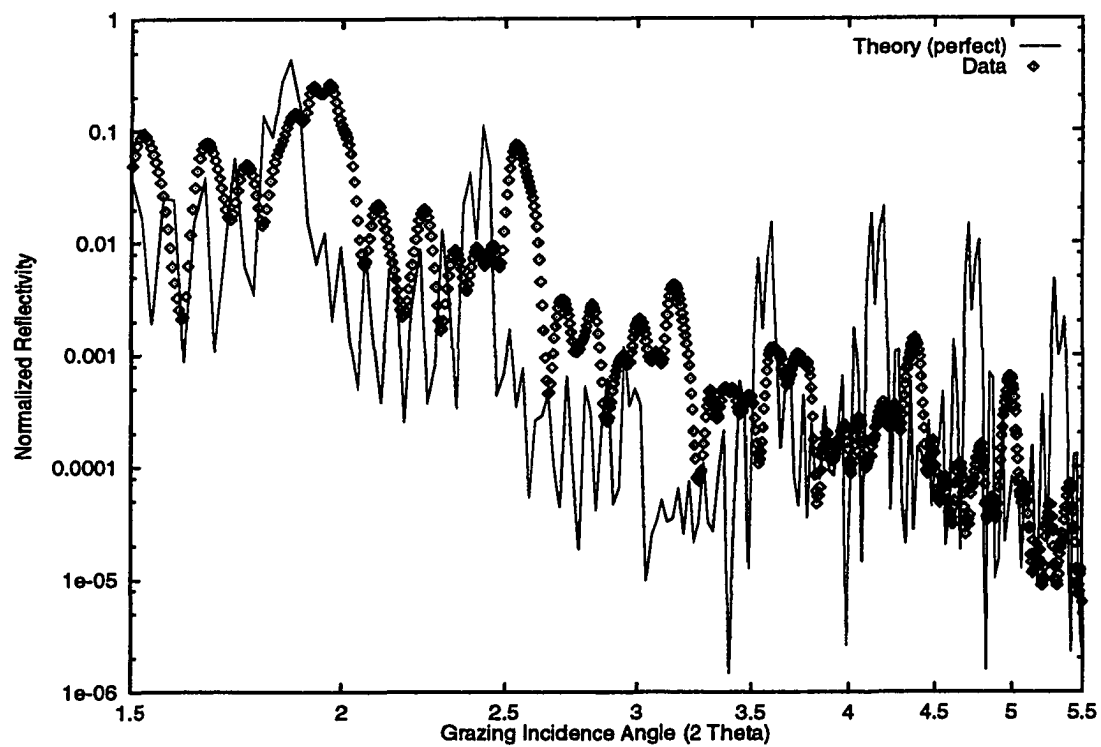


Figure 38. X-ray diffractometry profile of Fabry-Perot filter.

data below. Inclusion of an additional silver layer is done on evidence provided in the transmission electron microscopy section.

Transmission Electron Microscopy

Electrons are easily scattered within materials. Therefore, transmission electron microscopy samples must be extremely thin before information can be gathered. Preparation of the sample requires approximately one week, and although this test can yield useful results, it is very time intensive.

The process for creating the sample requires sawing the sample in half with a diamond saw and creating a "sandwich" with the multilayer structure between substrates. This sandwich is sliced into sections which are then epoxied into an aluminum tube 2.5 mm in diameter. Once the epoxy dries, the tube is sliced to produce a disk 0.75 mm thick. This disk becomes the sample. However, the thickness is too great for the disk to be of use. The disk is placed onto a grinding and polishing machine where the bottom surface of the disk is ground and polished until 20-50 μm of material is removed. The disk is then flipped, and the top surface is ground and polished until approximately 100-120 μm of material is removed. Finally, the top surface is dimpled until the center of the disk is no thicker than 20-30 μm . The final stage involves perforating the center of the disk with an argon ion beam of approximately 5 keV. The edges of the perforation are the regions of interest. The typical length of ion milling can range from 10 to 30 h.

Imaging the sample is done in a low grade vacuum of 1×10^{-4} torr. Electrons for transmission electron microscopy are accelerated toward the sample at 200 keV

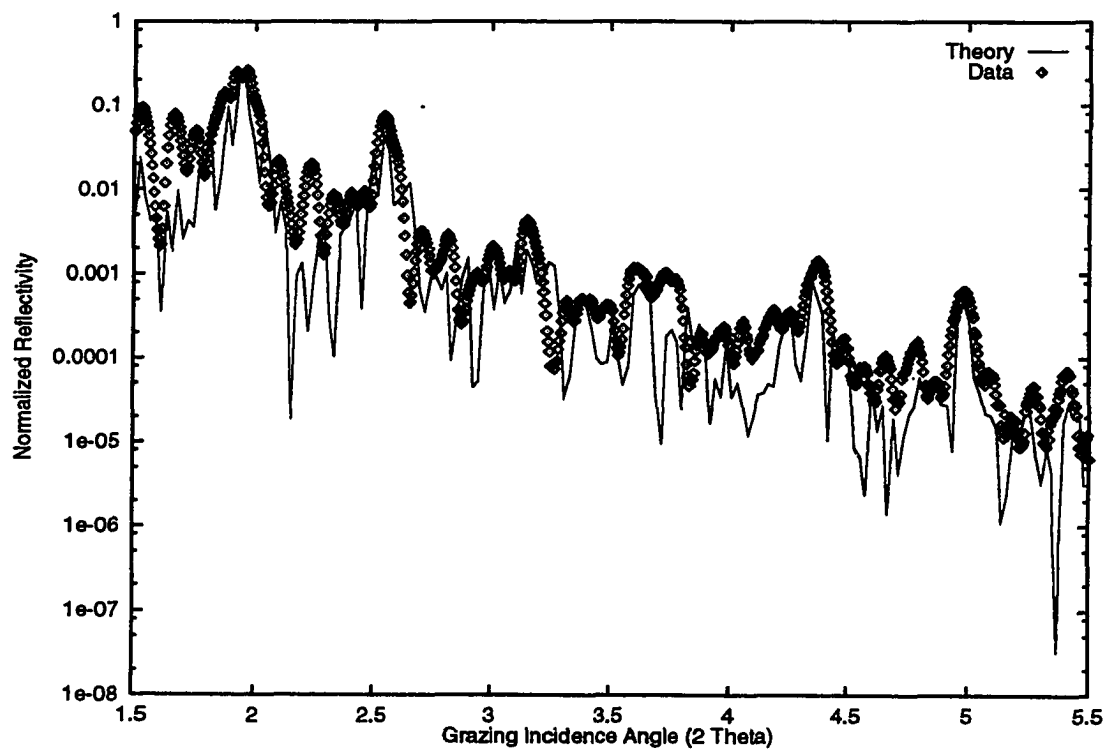


Figure 39. X-ray diffractometry profile of Fabry-Perot filter including thickness errors and interfacial roughness.

with a beam current of 130 μA . The electrons not scattered by the sample strike a fluorescence screen after being focused by magnetic optics. Figure 40 shows a Fabry-Perot filter that was created to determine final sputter deposition rates.

After determining the pair thicknesses of this filter to be 20.8 nm with x-ray diffractometry, individual layer thicknesses may be determined from the photograph. In this case, γ is determined to be 0.219 ± 0.017 , which represents an average silver layer thickness of 4.56 nm and an average silicon layer 16.24 nm thick. The sputter deposition times were 6 and 129 s for silver and silicon, respectively, which yields final sputter deposition rates of 0.76 nm/s for silver and 0.13 nm/s for silicon. This uniquely determines sputter deposition times to create the structure in Table 6.

Figure 41 is a transmission electron micrograph of the final Fabry-Perot filter. The spots on the image are probably the remains of the wax used as an adhesive during the ion milling process. This particular micrograph, however, indicates that these data may only be used qualitatively. Even though the layers look quite uniform, the plot of average pixel value versus depth (in pixels) in Figure 42 shows two processes that modify the data in a way difficult to remove.

Transmission of electrons through material decreases exponentially as a function of thickness. The drop in pixel value signifies an increase in flux and can be roughly modeled by the function

$$P = 190 - e^{0.0035(x-700)} \quad (58)$$

which is plotted along with the data in Figure 42. This particular sample is apparently linearly tapered causing the thin section at high pixel numbers to allow enough electrons through to saturate the film.

Figure 40. Transmission electron micrograph of Sample 26.

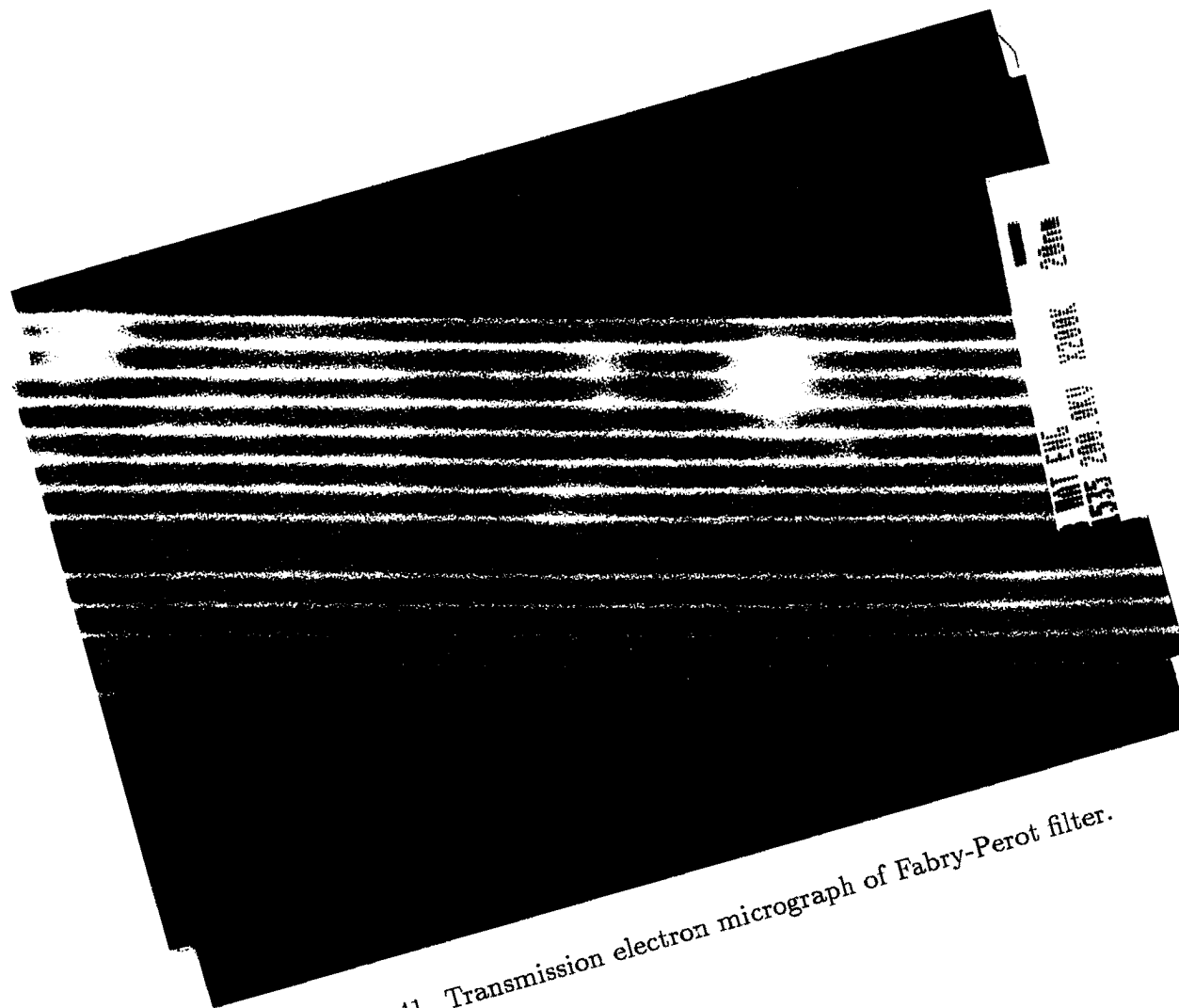


Figure 41. Transmission electron micrograph of Fabry-Perot filter.

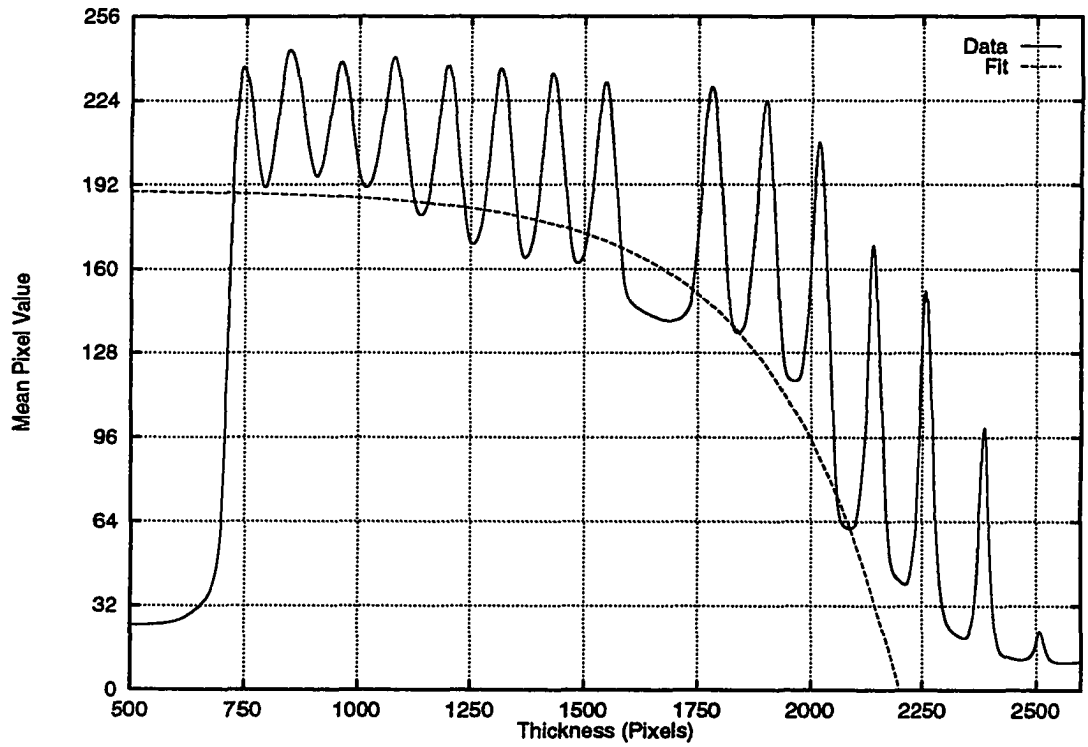


Figure 42. Pixel values for Fabry-Perot filter.

Even with such a degradation in image quality, it could still be possible to examine the interfaces of the sample and get a good feeling for γ . This is also not possible. Examining the roughly flat section at lower pixel numbers and attempting to fit a square wave to the data, it is found that this transmission electron micrograph suggests a gamma of 0.50. Because both the x-ray diffractometry and extreme ultraviolet reflectivity data do not suggest this, it is highly likely that the sample is tilted to the beam. Such tilting will cause electrons to pass through an interface obliquely and “smear” the interface.

Finally, it appears that an additional, initial silver layer was deposited immediately on top of the substrate. This will slightly modify reflectivity in both the x-ray and extreme ultraviolet and will be added to both models.

Extreme Ultraviolet Reflectivity Testing

Extreme ultraviolet reflectivity measurements were made at the Stanford Synchrotron Radiation Laboratory in Stanford, California using one of two vacuum ultraviolet beam lines. Beam line VIII-1 was used to test the fabricated Fabry-Perot filter. It is similar to beam line I-2 used in February 1995 to post-flight calibrate the mirrors and filters from the November 1994 flight of the MSSTA II.³⁴

Beam-line VIII-1 supplies light from visible wavelengths down to $\lambda \approx 5$ nm and is shown schematically in Figure 43. The beam, emergent from one of the bend magnets in the storage ring, is sent through an entrance slit to a monochromator³⁵ and then out the exit slit to a selectable pre-filter stack. An aluminum pre-filter was used to block higher order radiation when testing reflectivities below the aluminum

edge (longer than 16.5 nm). A toroidal mirror focused the beam to a point many meters behind the set-up, roughly collimating the radiation. It was found that the divergence of the beam was approximately 20 arc min^{36} in the vertical direction, however. Fluorescent screens were available to position the beam and to confirm presence of invisible radiation. The beam current monitors are fine gold mesh ($\approx 90\%$ transmissive) which are used as photo-cathodes when placed into the beam-line to monitor beam-current during data acquisition.

The experiment chamber used was not capable of ultra-high vacuum work, which requires the use of sharp-edged flanges and copper gaskets. Use of rubber gasket seals and Apiezon vacuum grease allows pressures no lower than $\approx 5 \times 10^{-7}$ torr after several hours of pumping with a CTI Cryo-8 pump—three orders of magnitude higher than the pressures in the storage ring ($\approx 5 \times 10^{-10}$ torr). In order to connect to the beam-line, a differential pumping system developed by Warburton and Pianetta³⁷ was used which can support pressure differences of up to four orders of magnitude at the vacuum levels of interest.

All data is initially collected as electronic currents from both the the beam current monitor and the photo-diode inside the experiment chamber. These currents are converted into usable data by, first, passing the currents into a Keithley 427 current to voltage amplifier which has a variable gain from $10^4 \leq G \leq 10^{11} \text{ V/A}$. This voltage is sent to a CAMAC crate where it is converted to a pulse train via a voltage to frequency amplifier (1 or 10 V/MHz) and mixed with a real-time clock signal (RTC-018) before being fed into a VAXStation II GPX computer. The “counts” received are then used as data.

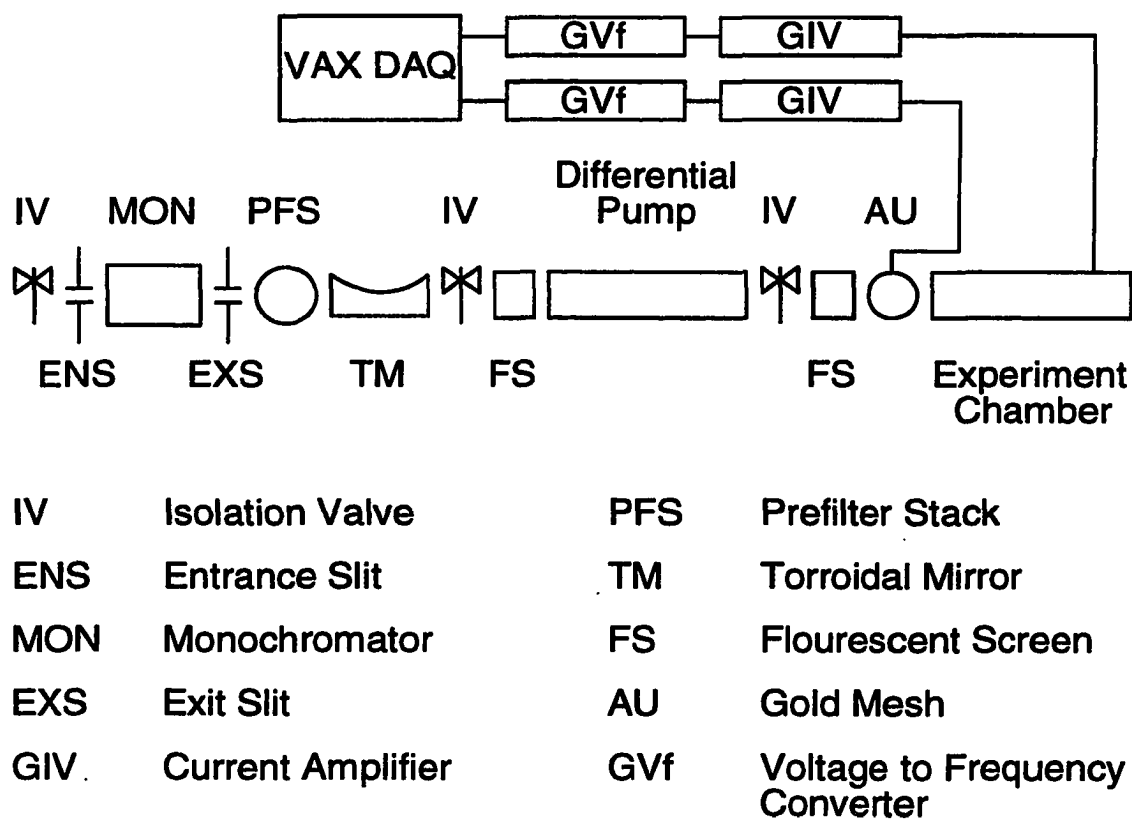


Figure 43. Schematic of SSRL beam-line VIII-1.

These “counts” are generated by a convolution of many processes. The data received at the photo-diode from measuring the intensity of the beam after encountering the optic under test can be represented by

$$C_{diode}(\lambda) = \Phi_{beam}(\lambda, t) R_{mono}(\lambda) \epsilon_{filter}(\lambda) T_{Au}(\lambda) \Phi_{optic}(\lambda) \epsilon_{diode}(\lambda) G_{IV} G_{Vf} \tau \quad (59)$$

where $\Phi_{beam}(\lambda, t)$ is the beam flux, $R_{mono}(\lambda)$ is the reflectivity of the monochromator, $\Phi_{optic}(\lambda)$ is the throughput of optic under test, $\epsilon_{filter}(\lambda)$ is the transmissivity of the pre-filter, $T_{Au}(\lambda)$ is the transmissivity of the gold mesh, $\epsilon_{diode}(\lambda)$ is the response of the photo-diode, G_{IV} is the gain of the current to voltage amplifier, G_{Vf} is the gain of the voltage to frequency amplifier, and τ is the integration time.

The counts received concurrently from the I0 beam monitor can be represented by

$$C_{Au}(\lambda) = \Phi_{beam}(\lambda, t) R_{mono}(\lambda) \epsilon_{filter}(\lambda) \epsilon_{Au}(\lambda) G'_{IV} G'_{Vf} \tau \quad (60)$$

where $\epsilon_{Au}(\lambda)$ is the response of the mesh. The counts received at the photo-diode from a calibration run (no optic in the path) are then calculated as

$$C_{calib}(\lambda) = \Phi_{beam}(\lambda, t) R_{mono}(\lambda) \epsilon_{filter}(\lambda) T_{Au}(\lambda) \epsilon_{diode}(\lambda) G_{IV} G_{Vf} \tau. \quad (61)$$

Dividing both testing and calibration runs by $C_{Au}(\lambda)$ yields

$$\frac{C_{diode}(\lambda)}{C_{Au}(\lambda)} = \frac{T_{Au}(\lambda) \Phi_{optic}(\lambda) \epsilon_{diode}(\lambda)}{\epsilon_{Au}(\lambda)} \left(\frac{G_{IV} G_{Vf}}{G'_{IV} G'_{Vf}} \right) \quad (62)$$

and

$$\frac{C_{calib}(\lambda)}{C'_{Au}(\lambda)} = \frac{T_{Au}(\lambda) \epsilon_{diode}(\lambda)}{\epsilon_{Au}(\lambda)} \left(\frac{G^c_{IV} G^c_{Vf}}{G'^c_{IV} G'^c_{Vf}} \right) \quad (63)$$

where the c superscript labels the data taken during the (separate) calibration run.

The throughput of the optic is then given as

$$\Phi_{optic}(\lambda) = \left(\frac{C_{diode}(\lambda)}{C_{Au}(\lambda)} \right) \left(\frac{C_{Au}^c(\lambda)}{C_{calib}(\lambda)} \right) \left(\frac{G'_{IV} G'_{Vf}}{G_{IV} G_{Vf}} \right) \left(\frac{G_{IV}^c G_{Vf}^c}{G_{IV}^{'c} G_{Vf}^{'c}} \right) \left(\frac{\tau}{\tau^c} \right) \quad (64)$$

which is a bit less cumbersome if all the G_{Vf} 's are kept constant (10 V/MHz) and if $\tau = \tau^c$:

$$\Phi_{optic}(\lambda) = \left(\frac{C_{diode}(\lambda)}{C_{Au}(\lambda)} \right) \left(\frac{C_{Au}^c(\lambda)}{C_{calib}(\lambda)} \right) \left(\frac{G'_{IV}}{G_{IV}} \right) \left(\frac{G_{IV}^c}{G_{IV}^{'c}} \right). \quad (65)$$

Extreme ultraviolet reflectivity testing of the Fabry-Perot filter was conducted with the addition of a goniometer constructed by Lindblom.³⁸ This goniometer is a motorized stage upon which the (flat) sample to be tested can be fit and the photodiode can also be attached. The goniometer is geared such that rotation of the sample by an angle θ rotates the photodiode by an angle 2θ , hence maintaining the photodiode's position with respect to the specularly reflected beam.

To prepare to take data, the goniometer was set to 90° from normal incidence and the sample was placed onto the sample holder. With the sample out of the beam path, a calibration run could be made before the sample was rotated into the beam. The chamber was closed, sealed, and, through the use of a carbon vane pump, sorption pump, and cryogenic pump, pumped down to 5×10^{-6} torr or lower. This required approximately 9 h.

To align the optics to the synchrotron beam, the visible portion of the beam may be selected. The beam-line optics were set to allow "zero order" light to reach the chamber. A glass pre-filter replaces the gold mesh both protecting the gold mesh from harm and the photodiode and optic from being struck by an uncontrolled light

source. The goniometer was aligned to the beam via linear actuators mounted on feed-throughs into the chamber. Beam alignment at the entrance slit was accomplished by visual cues. Alignment of the photocathode end required positioning it such that the Kiethly amplifiers read a maximum value. The monochromator was then set to send the wavelength to which the photocathode is most sensitive. The desired prefilter was then added, and the gains on the amplifiers were set. At this point, the calibration data were taken. To take reflectivity data, the goniometer is rotated (via an electric motor controlled by electronics outside the chamber) until the optic is situated at the desired angle in the beam path. Integration times were 5 s at each energy step of 0.5 eV.

The motor in the goniometer outgassed, causing pressures in the experiment chamber to periodically exceed 1.5×10^{-5} torr, tripping the interlocks and closing the valves. The effects of this are shown in Figure 44. Because the valves are opaque to the beam when closed, the periodic build-up of pressure causes periodic losses in data. These losses were accounted for by collecting three sets of data. In IDL, the “drop-outs” were removed, and the remaining data at each energy sample were averaged together.

Figure 45 plots the result against a theoretically perfect Fabry-Perot filter reflecting at 25° to normal incidence. The slight shift in peak reflectivity is due to both the period of the multilayer being different than expected and systematic error of positioning the goniometer.

Given the layer pair thickness of 14.25 nm determined from x-ray diffractometry, the peaks match a model tilted an angle of 21.5° from normal incidence. The low

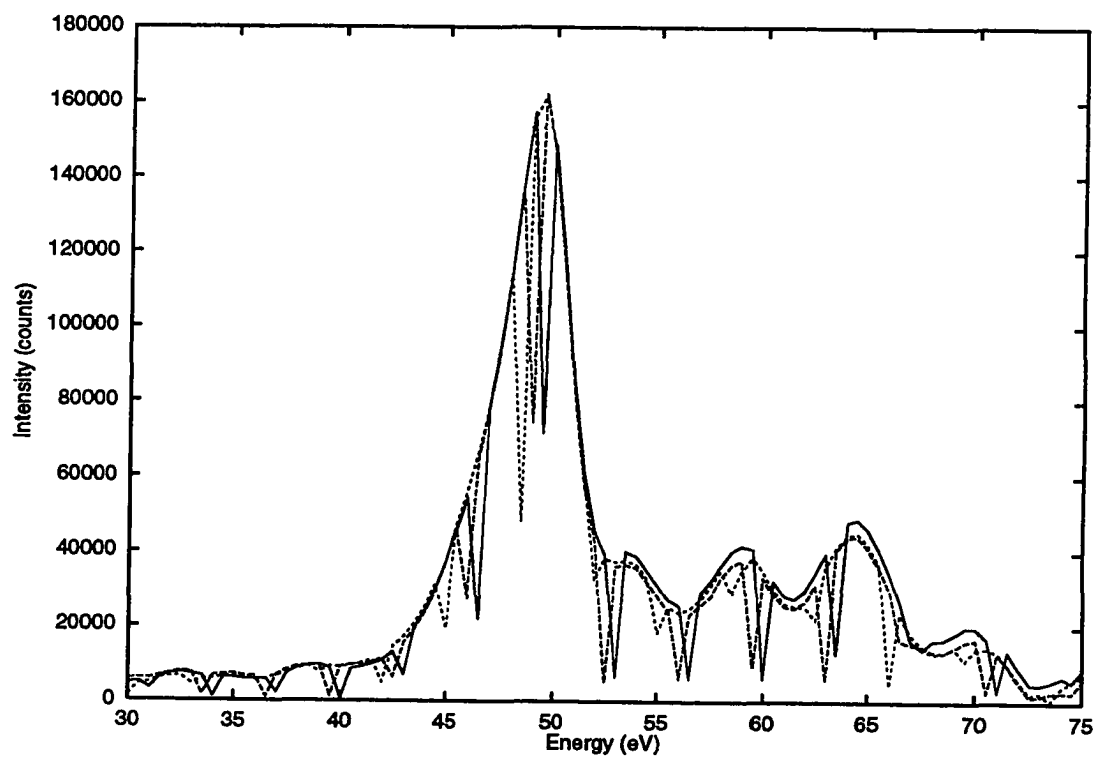


Figure 44. Raw data: photocathode signal for Optic 38.

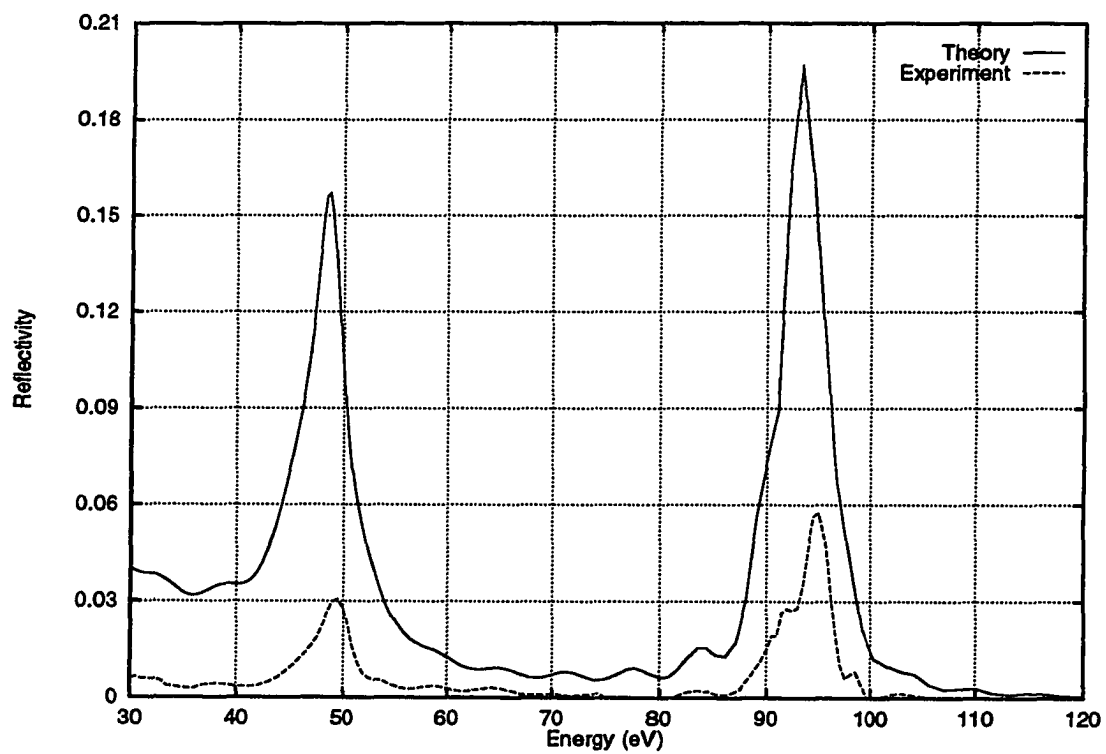


Figure 45. Extreme ultraviolet reflectivity of Fabry-Perot filter.

energy peak is mostly affected by oxidation of the top silicon layer, and the model's top layer is exclusively SiO_2 . Also required for a fit to the data is a 7-nm thick water layer adsorbed to the surface of the multilayer. Thin layers of adsorbed gases are expected unless the temperature of the sample is kept very high (about 1300 K) or the ambient pressure is kept very low (about 10^{-9} torr).³⁹ The high energy peak is more affected by interfacial roughness. A roughness of 1.2 nm has been added to reduce reflectivities appropriately. The x-ray diffractometry data suggests a thickness error of 0.5 nm, and the transmission electron microscopy data state the existence of an additional silver layer at the bottom of the stack. A model taking all these effects into account and plotted with the data is shown in Figure 46.

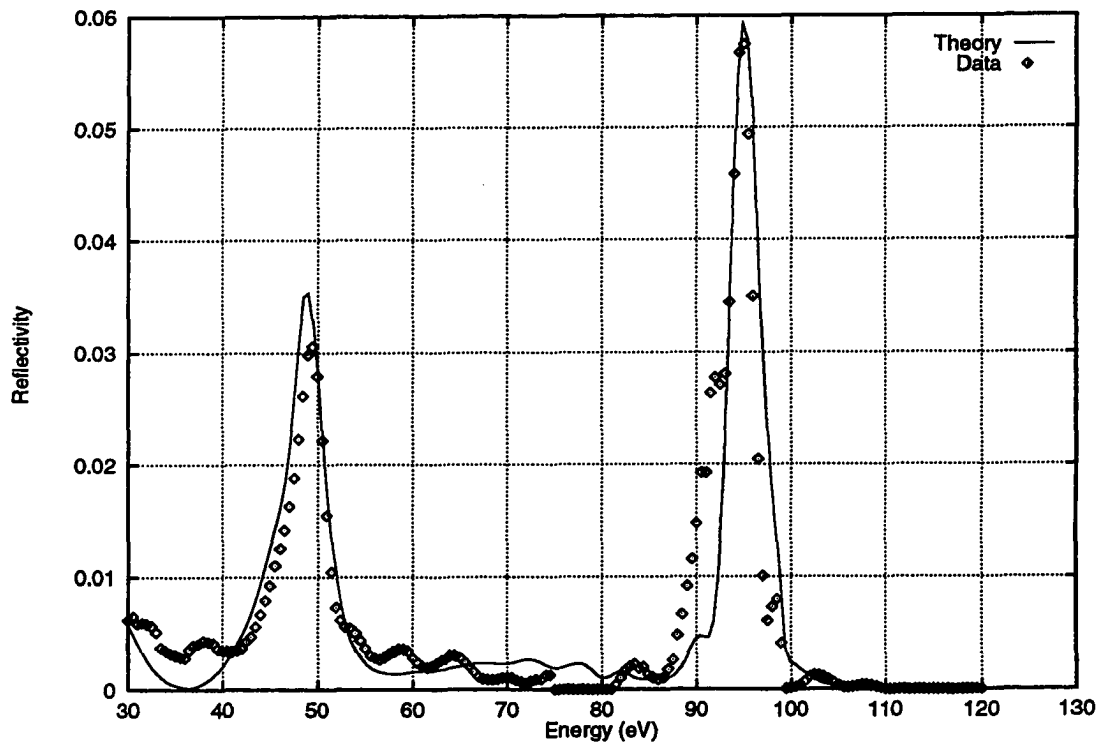


Figure 46. Extreme ultraviolet reflectivity of Fabry-Perot filter including oxidation, interfacial roughness, and thickness errors.

DISCUSSION AND CONCLUSIONS

A Fabry-Perot filter with a bandpass near the Fe XV line at 28.4 nm was designed, fabricated, and tested. This research required investigation of the theoretical optical properties necessary for a device to operate in the extreme ultraviolet and the experimental methods required to produce the optic within design tolerances. Table 11 lists the properties of the multilayer desired, the multilayer able to be fabricated due to sputter deposition constraints, and the multilayer actually constructed as elucidated by both x-ray diffractometry (XRD) and extreme ultraviolet reflectivity measurements taken at SSRL. Figure 47 shows the transmissivity of the perfect filter and the two possible filters determined from structure testing.

Table 11. Comparison of results.

Structure	Perfect	As deposited	XRD	SSRL
Adsorbed water layer thickness (nm)	0	0	7	7
Oxidation of top silicon layer (%)	0	0	100	100
Multilayer pair thickness (nm)	15.0	15.14	14.25	14.25
Multilayer gamma	0.19	0.20	0.20	0.20
Multilayer thickness error (nm)	0	0	0.5	0.5
Interfacial roughness (nm)	0	0	0.5	1.2
Etalon thickness (nm)	26.00	25.96	25.96	25.96
Peak transmission (nm)	28.0	28.2	27.0	27.0
Peak transmissivity (%)	1.55	1.23	1.05	0.75
FWHM (nm)	2.0	1.9	2.8	3.7

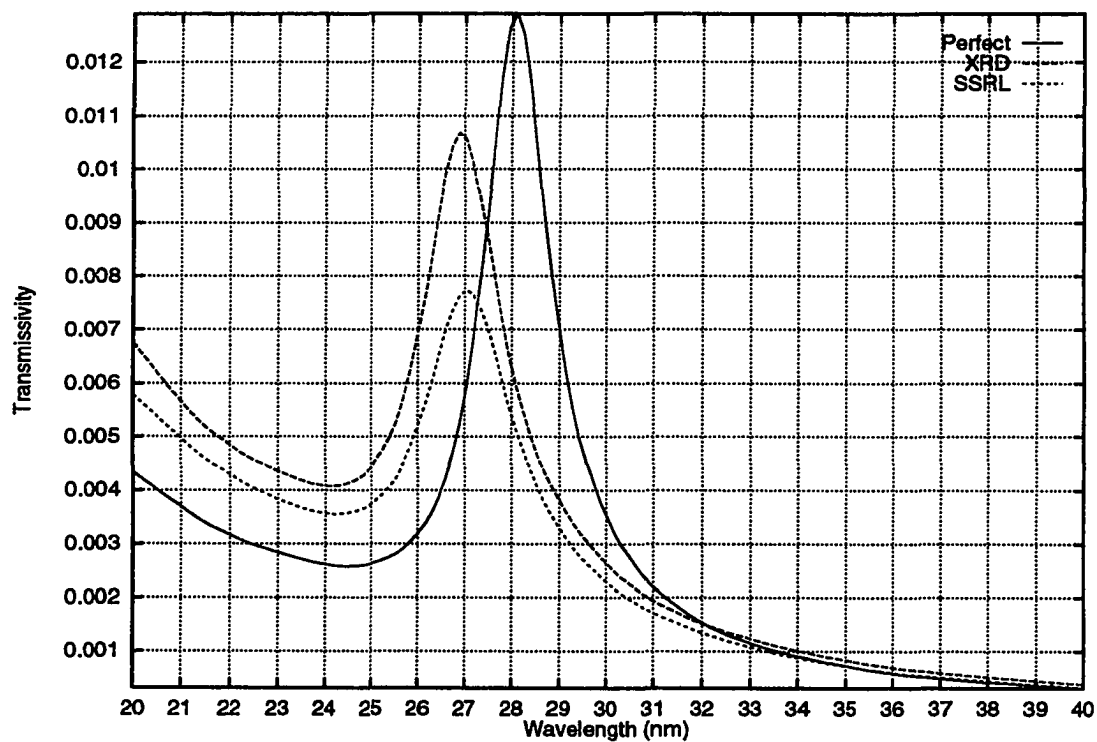


Figure 47. Comparison of perfect Fabry-Perot filter with experiment.

The decision to fabricate a Fabry-Perot filter was made in an attempt to improve upon the thin film filters used for the 1994 MSSTA flight. The Fabry-Perot design allows shifting the peak wavelength and narrowing of the bandpass simply by changing the thickness of the etalon and multilayer ratio, γ , of the mirrors. The current Fabry-Perot filter is of order two ($m = 2$). As designed, it could achieve a peak transmissivity of 1.55% at 28.04 nm with a FWHM of 2.0 nm. The closest thin film filter utilized on the MSSTA flight has a peak transmissivity of 11.4% at 17.2 nm and a 2.6 nm FWHM.

A common Fabry-Perot filter has only four interfaces, two each of ambient with reflective layer and reflective layer with etalon layer. This is unsuitable for use in the extreme ultraviolet because of the low reflectivities at each interface caused by ever decreasing differences in optical constants as wavelengths decrease. At 28.4 nm, the silicon/silver interface has a reflectivity of only 2.4%. Therefore, adding many such interfaces in such a way as to add reflected fields constructively is necessary. This requires the use of multilayer optics. In the fabricated filter, each "mirror" surrounding the etalon was comprised of seven silicon/silver layer pairs, hence thirteen silicon/silver interfaces and a reflectivity of approximately 20%.

The optical constants used to predict performance were based on the model presented by Henke *et al.*²² This model assumes that, at extreme ultraviolet wavelengths, the optical constants of any material are a function only of elemental composition and not of the presence of any particular compound. This model predicts performance well, as noted in Figures 39 and 46.

At these shorter wavelengths, the interface between materials becomes important because interdiffusion can easily produce an interface with a thickness of a sizable fraction of the wavelength of light. To model this, the theory presented by Stearns²⁴ was used in the computational fit. Interdiffusion is typically modeled as an error function, and the reduction of reflectivity at this type of interface follows the form of the Debye-Waller factor in equation (56).

Silicon and silver were chosen as the materials for this Fabry-Perot filter for a number of reasons. First, silicon has a relatively low coefficient of absorption at 28.4 nm, making it suitable for use as an etalon material. Second, silver has a high degree of compatibility with silicon. Not only does silver differ enough from silicon's optical constants to create an interface with decent reflectivity, but its coefficient of absorption is also high enough on both sides of the bandpass of interest to effectively reduce transmissivity in these regions. This avoids Spiller's pitfall¹ of creating a bandpass filter with high "wings," as shown in Figure 19. Third, upon inspection of tables of binary alloys such as Hansen³⁰ and Massalski,³¹ it seems that silver and silicon are not prone to interdiffusion and should make relatively sharp interfaces. This seems to be the case; however, x-ray diffractometry and extreme ultraviolet reflectivity seem to differ on the value of roughness by a factor of 2.4. Finally, it was desired that the materials chosen should not readily combine with atmospheric elements, and, even though the top silicon layer shows signs of oxidation, the reflectivity at extreme ultraviolet wavelengths does not imply that oxidation has traversed the entire multilayer stack.

Many of the parameters for the multilayer were decided upon by computational modeling. Both privately written code and publicly available code were used to choose material pairs from among the many available sputtering targets. The decision to use only seven pairs for each mirror and an etalon thickness of 26.0 nm was based on finding a balance between increased reflectivity and increased absorption.

Once the structure of the Fabry-Perot filter was determined (as listed in Table 6), the layers were deposited via R.F. triode sputtering. Because of the limitations of the system, the structure of the multilayer needed to be modified to those listed in Table 8, causing a mild degradation in the fabricated multilayer.

Given recent success with construction of thin silicon nitride and silicon carbide windows,⁵ an attempt was made to fabricate a transmissive substrate composed of a 30-nm thick layer of silicon nitride stretched across an etched opening in a silicon wafer. This could not be accomplished before extreme ultraviolet testing was to be performed. Transmissivity through the silicon nitride window would be approximately 36.3%. A silicon carbide window of 30 nm thickness would have almost double the transmissivity: 60.9%. The transmissivity of these windows is shown in Figure 48. Silicon dioxide is a poor window material because of its inability to remain flat over large areas.⁴⁰

After the multilayer was fabricated, it was imperative to determine the structure of the fabricated multilayer. Materials content, layer periodicity, layer thickness, and interface quality are the quantities of greatest importance because they have the largest effect on the efficiency of the optic. All tests were performed on small, random areas of the 6.5 cm² sample. Therefore, although no direct measurement of uniformity

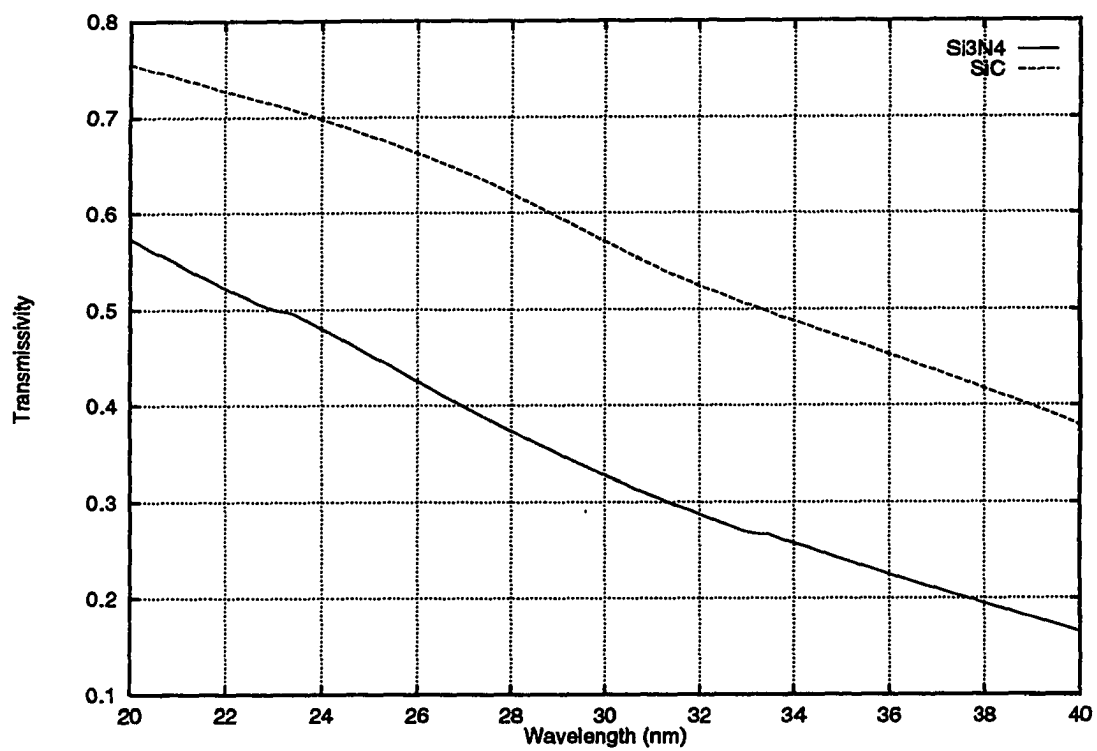


Figure 48. Transmissivity of silicon nitride and silicon carbide windows 30 nm thick.

was made, the fact that the tests are in relative agreement indicate that the multilayer structure is adequately uniform over the full area.

In order to best determine composition, Auger spectroscopy was performed on a sputter deposited sample similar to the final Fabry-Perot filter. No impurities of serious consequence were found. However, oxidation was noted both for silver and silicon layers exposed to atmospheric conditions. The final Fabry-Perot filter appears to have suffered from oxidation of almost all of the top silicon layer. Experiments performed with silicon wafers⁴¹ seem to indicate an expected native oxide of approximately 2 nm thickness. The apparent six-fold increase in oxidation could be caused by the non-crystalline structure of sputter deposited silicon. An argument could be made for the presence of oxygen in the sputter deposition system; however, no such excess oxygen is found incorporated into the multilayer in layers deposited earlier than the final (top) silicon layer.

X-ray diffractometry is a relatively quick test that is most sensitive to layer periodicity, interfacial roughness, and layer thickness errors. The model that best fits the data (Figure 39) has a layer period of 14.25 nm and includes a thickness error of 0.5 nm and an interfacial roughness of 0.5 nm. Typically, measurements at these short wavelengths are preferred to measurements at the longer, extreme ultraviolet wavelengths because the multilayer is less affected by absorption and the optical constants are known more reliably.³³ However, Stearns' model²⁴ for interfacial roughness is an approximation intended to be used away from normal incidence. The true interfacial roughness characteristic is most likely somewhere between the values

of 0.5 nm and 1.2 nm elucidated by x-ray diffractometry and extreme ultraviolet reflectivity, respectively.

Transmission electron microscopy was the most time-intensive test performed. However, it was necessary in order to determine information on gross structure and layer thicknesses. During calibration of sputter deposition rates, transmission electron microscopy data offered the ability to determine γ much better than x-ray diffractometry could alone. Unfortunately, the transmission electron micrograph of the Fabry-Perot interferometer did not record the true structure of the optic. Both a non-uniform thickness across the sample and a non-negligible tilt of the sample to the electron beam caused non-uniform exposure of the film and blurring of interface regions. The transmission electron micrograph, however, did record an additional silver layer deposited by accident which was easily incorporated into the models predicting x-ray diffractometry results and extreme ultraviolet reflectivity.

Even though x-ray reflectivity is considered somewhat more reliable than measurements at longer wavelengths, it is relatively insensitive to the presence of light elements adsorbed onto the surface or absorbed into the bulk of the optic. Testing at extreme ultraviolet wavelengths was the only way to test for these effects and was the most involved of all tests because of the requirement of a relatively well collimated beam with high enough intensity to detect reflectivity at low efficiencies. This test revealed a thin water layer adsorbed on the surface and a completely oxidized top layer of silicon.

The Fabry-Perot filter created for this research demonstrates the possibility of using such a filter for the extreme ultraviolet. With a few simple changes in

etalon thickness and the multilayer mirror ratio, γ , the passband of this filter can be more easily tailored for a specific wavelength than the currently utilized thin film filters. To exact better performance from this particular multilayer, it would be necessary to obtain a deposition system capable of depositing materials to at least an integer multiple of 0.1 s. In situ monitoring of reflectivity during deposition via x-ray reflectivity measurements as presented by Barbee⁴² would also be of great help in reducing the error caused by uncertainties in sputter deposition rates.

These filters have applications wherever imaging narrow bandpasses in the far ultraviolet region is desired. Currently, this requires high flux sources such as the sun because the peak transmissivity is near 1.6%. In spectral line imaging, this filter could possibly be used to selectively filter Fe XV radiation while blocking the He II line at 30.4 nm. The major factors to overcome are the low peak transmissivity and the somewhat wide bandpass.

LIST OF REFERENCES

1. E. Spiller, *Soft X-Ray Optics*, SPIE Optical Engineering Press, Bellingham, WA (1994).
2. D.L. Shealy, C. Wang, W. Jiang, and R.B. Hoover, "Design and analysis of soft x-ray imaging microscopes," *Proc. SPIE*, **1546**, 117-124 (1991).
3. R.B. Hoover, P.C. Baker, J.B. Hadaway, R.B. Johnson, C. Peterson, D.R. Gabardi, A.B.C. Walker, Jr., J.F. Lindblom, C. DeForest, and R.H. O'Neal, "Performance of the multi-spectral solar telescope array III. Optical characteristics of the Ritchey-Chrétien and Cassegrain telescopes," *Proc. SPIE*, **1343**, 189-202 (1990).
4. M. Yamamoto, M. Yanagihara, H. Nomura, and K. Mayama, "Soft x-ray multilayer phase shifter," *Rev. Sci. Instrum.*, **63**, 1510-1512 (1992).
5. C.K. Malek, J. Susini, A. Madouri, M. Ouahabi, R. Rivoira, F.R. Ladan, Y. Lepetre, and R. Barchewitz, "Semitransparent soft x-ray multilayer mirrors," *Optical Engineering*, **29**, 597-601 (1990).
6. A.B.C. Walker, Jr., J.F. Lindblom, R.H. O'Neal, M.J. Allen, T.W. Barbee, Jr., and R.B. Hoover, "Multi-spectral solar telescope array," *Optical Engineering*, **29**, 581-591 (1990).
7. D.B. Gore, J.B. Hadaway, R.B. Hoover, A.B.C. Walker, and C.C. Kankelborg, "Optical focussing and alignment of the multi-spectral solar telescope array II payload," *Proc. SPIE*, **2515**, 532-543 (1995).
8. F.R. Powell, P.W. Vedder, J.F. Lindblom, and S.F. Powell, "Thin film filter performance for extreme ultraviolet and x-ray applications," *Optical Engineering*, **29**(6), 614-624 (1990).
9. T. Barbee, Jr. and J.H. Underwood, "Solid Fabry-Perot etalons for x-rays," *Optics Communications*, **48**, 161-166 (1983).
10. F.E. Fernandez, C. Riedel, A. Smith, B. Edwards, B. Lai, F. Cerrina, M.J. Carr, A.D. Romig, Jr., J. Corno, L. Nevot, B. Pardo, J.M. Slaughter, and C.M. Falco, "Monolithic Fabry-Perot structure for soft x-rays," *Proc. SPIE*, **984**, 256-262 (1988).
11. R.B. Hoover, A.B.C. Walker, Jr., J. Lindblom, M. Allen, R. O'Neal, C. DeForest, and T.W. Barbee, Jr., "Solar observations with the multi-spectral solar telescope array," *SPIE Proc.*, **1546**, 175-187 (1991).

12. J.B. Hadaway, R.B. Johnson, R.B. Hoover, J.F. Lindblom, and A.B.C. Walker, Jr., "Design and analysis of optical systems for the Stanford/MSFC multi-spectral solar telescope array," *SPIE Proc.*, **1160**, 195-208 (1989).
13. R.B. Hoover, R.B. Johnson, S. Fineschi, A.B.C. Walker, Jr., P.C. Baker, M. Zukic, and J. Kim, "Design and fabrication of the all-reflecting H-Lyman α coronagraph/polarimeter," *SPIE Proc.*, **1742**, 439-451 (1992).
14. A.B.C. Walker, Jr., T.W. Barbee, Jr., R.B. Hoover, and J.F. Lindblom, "Soft x-ray images of the solar corona with a normal-incidence Cassegrain multilayer telescope," *Science*, **241**, 1725-1868 (1998).
15. P.N. Peters, R.B. Hoover, R. Watts, C. Tarrio, and A.B.C. Walker, Jr., "Fabrication of multilayer optics by sputtering: application to EUV optics with greater than 30% normal reflectance," *SPIE Proc.*, **2515**, 576-581 (1995).
16. A.B.C. Walker, Jr., M.J. Allen, C.E. DeForest, C.C. Kankelborg, D.S. Martínez-Galarce, J.E. Plummer, R.B. Hoover, T.W. Barbee, Jr., and D.B. Gore, "The multi spectral solar telescope array VIII: the second flight," *Proc. SPIE*, **2515**, 182-193 (1995).
17. D. Martínez-Galarce, A.B.C. Walker, II, D.B. Gore, C.C. Kankelborg, R.B. Hoover, T.W. Barbee, Jr., and P.F.X. Boerner, "High resolution imaging with multilayer telescopes: resolution performance of the MSSTA II telescopes," Submitted to *Optical Engineering* (1999).
18. J.F. Lindblom, R.H. O'Neal, A.B.C. Walker, Jr., F.R. Powell, T.W. Barbee, Jr., R.B. Hoover, and S.F. Powell, "Performance of the multi-spectral solar telescope array IV: the soft x-ray and extreme ultraviolet filters," *Proc. SPIE*, **1343**, 544-557 (1990).
19. J.E. Plummer, C.E. DeForest, D.S. Martínez-Galarce, C.C. Kankelborg, D. Gore, R.H. O'Neal, and A.B.C. Walker, Jr., "The design and performance of thin foil XUV filters for the multi-spectral telescope array II," *SPIE Proc.*, **2515**, 565-575 (1995).
20. M.V. Klein and T.E. Furtak, *Optics*, John Wiley & Sons, Inc., New York, NY (1986).
21. T.C. Chen, "Turning-point method of optimised multilayer design," *IEE Proc.*, **137-J-2**, 101-107 (1990).
22. B.L. Henke, E.M. Gullikson, and J.C. Davis, "Low energy x-ray interaction coefficients: photoabsorption, scattering, transmission and reflection. $E = 50$ -30,000 eV, $Z = 1$ -92," *Atomic Data and Nuclear Data Tables*, **54**, (1993).
23. A.V. Vinogradov and B.Ya. Zeldovich, "X-ray and far UV multilayer mirrors: principles and possibilities," *Applied Optics*, **16**(1), 89-93 (1977).
24. D.G. Stearns, "The scattering of x-rays from nonideal multilayer structures," *J. Appl. Phys.*, **65**(2), 491-506 (1989).

25. P. Debye, "Über die Intensitätsverteilung in den mit Röntgenstrahlung erzeugten Interferenzbildern," *Verh. d. Deutsch. Phys. Ges.*, **15**, 738 (1913).
26. R.J. Bartlett, W.J. Trela, D.R. Kania, M.P. Hockaday, T.W. Barbee, Jr., and P. Lee, "Soft x-ray measurements of solid Fabry-Perot etalons," *Optics Communications*, **55**(4), 229-235 (1985).
27. D.L. Windt, "IMD - software for modeling the optical properties of multilayer films," *Computers in Physics*, **12**(4), 360-370 (1998).
28. A.E. Rosenbluth, "Computer search for layer materials that maximize the reflectivity of x-ray multilayers," *Revue Phys. Appl.*, **23**, 1599-1621 (1988).
29. T. Bäck and M. Schütz, "Evolution strategies for mixed-integer optimization of optical multilayer systems," *Proc. Evolutionary Programming IV*, 33-51 (1995).
30. Max Hansen, *Constitution of Binary Alloys*, McGraw-Hill, New York, NY (1958).
31. Thaddeus B. Massalski, *Binary Alloy Phase Diagrams*, American Society for Metals, Metals Park, OH (1986).
32. A.M. Hawryluk, N.M. Ceglio, D.G. Stearns, K. Danzmann, M. Kühne, P. Müller, and B. Wende, "Soft x-ray beamsplitters and highly dispersive multilayer mirrors for use as soft x-ray laser cavity components," *Proc. SPIE*, **688**, 81-90 (1987).
33. E. Spiller, "Characterization of multilayer coatings by x-ray reflection," *Revue Phys. Appl.*, **23**, 1687-1700 (1988).
34. C.C. Kankelborg, J.E. Plummer, D.S. Martínez-Galarce, R.H. O'Neal, C.E. DeForest, A.B.C. Walker, Jr., T.W. Barbee, Jr., J.W. Weed, R.B. Hoover, and F.R. Powell, "Calibration of multilayer mirrors for the multi-spectral solar telescope array II," *Proc. SPIE*, **2515**, 436-444 (1995).
35. P. Thiry, *et al.*, "A 6 m toroidal-grating-monochromator beam line for high momentum-resolution photoelectron spectroscopy," *Nucl. Instr. Meth.*, **222**(1), 85-90 (1984).
36. M.J. Allen, T.D. Willis, C.C. Kankelborg, R.H. O'Neal, D.S. Martínez-Galarce, C.E. DeForest, L.R. Jackson, J.D. Plummer, A.B.C. Walker, Jr., T.W. Barbee, and R.B. Hoover, "Performance of the multilayer coated mirrors for the multi spectral solar telescope array," *SPIE Proc.*, **2011**, 381-390 (1993).
37. W.K. Warburton and P. Pianetta, "A novel differential pump for synchrotron beam lines: tests, models and applications," *Nucl. Instr. Meth.*, **A291**, 350-356 (1990).
38. J. F. Lindblom, "Soft x-ray/extreme ultraviolet images of the solar atmosphere with normal incidence multilayer optics," Ph.D. Thesis, Stanford, (1990).

39. E.W. McDaniel, *Collision Phenomena in Ionized Gases*, John Wiley & Sons, New York, NY (1964).
40. C.W. Wilmsen, E.G. Thompson, and G.H. Meissner, "Buckling of thermally grown SiO₂ thin films," *IEEE Trans. Electron Devices*, **19(1)**, 122 (1972).
41. S.I. Raider, R. Flitsch, and M.J. Palmer, "Oxide growth on etched silicon in air at room temperature," *J. Electrochem. Soc.*, **122(3)**, 413-418 (1975).
42. T.W. Barbee, Jr., "Multilayers for x-ray optics," *Optical Engineering*, **25(8)**, 898-915 (1986).

**GRADUATE SCHOOL
UNIVERSITY OF ALABAMA AT BIRMINGHAM
DISSERTATION APPROVAL FORM
DOCTOR OF PHILOSOPHY**

Name of Candidate David B. Gore



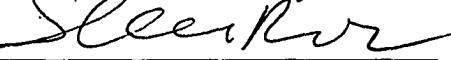
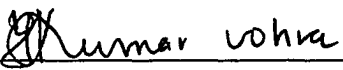
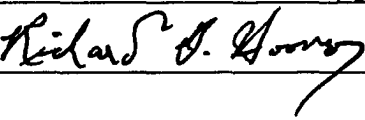
Major Subject Physics

Title of Dissertation A Silicon/Silver Multilayer Fabry-Perot Bandpass Transmission

Filter for Use Near 28.4nm

I certify that I have read this document and examined the student regarding its content. In my opinion, this dissertation conforms to acceptable standards of scholarly presentation and is adequate in scope and quality, and the attainments of this student are such that he may be recommended for the degree of Doctor of Philosophy.

Dissertation Committee:

Name	Signature
<u>David L. Shealy</u> , Chair	<u></u>
<u>Chris Lawson</u>	<u></u>
<u>Sergey Mirov</u>	<u></u>
<u>Yogesh K. Vohra</u>	<u></u>
<u>Robin Griffin</u>	<u>ROBIN D. GRIFFIN (Gm)</u>
<u>Richard Hoover</u>	<u></u>

Director of Graduate Program 

Dean, UAB Graduate School 

Date 10/4/99